Final Report for Texas AQRP Project 14-003

Update and Evaluation of Model Algorithms Needed to Predict Particulate Matter from Isoprene

Submitted to:

Dr. Elena McDonald-Buller, Project Manager Texas Air Quality Research Program
The University of Texas at Austin

Submitted by:

University of North Carolina – Chapel Hill

William Vizuete, Jason D. Surratt, M. Riedel, Yuzhi Chen, Ken Sexton, Ying-Hsuan Lin, Sri Hapsari Budisulistiorini, Cassandra J. Gaston, Joel A. Thornton, Zhenfa Zhang, Avram Gold, Roger E. Jerry

Revised September 2015

QA Requirements: Audits of Data Quality: 10% Required

1. Table of Contents

1. Executive Summary

Terrestrial vegetation emits large quantities (~500 teragrams Carbon (C)) into the atmosphere of a chemical called isoprene (C_5H_8). Isoprene emissions in eastern Texas and northern Louisiana are some of the largest in the United States. The photochemical oxidation of emitted isoprene leads to significant yields of gas-phase intermediates that then contribute to particulate matter (PM) through secondary organic aerosols (SOA). The production of isoprene-derived PM is enhanced when mixed with anthropogenic emissions from urban areas like those found in Houston. To quantify the contribution that PM production from isoprene has in Texas requires air quality models to predict the oxidation chemistry that produces the gas phase PM precursors. These models must also be updated with the fundamental parameters needed to describe the efficiency that these gas phase precursors react on the surface of PM. The goal of this project was to provide new information on these two critical processes. The following four tasks were completed to accomplish this goal:

1. Integration of Gas-Phase Epoxide Formation and Subsequent SOA Formation into our smog chamber box model

2. Synthesis of Isoprene-derived Epoxides and Known SOA Tracers

3. Indoor Chamber Experiments Generating SOA Formation Directly from Isoprene-Derived Epoxides

4. Modeling of Isoprene-derived SOA Formation From Environmental Simulation Chambers

Upon successful completion of these tasks we have already published two articles. The two completed manuscripts are listed here and the results and findings can be found in Chapters 2-3 of this report.

1. Chen, Y.Z., et al., Assessment of SAPRC07 with updated isoprene chemistry against outdoor chamber experiments. Atmospheric Environment, 2015. **105**: p. 109-120.

2. Riedel, T.P., et al., Heterogeneous Reactions of Isoprene-Derived Epoxides: Reaction Probabilities and Molar Secondary Organic Aerosol Yield Estimates. Environmental Science & Technology Letters, 2015. **2**(2): p. 38-42.

A third draft manuscript that is listed below is currently in review and its draft is presented in Chapter 4 of this report.

3. Riedel, T. P., Z. Zhang, K. chu, J. Thornton, W. Vizuete, A. Gold and j. d. Surratt, Constraining Condensed-Phase Formation Kinetics of Secondary

Organic Aerosol Components from Isoprene Epoxydiols. Atmospheric Chemistry and Physics, **in review** 2015.

A. Key Findings

1. Gas Phase Oxidation of Isoprene

We have evaluated against outdoor chamber experiments the state of the science Community Multi-scale Air Quality (CMAQ) modeling system version of the Statewide Air Pollution Research Center (SAPRC07) mechanism we have called the Xie mechanism and published our results [1]. This research version of the SAPR07 chemical mechanism is a combination of improved isoprene oxidation pathways by EPA researchers [2] and the base mechanism SAPRC07T [3]. Our model performance results suggest that the new Xie mechanism produces more ozone (O_3) and predicts an earlier Nitrous Oxide (NO)/ Nitrous Dioxide (NO_2) crossover time than SAPRC07 for all experiments. Under lower-NO+ NO_2 conditions, both mechanisms over-predict O_3 observations; the Xie mechanism worsens performance and increases the bias of O_3 from 4.9% to 9.4%. Overall, the Xie mechanism reacts more Volatile Organic Carbons (VOCs) due to a more explicit representation of isoprene oxidation products and therefore increases subsequent hydroxyl radical (OH) formation. The increased reaction rate of VOCs results in more NO to NO_2 conversions by peroxy radicals and more production of aldehyde. The Xie mechanism also increases NO_2 recycling from nitrogen termination species, which accounts for the increase in the afternoon O_3 peak concentrations in the lower-NO_X experiments. The increase in NO_2 recycling from peroxyacetyl nitrate species (PAN) accounts for 85% of the total increase in NO_2 recycling.

This data suggests a continued focus on the production of radical and SOA precursor species to improve the ability of the mechanism to simulate ozone chemistry while maintaining explicit gas phase precursors for isoprene SOA. The significantly larger concentrations in our experiments allow for all day oxidation. Our results, however, may not be applicable for ambient conditions at low NO_X concentrations. Chamber experiments at ambient NO_X concentrations are needed to obtain a complete understanding of the performance of the Xie mechanism under ambient-relevant conditions.

2. Formation of PM

A combination of flow reactor studies and chamber modeling was used to constrain two uncertain parameters central to SOA formation from isoprene-derived gas phase precursors:

(1) Rate of epoxide heterogeneous uptake to the particle phase

(2) Molar fraction of gas phase precursors that are reactively taken up and contribute to SOA (ϕ_{SOA}).

Flow reactor measurements of the *trans*-β-isoprene epoxydiol (*trans*-β-IEPOX) and methacrylic acid epoxide (MAE) aerosol reaction probability (γ) were completed on atomized aerosols with compositions similar to those used in chamber studies [4]. Observed γ ranges for *trans*-β-IEPOX and MAE were 6.5×10^{-4}–0.021 and 4.9×10^{-4}–5.2×10^{-4}. Through the use of a time-dependent chemical box model initialized with chamber conditions and the γ measurements, ϕ_{SOA} for *trans*-β-IEPOX and MAE on different aerosol compositions was estimated between 0.03–0.21 and 0.07–0.25, with MAE ϕ_{SOA} showing more uncertainty.

As discussed above, it is unclear how γ and ϕ_{SOA} are affected when a significant fraction of surface area (S_a) is represented by epoxide-derived SOA. This warrants further investigation as it could be relevant in regions like eastern Texas during summer where isoprene SOA can account for a substantial portion of $PM_{2.5}$ mass and therefore S_a. The results presented here, and in our previous study [5] that constrained all reactions contributing to IEPOX- and MAE-derived SOA, could be beneficial in regional and/or global models to help constrain predictions of IEPOX- and MAE-derived SOA. This is especially true since only a few known aqueous-phase reaction rates constrain current models.

We have completed our chemical box model simulations that explicitly predict the gas- and aqueous-phase reactions during chamber experiments of SOA growth from IEPOX uptake onto acidic sulfate aerosol. These reactions are listed in Figure 1.1. Specifically, the model is constrained by recent measurements of the IEPOX reactive uptake coefficient [4, 5], experimentally obtained aqueous-phase rate constants [6], chamber-measured aerosol mass and surface area concentrations, aerosol thermodynamic model calculations with Extended AIM Aerosol Thermodynamics Model (E-AIM III) [7], and offline filter measurements of SOA of a number of the aforementioned tracers.

$$IEPOX_{(aq)} + H^+ \rightarrow C_5\text{-alkene triols} + H^+ \quad \text{(R5)}$$

$$IEPOX_{(aq)} + H^+ \rightarrow \text{3-MeTHF-3,4-diols} + H^+ \quad \text{(R6)}$$

$$IEPOX_{(aq)} + H^+ + \text{2-methyltetrols} \rightarrow \text{IEPOX-dimer} + H^+ \quad \text{(R7)}$$

$$IEPOX_{(aq)} + H^+ + IEPOX\text{-OS} \rightarrow \text{IEPOX-dimerOS} + H^+ \quad \text{(R8)}$$

$$IEPOX_{(aq)} + H^+ \rightarrow \text{other SOA} + H^+ \quad \text{(R9)}$$

Figure 1.1 Reactions used in box model.

The resulting model-predicted tracer formation rate constants for these reactions are given in Table 1.1. These are averaged over all experiments and the listed errors correspond to one standard deviation. For the purpose of comparison, we have also included the existing literature values [8, 9] in the top portion of the table.

Table 1.1 Model-predicted tracer formation rate constants (k) where "OS" is defined as IEPOX-derived organosulfates.

SOA tracer formed	k	reaction
2-methyltetrols	9.0×10^{-4} M^{-2} s [a]	(R1)
2-methyltetrols	1.3×10^{-5} M^{-2} s [a]	(R2)
IEPOX-OS	2.0×10^{-4} M^{-2} s [a]	(R3)
IEPOX-OS	2.9×10^{-6} M^{-2} s [a]	(R4)
C_5-alkene triols	$7.8 \pm 0.4 \times 10^{-4}$ M^{-1} s	(R5)
3-MeTHF-3,4-diols	$9.2 \pm 1.2 \times 10^{-4}$ M^{-1} s	(R6)
IEPOX-dimer	$7.7 \pm 2.7 \times 10^{-7}$ M^{-2} s	(R7)
IEPOX-dimerOS	$8.1 \pm 3.3 \times 10^{-6}$ M^{-2} s	(R8)
other SOA	$5.4 \pm 0.2 \times 10^{-3}$ M^{-1} s	(R9)

[a]from Eddingsaas et al., 2010; see also Pye et al., 2013

Figure 1.2 shows a tracer-specific model simulation and the corresponding offline filter measurements from the chamber experiment. Through the use of offline filter measurements collected during the chamber experiments, we are able to place estimates on the tracer formation reaction rate constants that have yet to be measured for bulk solutions. By varying the aqueous-phase reaction rate constants in the model that lack experimental constraints until the modeled SOA tracer mass loadings closely match those of the filter measurements we are able to constrain the kinetics of the aerosol-phase species that have been quantified through offline techniques but lack formation rate information. Additionally, those species that are not quantified through filter analyses, which we term "other SOA", are also examined and a preliminary formation rate constant for the sum of those species can be obtained.

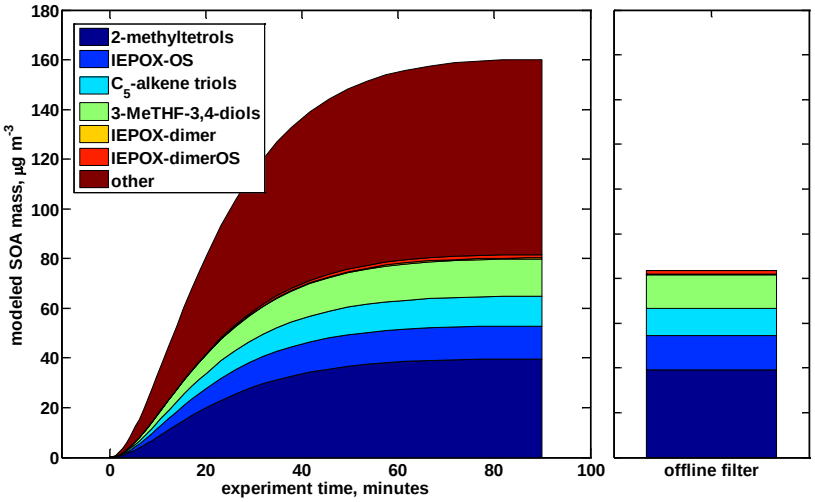

Figure 1.2 Model simulation of speciated SOA growth during a chamber experiment (left panel). Corresponding filter measurements during the chamber experiment (right panel). "other SOA" represents tracers not quantified by the filter analyses.

B. Project Deliverables

The critical information generated by this project has been disseminated in two published publications [1, 4] in the peer-reviewed literature, and a third manuscript that is currently in progress of being drafted [10]. The two published manuscripts are provided in chapters 2-3 and the draft manuscript in chapter 4. Each chapter provides detailed methodological and supporting information for the key findings described in this summary. Following are other key deliverables provided by this project.

- We have developed evaluation software that allows a user to evaluate chemical mechanisms against UNC's experimental chamber runs. This includes incorporating data into the software from 40 experiments (16 characterization runs and 24 isoprene runs) that were conducted in the UNC Dual Gas-phase Chamber (Pittsboro, NC). These experimental runs include real-time concentration data of NO_X, VOCs and O_3. Other data from these experiments include temperature, relative humidity, and light intensity. Using this evaluation software we have generated data evaluating two chemical mechanisms: the standard SAPRC07 [3] and the updated Xie mechanism [2].

- We have generated new experimental data that quantitatively measures the reactive uptake of two predominant isoprene-derived gas phase intermediates to PM. These new fundamental measurements provide for the first time the data needed to directly evaluate the aerosol-phase processes in an air quality model. These experiments include *trans*-β-IEPOX and MAE chamber runs where SOA

growth was measured with various relative humidity (RH) levels and seed aerosol types. These data were used to generate ɣ results for *trans*-β-IEPOX and MAE including the 1σ error for each measurement.

- A 0-Dimension time-dependent box model was developed and data generated that simulated the chamber experiments and estimated ϕ_{SOA}.

- Techniques for the synthesis of isoprene-derived epoxides and known SOA tracers were developed and quality assured.

- We have estimated reaction rate constants needed for the model to predict SOA tracer loadings.

C. References

1. Chen, Y.Z., et al., *Assessment of SAPRC07 with updated isoprene chemistry against outdoor chamber experiments.* Atmospheric Environment, 2015. **105**: p. 109-120.
2. Xie, Y., et al., *Understanding the impact of recent advances in isoprene photooxidation on simulations of regional air quality.* Atmospheric Chemistry and Physics, 2013. **13**(16): p. 8439-8455.
3. Hutzell, W.T., et al., *Interpreting predictions from the SAPRC07 mechanism based on regional and continental simulations.* Atmospheric Environment, 2012. **46**: p. 417-429.
4. Riedel, T.P., et al., *Heterogeneous Reactions of Isoprene-Derived Epoxides: Reaction Probabilities and Molar Secondary Organic Aerosol Yield Estimates.* Environmental Science & Technology Letters, 2015. **2**(2): p. 38-42.
5. Gaston, C.J., et al., *Reactive Uptake of an Isoprene-Derived Epoxydiol to Submicron Aerosol Particles.* Environmental Science & Technology, 2014. **48**(19): p. 11178-11186.
6. Eddingsaas, N.C., D.G. VanderVelde, and P.O. Wennberg, *Kinetics and Products of the Acid-Catalyzed Ring-Opening of Atmospherically Relevant Butyl Epoxy Alcohols.* The Journal of Physical Chemistry A, 2010. **114**(31): p. 8106-8113.
7. Wexler, A.S. and S.L. Clegg, *Atmospheric aerosol models for systems including the ions H^+, NH_4^+, Na^+, SO_4^{2-}, NO_3^-,Cl^-, Br^-, and H_2O.* Journal of Geophysical Research-Atmospheres, 2002. **107**(D14).
8. Pye, H.O., et al., *Epoxide pathways improve model predictions of isoprene markers and reveal key role of acidity in aerosol formation.* Environ Sci Technol, 2013. **47**(19): p. 11056-64.
9. Eddingsaas, N.C., D.G. VanderVelde, and P.O. Wennberg, *Kinetics and Products of the Acid-Catalyzed Ring-Opening of Atmospherically Relevant Butyl Epoxy Alcohols.* Journal of Physical Chemistry A, 2010. **114**(31): p. 8106-8113.
10. Riedel, T.P., et al., *Constraining Condensed-Phase Formation Kinetics of Secondary Organic Aerosol Components from Isoprene Epoxydiols.* Atmospheric Chemistry and Physics, 2015.

2. Assessment of SAPRC07 with updated Isoprene Chemistry against Outdoor Chamber Experiments

A. Introduction

Isoprene (2-methyl-1, 3-butadiene, C_5H_8) is the most abundant non-methane hydrocarbon emitted from vegetation [1] and has a significant impact on atmospheric chemistry. Isoprene is known to influence ground-level ozone (O_3) formation in urban areas rich with biogenic emissions [2, 3]. In recent years new discoveries have been made concerning isoprene oxidation chemistry leading to secondary organic aerosol (SOA) or particulate matter (PM) formation [4– 12]. By combining organic synthesis, computational calculations, smog chamber studies, and field measurements researchers have recently characterized reactive epoxides that are produced from the photochemical oxidation of isoprene and are significant for SOA formation [4, 5, 9, 12]. These gas phase oxidation products include methacrylic acid epoxide (MAE) and isomeric isoprene epoxydiols (IEPOX). From recent work it is clear that anthropogenic pollutants, such as oxides of nitrogen NO_X and sulfur dioxide SO_2, significantly enhance these isoprene-derived epoxides as a source of PM2.5 [4, 5, 8, 9, 12]. This is of great public health and regulatory importance since isoprene is primarily emitted from terrestrial vegetation, and thus, is not controllable, whereas anthropogenic emissions (e.g., NO_X, SO_2, or pre-existing primary aerosol) are controllable.

The chemical mechanisms in current regulatory models, however, do not have the gas-phase chemistry needed to predict isoprene-based SOA precursors. Isoprene gas phase oxidation chemistry is currently represented in air quality models (AQMs) in a condensed form. It is designed to represent the chemical formation of O_3 while incorporating simplification and approximation for computational efficiency. To evaluate future control strategies, new gas and particle phase isoprene chemistry must be incorporated into AQMs to study the importance of isoprene emissions on both ground level O_3 and SOA formation.

Xie et al. (2013) has developed a more explicit isoprene chemical mechanism with additional OH and NO_3 oxidation pathways that produce SOA precursors. The mechanism is based on SAPRC07T [13], which adds hazardous air pollutants and precursors to secondary aerosols to the original SARPC07 [14–16]. In the original SAPRC07 mechanism, the reaction of isoprene with OH gives a product mixture including methacrolein (MACR) and methyl vinyl ketone (MVK) as shown below in R.1:

(R.1) ISOP + OH → 0.986 RO_2C+0.093 RO_2XC + 0.093zRNO_3

+0.907xHO_2 + 0.624xHCHO + 0.23xMACR + 0.32xMVK + 0.357xIPRD + yR_6OOH + 0.167XC

All the above species are SAPRC07 species defined in [14–16].

In the Xie modification, bulk hydroxyl-peroxy isoprene radicals (ISOPO2) is formed in reaction 2 (R.2), which in turn produces MACR and MVK by reaction with other species, namely, NO, HO2, MEO2, RO2C, MECO3 and ISOPO2 itself [13].

(R.2) ISOP + OH → $ISOPO_2$ + ISOPRXN

In the original SAPRC07 mechanism, reaction with NO3 does not yield either MACR or MVK, but in the Xie modification the product NISOPO2 is created as show in reaction 3 (R.3).

(R.3) ISOP + NO_3 → $NISOPO_2$

NISOPO2, like its non-nitrated analogue, reacts with NO3, NO, MEO2, RO2C, and MECO3 to give small yields of MACR and MVK [13]. Other reactions of isoprene, with O_3 and chloride (Cl) radicals, are unchanged in the Xie modification. Isoprene-derived nitrates are treated explicitly. First generation isoprene nitrates include ISOPN (= ISOPND + ISOPNB), NIT1, and NISOPOOH. ISOPND and ISOPNB are produced in the Xie mechanism instead of RNO3 in the standard SAPRC07. ISOPN reacts an order of magnitude faster with OH and has almost 100% higher recycling of NO_2 than RNO3 does. NIT1 formed in NISOPO2 + NO/NO3/RO2 reactions reacts with OH and NO3 and forms respective peroxy radical species, which react with other radicals similarly as the initially formed peroxy radical species (ISOPO2/NISOPO2) to yield little NO_X and other products. Xie also assumes 70% NO_X recycling efficiency from NIT1 + O_3 oxidation.

NISOPOOH is the product of NISOPO2 + HO2 reaction. The OH oxidation of the above first-generation nitrates forms secondary isoprene nitrates including: short-lived MVKN, MACRN, ETHLN, RNO3I, and longer-lived PROPNN. These products can either react with OH or photolyze to give NO_2 back. In the Xie mechanism, isoprene oxidation chemistry under low NO_X conditions was updated. These updates include IEPOX formation from ISOPO2 + HO2 channel (R.4) and HPALD formation from ISOPO2 isomerization (R 5). HOX is produced in subsequent reactions of products from both reactions.

(R.4) ISOPOOH + OH → IEPOX + OH
(R.5) $ISOPO_2$ → HO_2 + HPALD

Xie et al. (2013) integrated the updated SAPRC07T chemical mechanism into the CMAQ model version 4.7 and simulated from 1 July to 16 August 2004 across the entire continental US and a portion of Canada and Mexico [13]. These additions to the CMAQ model allow for explicit predictions of OH reformation from isoprene peroxy radicals,

NO_2 recycling from isoprene nitrates and IEPOX-SOA tracers (and thus total SOA mass from isoprene oxidation). Current AQMs estimate that isoprene contributes 27% [17] ~ 48% [18] to the global burden of SOA [19], yet under predict summertime isoprene SOA especially in areas like the southeastern U.S. [20]. Xie et al. found that, compared to the base case simulation with SAPRC07T [20], their updated mechanism improves the simulation of aircraft measurement for gas phase compounds including NO_X (bias from -7% to 1%), O_3 (increases 1-2 ppbv with bias still within 5%), HCHO (bias from -12% to -9%) and isoprene (bias from 26% to 4%). Xie defined bias as shown in eqn. 2-1. Xie also reported biogenic SOA increased by 15% compared to the base case.

Eqn. 2.1

$$NMB = \frac{1}{n}\sum \frac{simulation - observation}{observation} \times 100\%$$

The CMAQ results reported by Xie et al demonstrated improved model performance for several species, but large uncertainties still lie in the new gas phase chemistry. These uncertainties include isoprene nitrates yield from isoprene + OH/NO pathway and NO_X recycling efficiency from first-generation nitrates. Further, it is difficult to evaluate a chemical mechanism in AQMs, where other processes like transport, deposition and emissions act synergistically. The compensating errors from those processes might result in good agreement between observations and predictions and thus veil the real problems within the mechanism. To resolve this problem, smog chamber experiments are traditionally used to test and refine a new mechanism, or evaluate an existing mechanism [21]. The smog chamber is a closed and controlled system allowing for chemistry to be the main process that influences concentration. Thus, the discrepancy or agreement between observations and predictions are directly correlated with the mechanism being used. Condensed gas phase mechanisms are finely tuned engineering approximations for atmospheric chemistry. Xie et al. have added new reactions and species to the base mechanism and consequently have altered the radical budgets and nitrogen cycling. The Xie mechanism has yet to be evaluated against smog chamber experiments before being widely used in AQMs. Thus, it is currently unknown how the Xie modification of SAPRC07T impacts the ability of the model to predict O_3, isoprene decay, and its oxidation products.

In this paper we will evaluate the Xie mechanism with simulations of experiments from the University of North Carolina (UNC) outdoor smog chamber. A rich archive of chamber experiment data [22] provides this study with reliable measurements from 24 experiments conducted with isoprene and NO_X. These experiments were carried out for isoprene to NO_X concentration ratios (ISOP:NO_X) ranging from 0.18 to 9.29 in ppm/ppm, with initial NO_X concentrations from 0.17 ppm and 0.83 ppm. The focus will be on changes in model predictions from the SAPRAC07 mechanism that may have been introduced by the Xie et al. updates and evaluating the mechanism's ability to predict ozone.

B. Methods

1. Experimental

Overall, 40 experiments (16 characterization runs and 24 isoprene runs) were conducted in the UNC Dual gas-phase chamber (Pittsboro,NC), where the real-time concentration of NO_X,VOCs and O_3 can be measured in accuracy. Environmental parameters including temperature, relative humidity, and light intensity were also monitored to compute chemical and photochemical reaction rates. Detailed descriptions of the chambers and measurement instruments employed can be found in the appendix [23]. Sixteen characterization runs were chosen to evaluate the light model and wall chemistry parameters represented in the auxiliary mechanism [24]. Explanation of the auxiliary mechanism (version-aadg) developed by Jeffries et al. for UNC smog chamber are available in other materials [24, 25]. Species in these runs include carbon monoxide (CO), methane (CH_4), ethene (C_2H_4) and formaldehyde (HCHO). These are explicit species in the chemical mechanism and whose kinetic information is well quantified. The initial injections of these runs are outlined in Table 2.1.

Twenty-four isoprene photooxidation experiments were selected and shown in Table 2.2. In this study, runs in which the isoprene:NOX concentrations have a ratio less than 1.25 (ppm/ppm) were arbitrarily classified as having a low VOC:NOX ratio or a high NO_X experiment, while those over 1.25 were considered to have a high VOC:NO_X ratio or a lower NO_X experiment.

2. Modeling

Two mechanisms compared in this study, standard SAPRC07 [14, 15] and Xie, were implemented in the Morpho Photochemical Reaction Simulation System (MORPHO) [26]. The SAPRC07 source code was created based on Dr. Carter's report [14, 15]. The Xie mechanism was contained in the CMAQ files provided by Dr. Xie, and converted to the Morpho format [24].

C. Results and Discussion

1. Model Performance

Simulations of with SAPRC07 and the Xie mechanism were statistically compared with observational data in terms of peak O_3 concentration and $NONO_2$ crossover time derived

from temporal concentration profiles of NO, NO_2, O_3 (Figure 2.3 and Figure 2.4). The NO-NO_2 crossover time implies how fast a mechanism is converting NO to NO_2 and propagating the autocatalytic process of O_3 production. Ozone peak/maximum value is a direct indicator of regulatory interest as reflected by 8-hour ozone standard in NAAQS. Both indicators are reported in the form of normalized mean bias (NMB) computed using Eqn. 2.1.

Eqn. 2.1

$$NMB = \frac{1}{n}\sum \frac{simulation - observation}{observation} \times 100\%$$

2. O_3 Peak

O_3 peak concentration values were plotted against observational values shown in Figure 2.1. For chamber VOC + NO_X daytime experiments, the observed pattern of O_3 temporal profile changes with relative NO_X abundance. A lower NO_X experiment is often characteristic of two O_3 peaks, of which the second peak is due to photolysis of NO_2 released back from reservoir species like PAN. Here we only display the results of the first morning O_3 peak due to direct ozone photochemistry. Under all conditions the Xie O_3 peak was consistently higher than the peak predicted with SAPROC07 by as much as 22.5%. The difference was most pronounced under high NO_X conditions (Figure 2.1a). Both mechanisms show consistent over-prediction under lower NO_X conditions as shown in Figure 2.1b and Table 2.3. It is important to note that under lower NO_X the Xie mechanism is pushing model performance in the wrong direction increasing bias from 4.92 to 11.08%. There is insufficient number of runs in our high NO_X experiments to conclude a statistically significant difference in the two mechanisms. It is clear that the modifications made to SAPRAC07 have resulted in increasing the magnitude of peak ozone.

3. NO-NO_2 Crossover

Figure 2.2 shows the observed NO-NO_2 crossover time versus simulated results across 8 high NO_X experiments and 16 lower NO_X experiments. We found that both mechanisms under-predict NO-NO_2 crossover time for lower NO_X experiments. The Xie mechanism always had a sooner crossover time than SAPRC07 and was even sooner for lower NO_X experiments. Detailed statistical results are summarized in Table 2.4.

4. Process Analysis

In the following analysis, our focus shifts from model-to-observation comparison to mechanism inter-comparison under different initial ISOP:NOX ratios. Chemical reaction process analysis is applied in this step using Python-based Environment for Reaction Mechanisms/Mathematics (PERMM) [27]. Process analysis is

based on the concepts of integrated reaction rate (IRR) analysis [26, 28]. The IRR over each time step of each reaction in the mechanism is outputted to .irr file and the IRR over the course of the simulation and its corresponding reaction is outputted to .irrmg file by MORPHO. PERMM reads in these MORPHO outputs and provides an interface to obtain net reactions and quantify radical and NO_X budgets. To account for the pattern observed in model performance assessment, we conducted reaction process analysis on two selected cases – one high NO_X case and one lower NO_X case (Table 2.5). The differences between SAPRC07 and Xie for all parameters are reported in the form of relative difference (RD) using equation 2.2. In this case, a positive RD value would suggest Xie has a higher cycle number, vice versa.

Eqn. 2.2

$$RD = \frac{Xie - SAPRC07}{SAPRC07} \times 100\%$$

5. Case Study

The concentration profiles of O_3, NO, and isoprene are displayed side by side in Figure 2.3 and Figure 2.4. Ozone temporal concentration profiles are characteristic of distinctive observed patterns under different initial VOC and NO_X concentration levels. For a typical high NO_X (low VOC:NOX ratio) chamber experiment (Figure 2.3a), the system runs out of NO late in the day compared with the lower NO_X (high VOC:NOX ratio) experiment and gradually makes ozone until 5 pm for our high NO_X experiment JN2381BLUE.In comparison, a typical lower NO_X experiment has a shorter-lasting photochemical production of ozone. Take our lower NO_X experiment JN2697RED as an example, the second O_3 peak (0.75 ppb) occurs at 2 pm due to NO_2 released from its reservoir species NO_Z.

For JN2381BLUE (high NO_X), both mechanisms under-predict the NO-NO_2 crossover time and maximum O_3 concentration. Neither mechanism is able to predict the actual O_3 peak around 5 pm. The Xie mechanism had a result closer to the measurement. For JN2697RED (lower NO_X), both mechanisms over-predict the NO-NO_2 crossover time and under-predict the morning O_3 peak to a similar extent. The Xie mechanism, however, produces O_3 faster in the afternoon increasing final O_3 concentrations by 0.22 ppb and 0.36 ppb compared to the observation and SAPRC07. Regardless of the difference of the ability to re produce observations the Xie mechanism predicts an earlier crossover time and a higher O_3 peak concentration and is visually represented in Figure 2.3. Table 2.6 lists the reactions for the OH reaction with isoprene and its resulting products. Figure 2.4 shows the isoprene decay for the two experiments with the Xie mechanism oxidizing more isoprene faster. The loss of isoprene due to the reaction with OH is consistent with

the OH concentration levels shown in Figure 2.5. Because of that, the first generated ISOPO2 of the Xie mechanism dominates over RO2C (SAPRC07) in NO-to-NO_2 conversion, and produces more formaldehyde (HCHO) and HO2. There was up to a three times increase in HO2 production rate from aldehyde photolysis, most of which is from formaldehyde (Figure 2.6). HO2 from aldehyde converts NO to NO_2 and produces a OH radical. This OH will participate in a new round of VOC oxidation and propagation reactions, thus amplifying the entire chain. Accordingly, more OH is predicted by the Xie mechanism as shown in Figure 2.5. The increased OH production permits the Xie mechanism to continue to oxidize VOCs until the end of the experiment (Figure 2.7).

Figure 2.8 shows the integrated reaction rate of VOC + OH (solid lines in Figure 2.7) over the entire courses of two experiments. Xie mechanism has more OH+VOC reactions due to both the introduction of new species and the increased reaction of existing species. A complete lists of VOCs reacted with OH are shown in their own identities in Figure 2.9 and 2.10. Note that there is a mass shift within certain species because of changed pathways in Xie mechanism. For example, RNO3 are now represented by species including ISOPND, ISOPNB, NIT1, NISOP2OOH, MACRN, MVKN, and ETHLN, RNO3I and itself in the Xie mechanism. So part of the OH radicals that used to react with RNO3 are now distributed to reaction with each of those species. A summary of the OH radical budget is tabulated in Table 2.7. This OH cycle number is an indication of the efficiency of the system in using OH radicals. In the simulations by the Xie mechanism, the OH cycle is about -33.7% different in the high NO_X case, but 8% different in the lower NO_X case. In the high NO_X case, the Xie mechanism was less efficient in use of OH even though it produced twice the amount of new OH (Table 2.7). The increased OH concentration in this experiment, coupled with higher NO_2 concentrations, increased the competition of OH through termination reaction (R.6) instead of VOC + OH reactions. For the lower NO_X case, this termination pathway is not as significant so the difference in OH cycle for the two mechanisms is less.

(R.6) $NO_2 + OH -> HNO_3$

The photolysis of NO_2 is the dominant pathway to make O3 in the troposphere. Table 2.8 shows that for the high NO case JN2381BLUE the reactions of NO_X with XO2 and nitrogen termination products (NO_Z) account for 47% of NO_2 production in the Xie mechanism compared to 31% in SAPRC07. Almost 50% of NO_2 comes from reaction of NO with O_3 in the Xie mechanism, compared to 65% in SAPRC07. Therefore, the Xie mechanism is able to produce more O_3. For the lower NO_X case, there is a 47% difference for the second peak O_3 concentration. Table 2.8 also shows that about 77% more NO_2 is recycled from NO_Z in the Xie mechanism than in SAPRC07, causing this increase in ozone production. Table 2.9 shows the NO cycles for both experiments. In high NO_X experiments, the increased nitrogen termination reactions result in a 21% decrease in the NO cycle. In lower NO_X experiments, the reconstruction of the isoprene oxidation pathways in Xie producing NO_2 from NO_Z species result in an increasing rate of NO_2

production in the afternoon (Figure 2.12b), and therefore a higher NO cycle. In this experiment, the NO cycle difference between two mechanisms is 32%. This explains the sustained ozone production, resulting in the increasing O3 concentrations shown in Figure 2.3. The consistency remains for experiments having higher ISOP:NOX ratios, of which the second peak differences between two mechanisms are even larger. We found that the majority of NO_2 recycling increase comes from PANs (Figure 2.13). Xie mechanism predicts 64% more NO_2 from PANs (PAN, MA PAN & PAN2) than SAPRC07 and that increase accounts for 85% of the total increase in NO_2 recycling. This is due to increased first-generation VOCs products and NO_2 concentration, thus more PANs being made. The Xie mechanism has changed the radical balance of SAPRC07 and directed more NO_X to its temporary reservoir species instead of terminating it through XN (Figure 2.11b).

Figure 2.14 shows the percent difference between the two mechanisms of the OH and NO cycle for the entire experimental set. In the high NO_X experiments, the difference in OH cycle is smaller than that in the lower NO_X experiments. When the experimental conditions are at lower NO_X concentrations, the Xie mechanism tends to have a higher OH cycle. A similar trend is observed in NO cycle difference (Figure 2.14b). The Xie mechanism has the ability to produce more OH reactions with VOCs and convert more NO to NO_2 than the SAPRAC07 mechanism. Under high NO_X conditions, this results in higher NO_2 and OH concentrations and thus increased termination reactions. Although more NO_2 and ultimately O_3 are produced, the OH and NO cycle are lowered. In the lower NO_X experiments, the termination reactions are not as large and the recycled NO_2 late in the day accounts for the differences in the cycle numbers with the SAPRAC07 mechanism.

6. Sensitivity Runs

Model performance results under lower NO_X conditions prompted several sensitivity runs exploring low NO_X chemistry and NO_2 recycling. Again, the lower NO_X experiment selected for process analysis JN2697RED will be used as our testing case. Recent chamber experimental work by Fuchs et al. (2013) confirmed OH regeneration from HPALD produced in ISOPO2 unimolecular reactions (1,6-H shift) but the rate constant $k1,6-isom = 8.5 \times 10^{8} \exp(-5930/T)\ cm^3/s$ in Leuven isoprene mechanism (LIM) [29] is too large. They evaluated against isoprene photo-oxidation experiments the values of k1,6-isom and proposed a rate of $6.20 \times 10^{8} \exp(-7700/T)\ cm^3/s$ that can reproduced observed OH [30]. However, their experiments were not able to give a more accurate quantification of k1,6-isom because of uncertainties in rate coefficient value for 1,5-H shift isomerization of ISOPO2 and additional recycling of unknown peroxy radicals. Xie used $4.07 \times 10^{8} \exp(-7694/T)\ cm^3/s$ [31, 32]. Here we simulated with a value of $2.35 \times 10^{8} \exp(-7694/T)\ cm^3/s$. The second analysis will focus on changing the isoprene nitrates (ISOPN) yield. The original value used in Xie et al.'s paper (2013) is 12%. The

value in the CMAQ files Dr. Xie provided was reduced to 6% and we used this value in our simulations so far. Here we zeroed it out to evaluate its effect on NO_2 recycling of the lower NO_X case. The sensitivity parameters and their values are summarized in Table 2.10.

In Run A, halved ISOPO2 isomerization rate constant has no impact on NO-NO_2 crossover time and ozone maximum concentration (1.0% less). In Run B, the shut-off of ISOPN yield from ISOPO2 + NO pathway reduced ozone maximum by 5.5%. This confirms the key role of PANs has played in NO_2 recycling efficiency changes under lower NO_X experiments.

D. Conclusion

We evaluated the CMAQ version of SAPRC07 mechanism with improved isoprene oxidation pathways by Xie et al. (2013) against outdoor chamber experiments and the base mechanism SAPRC07. Our model performance results suggest that the Xie mechanism produces more O_3 and predicts a faster NO to NO_2 crossover time than SAPRAC07 for all experiments. Under lower NO_X conditions, both mechanisms over predict observations and the Xie mechanism worsens performance and increases the bias from 4.92% to 11.08%. The Xie mechanism reacts more VOCs due to the increased explicit representation of isoprene oxidation products and subsequent OH formation. This increased rate of VOC reactions results in more NO to NO_2 conversions by peroxy radicals and more production of aldehyde. The Xie mechanism also increases NO_2 re-cycling from NO_Z species, which accounts for the increase in O_3 concentrations in the afternoon for lower NO_X experiments. The increase in NO_2 recycling from PANs accounts for 85% of the total increase in NO_2 recycling. Attempts to improve ozone model performance at lower NO_X experiments showed limited influence to the isoprene nitrates yields from ISOPO2 + OH/NO pathway. A shut-off of ISOPN yield merely resulted in a 5.5% decrease in ozone maximum concentrations. This confirms that changes in NO_2 recycling efficiency should be attributed to increased PANs production, which is a result of increased initial VOC + OH reactions and NO_2 production. These results underline the importance of further efforts in refining the stoichiometry of isoprene oxidation pathways within a condensed mechanism and further lab studies on characterizing more reasonable rate constants for those pathways.

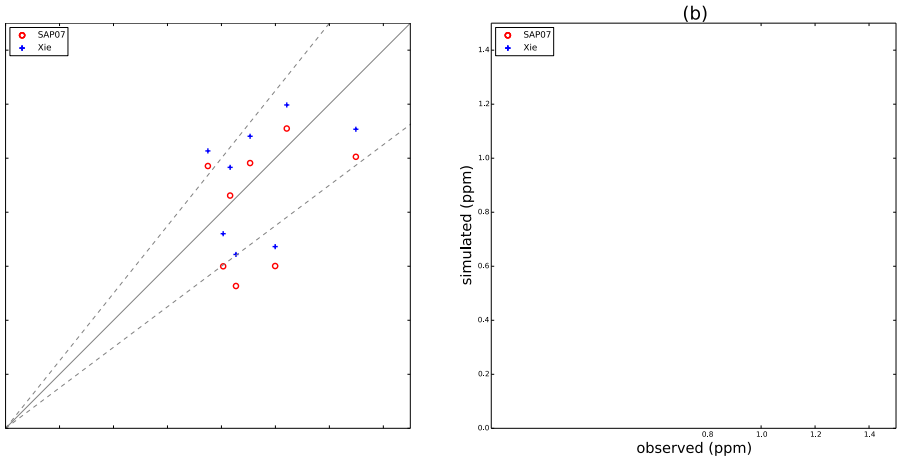

Figure 2.1. Ozone peak (a) under low isoprene:NOX ratio and (b) under high isoprene:NOX ratio experiments.

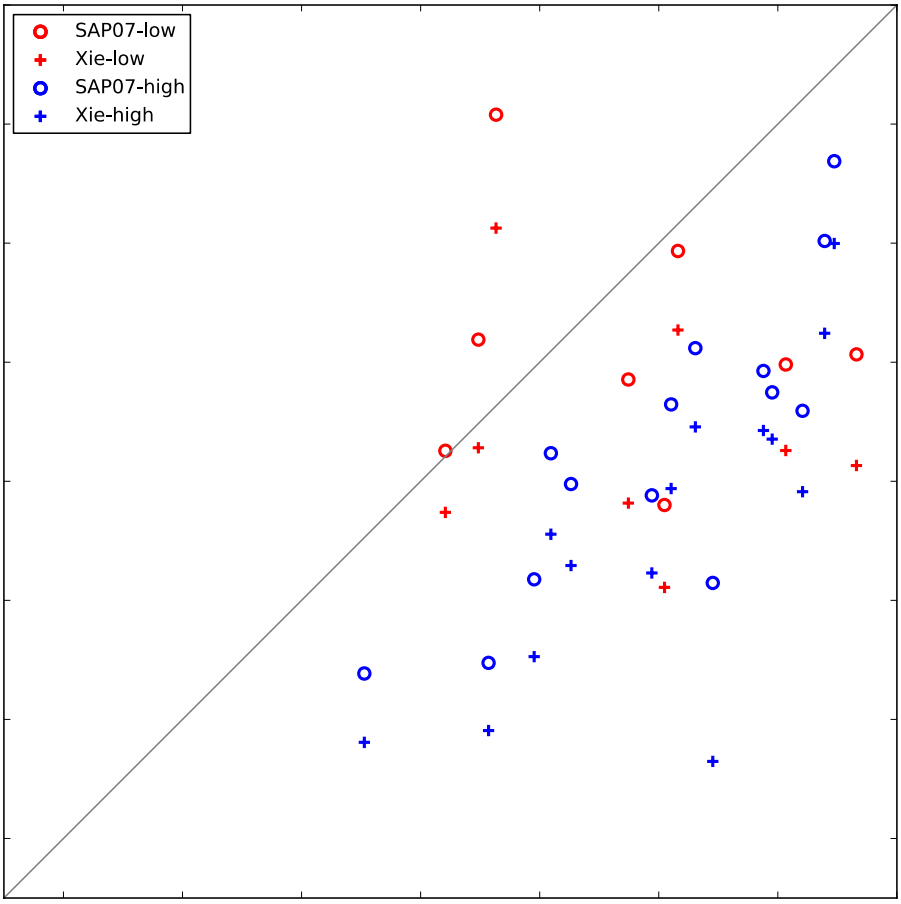

Figure 2.2 NO-NO2 Crossover time

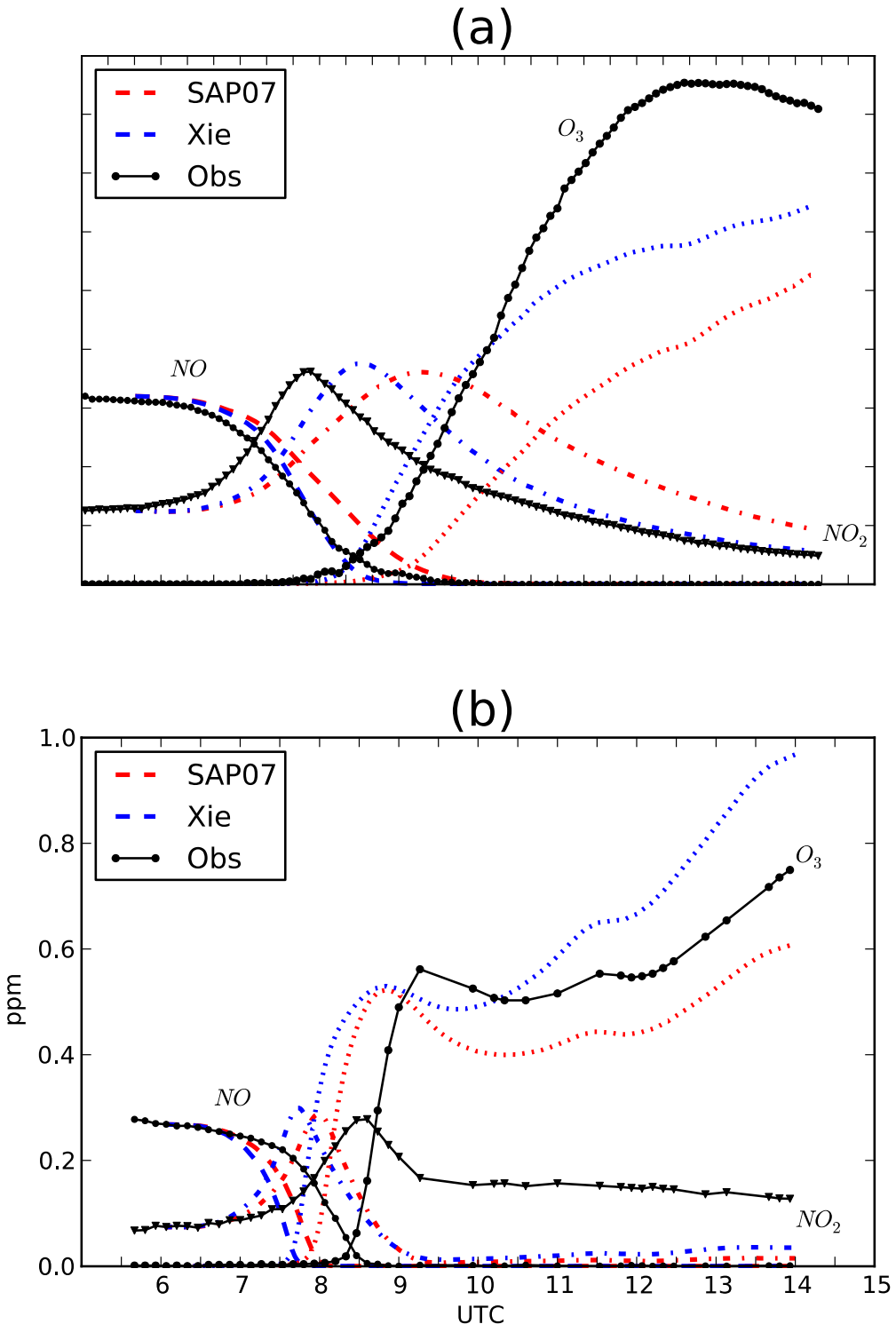

Figure 2.3. Ozone and NO_X concentration time profile for: (a) JN2381BLUE (High NO_X) and (b) JN2697RED (Lower NO_X) experiments.

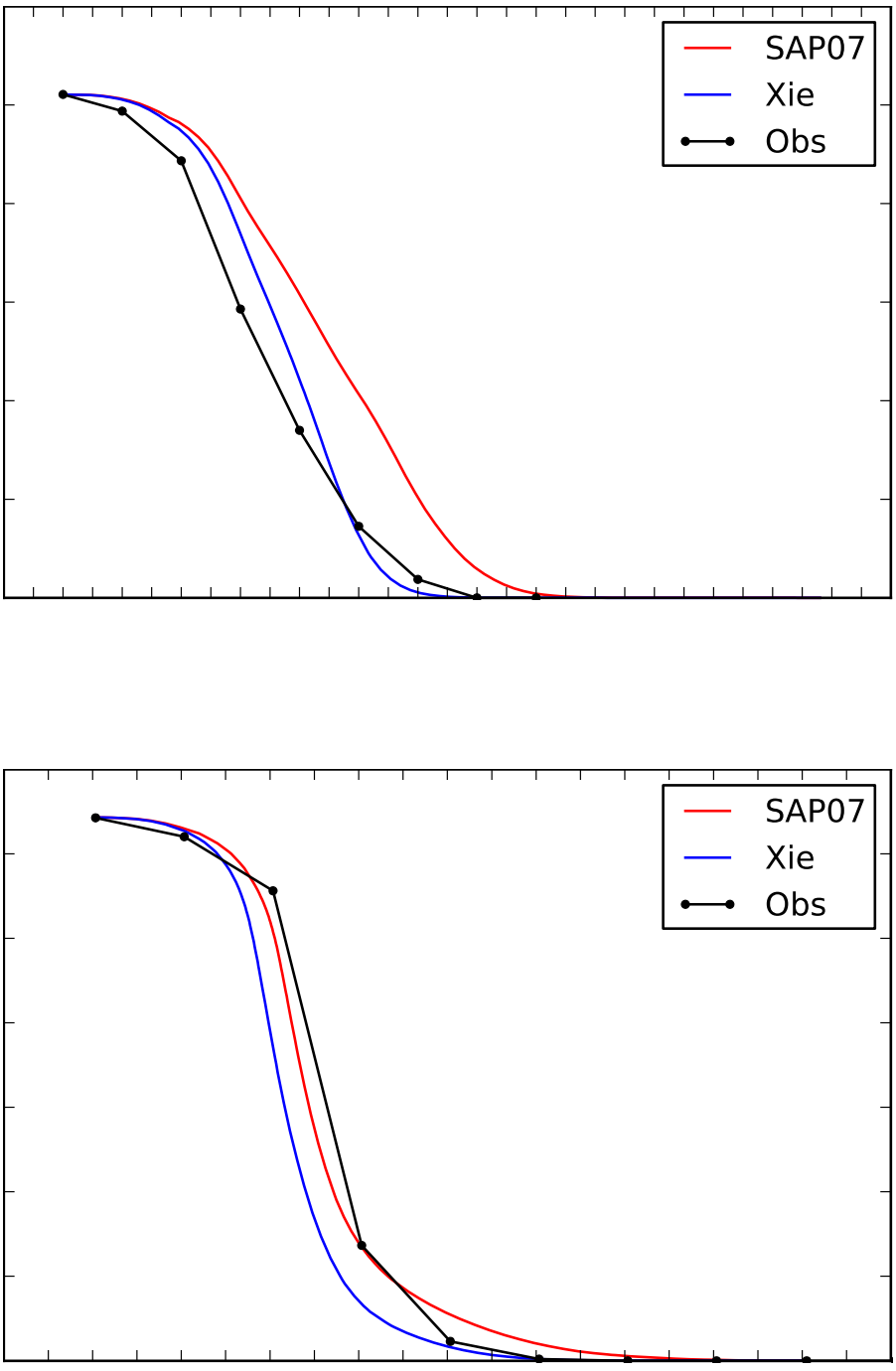

Figure 2.4. Isoprene concentration time profile for: (a) JN2381BLUE (High NO_X) and (b) JN2697RED (Lower NO_X) experiments.

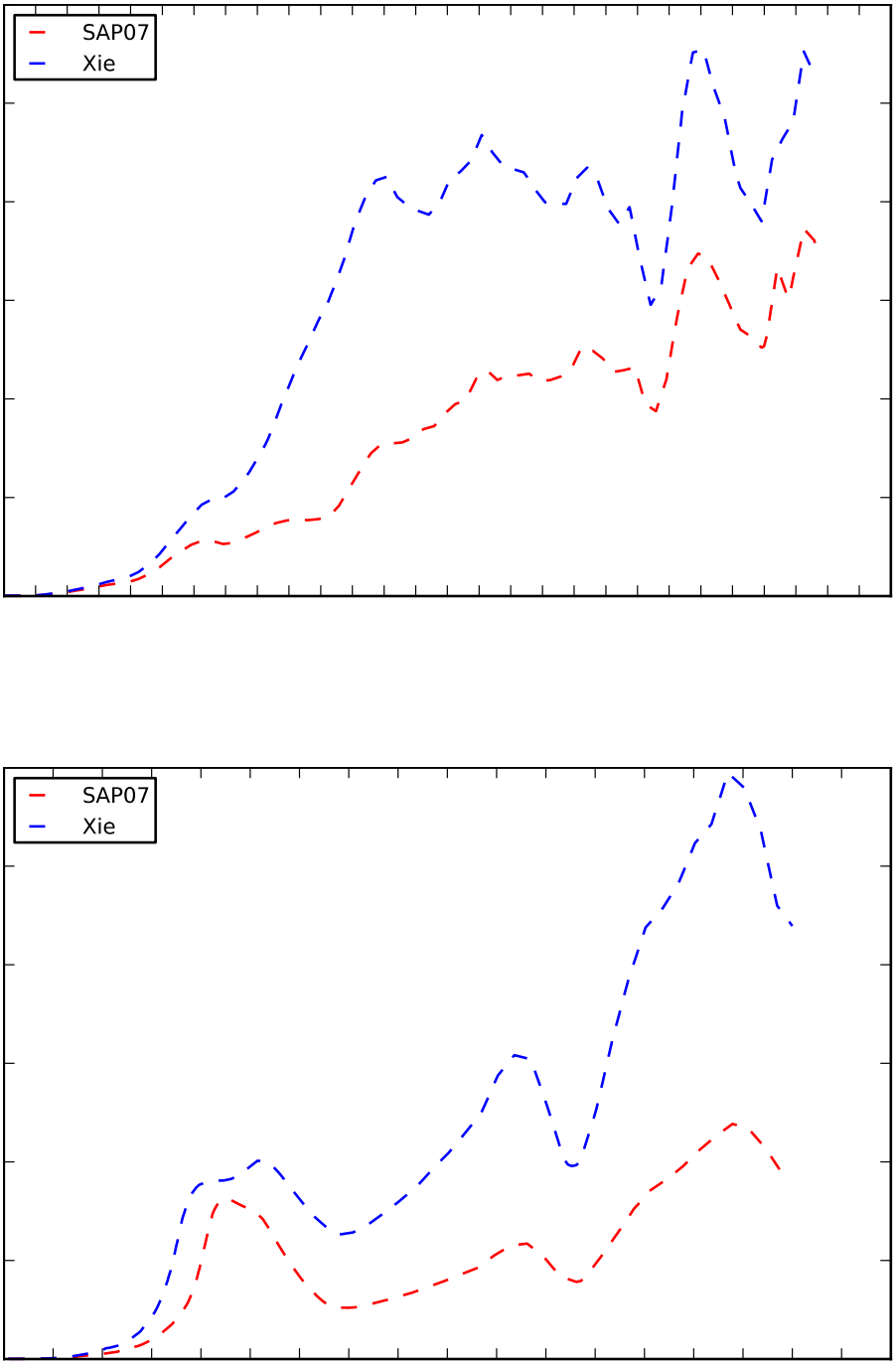

Figure 2.5. OH concentration time profile for: (a) JN2381BLUE (High NO_X) and (b) JN2697RED (Lower NO_X) experiments.

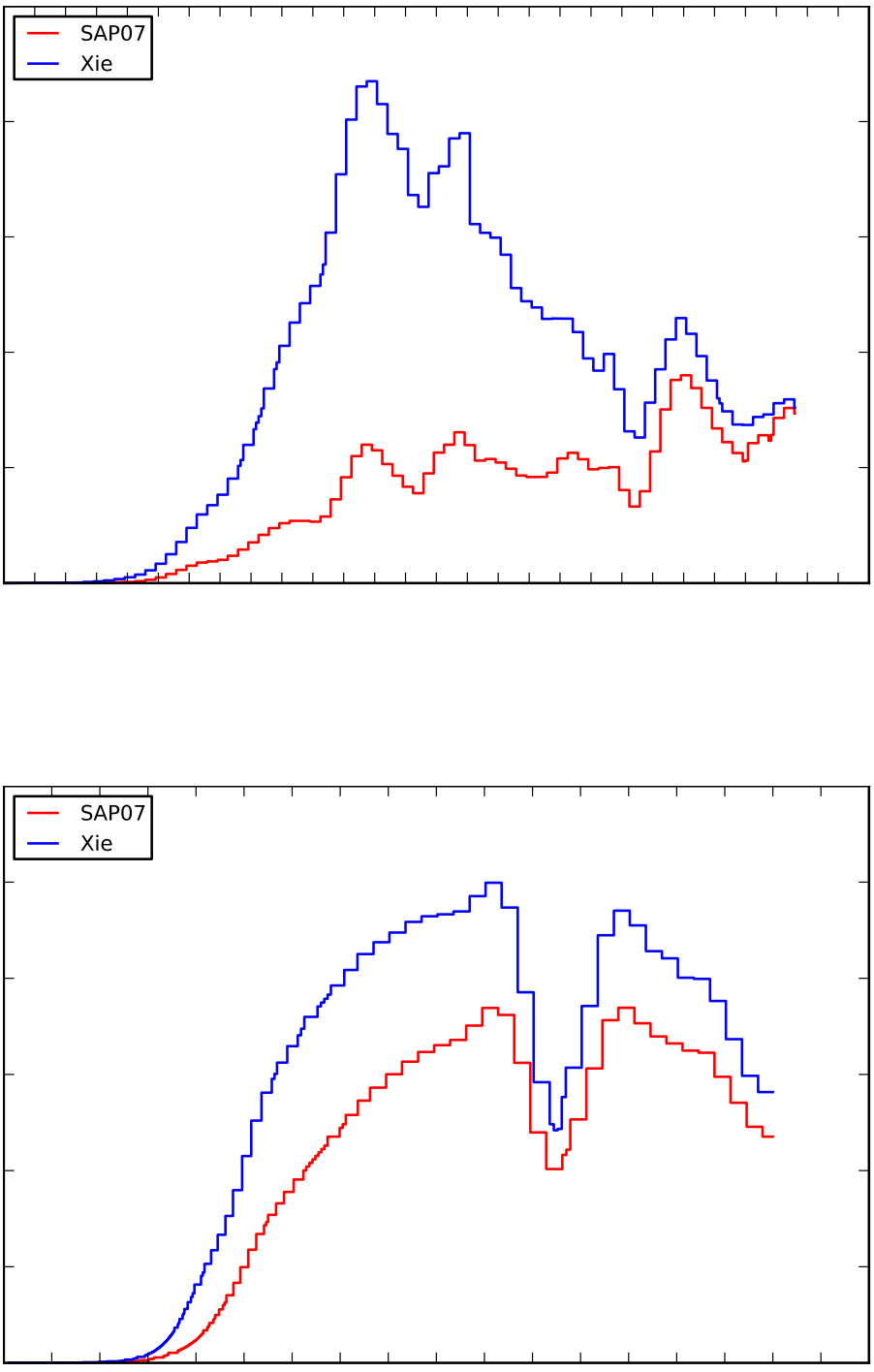

Figure 2.6. VOCs and isoprene reaction rate against OH time series for: (a) JN2381BLUE (High NO_X) and (b) JN2697RED (Lower NO_X) experiments.

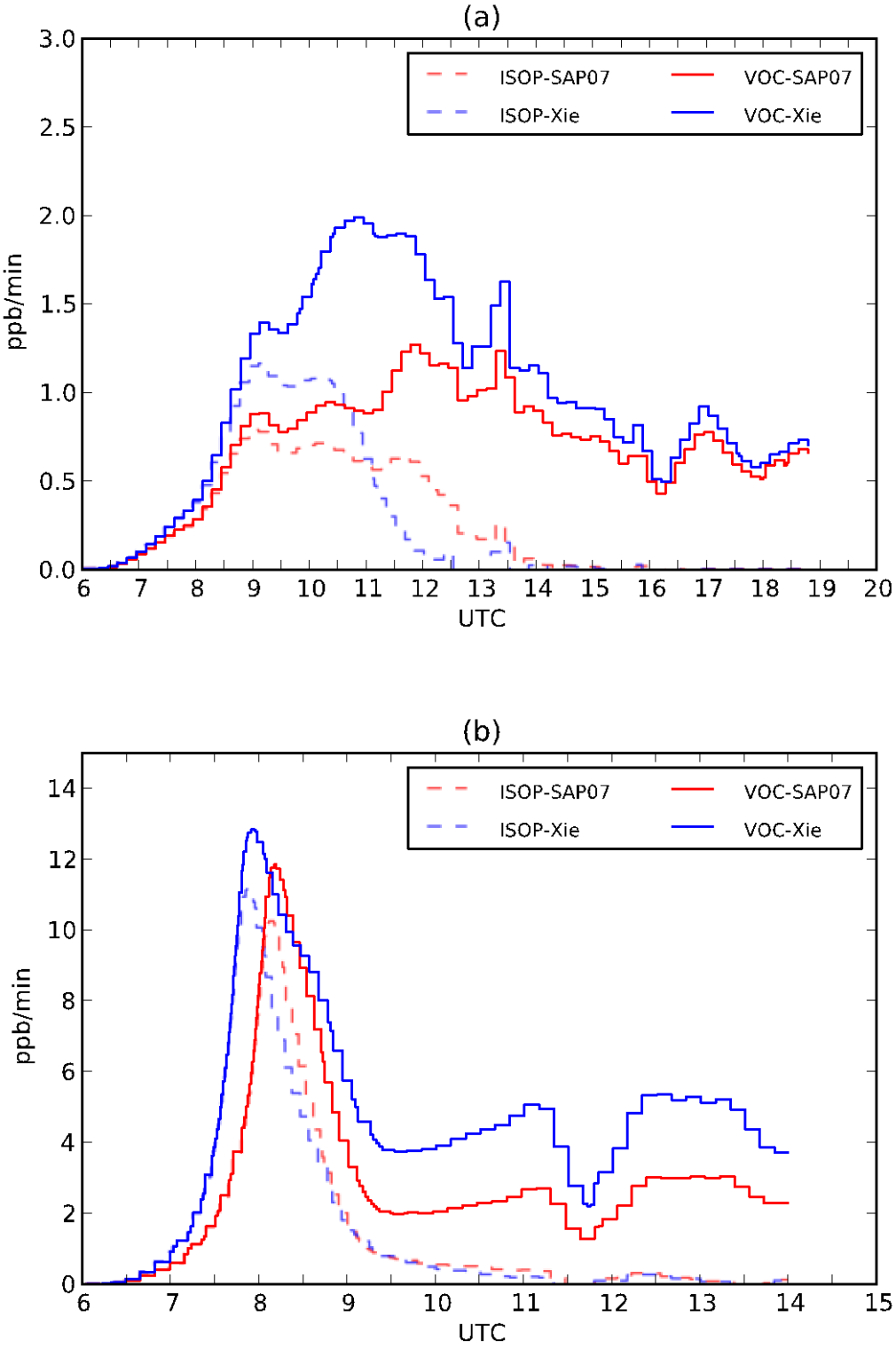

Figure 2.7. HO_2 production rate from aldehyde time series for: (a) JN2381BLUE (High NO_X) and (b) JN2697RED (Lower NO_X) experiments.

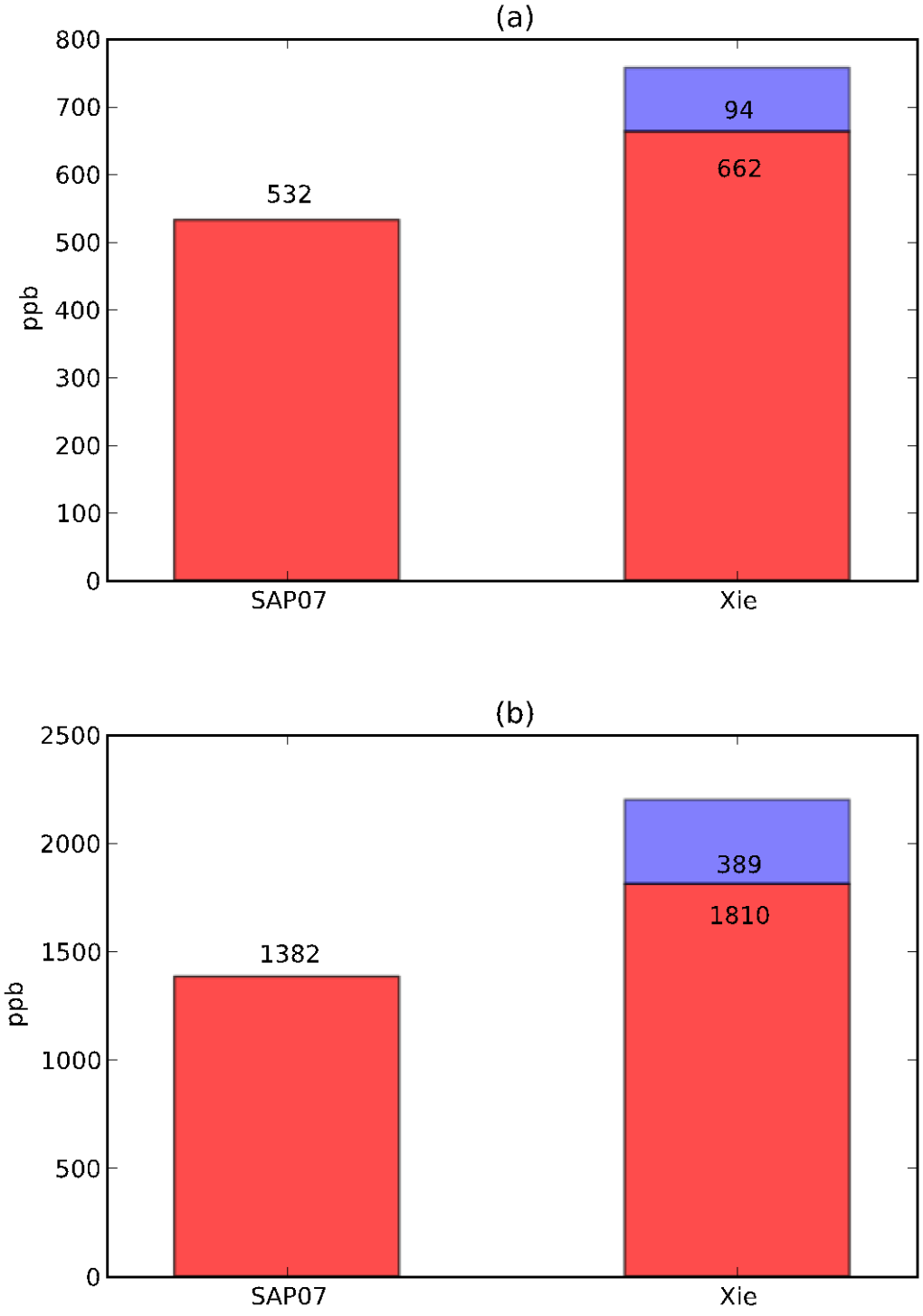

Figure 2.8. Comparison of Total OH+VOC reactions IRR: (a) JN2381BLUE (High NO_X) and (b) JN2697RED (Lower NO_X) experiments.

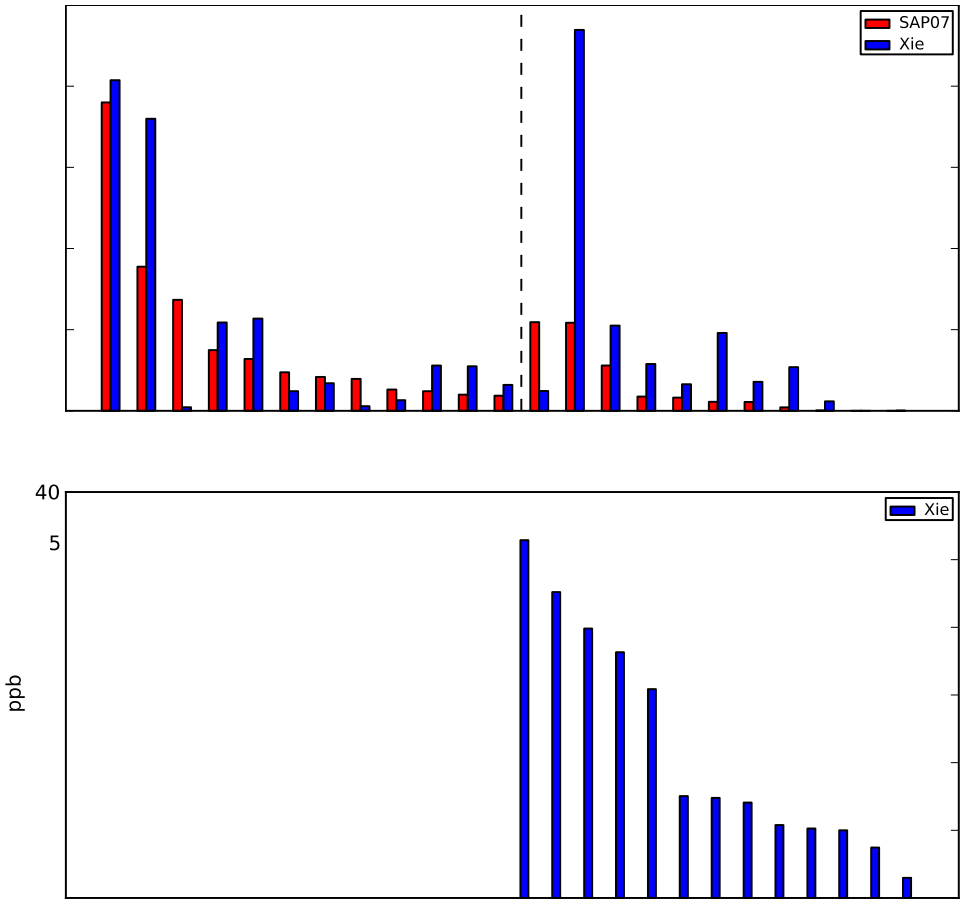

Figure 2.9. Detailed comparison of mass through various VOC+OH reaction pathways for JN2381BLUE (High NO_X) experiments.

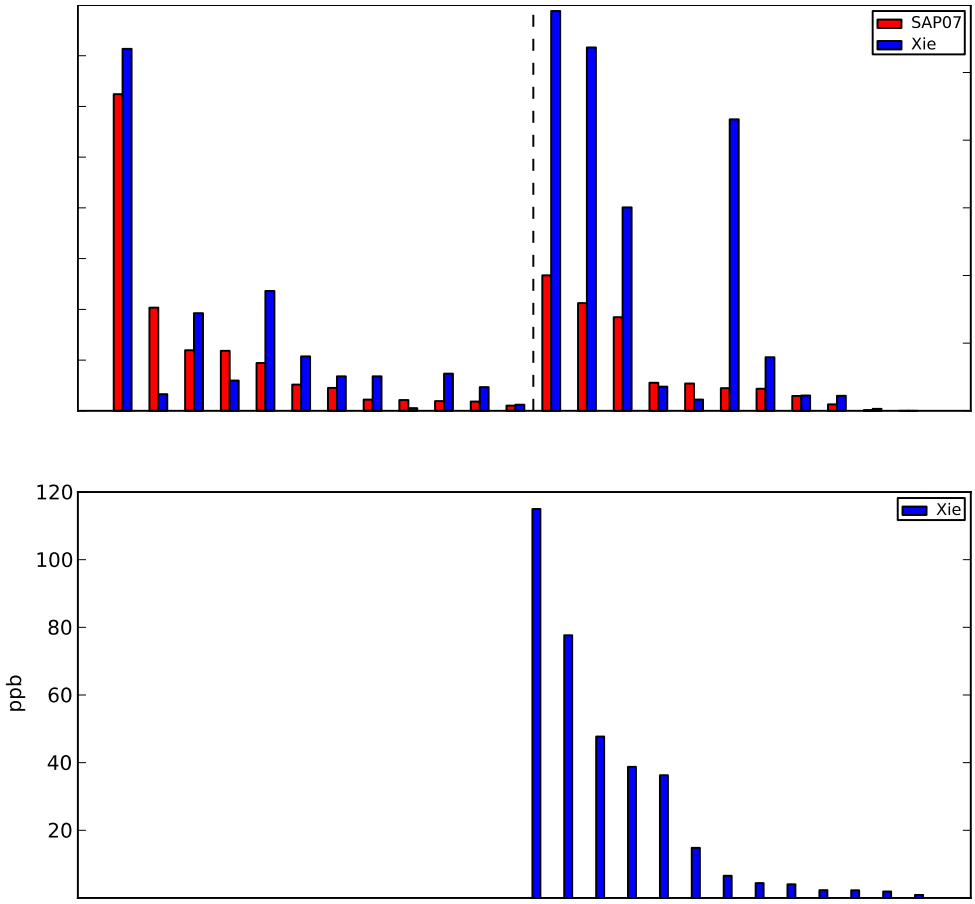

Figure 2.10. Detailed comparison of mass through various VOC+OH reaction pathways for JN2697RED (Lower NO_X) experiments.

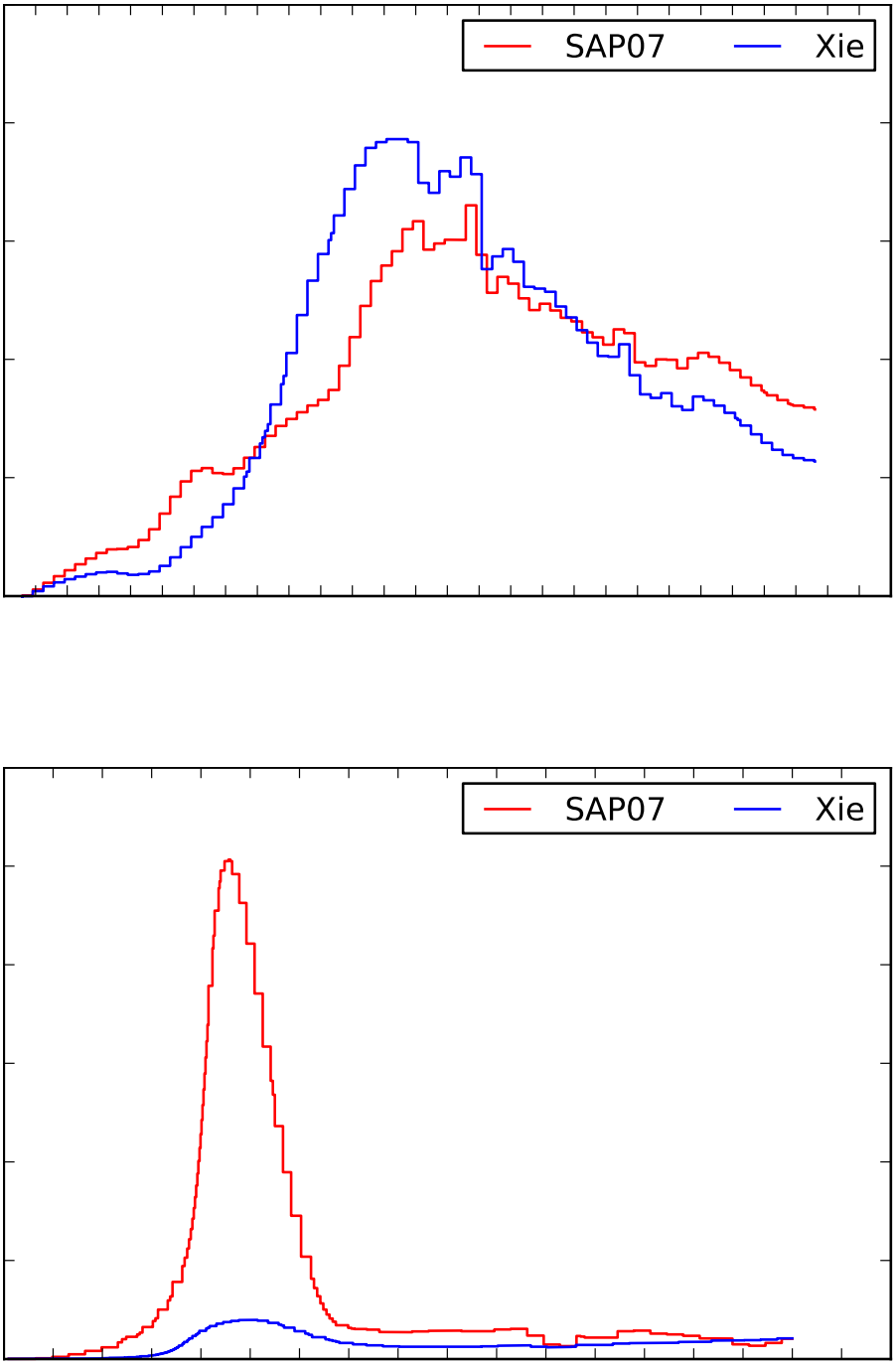

Figure 2.11. Nitrogen loss reaction rate time series through deposition of HNO_3 and nitrogen loss (XN): (a) JN2381BLUE (High NO_X) and (b) JN2697RED (Lower NO_X) experiments

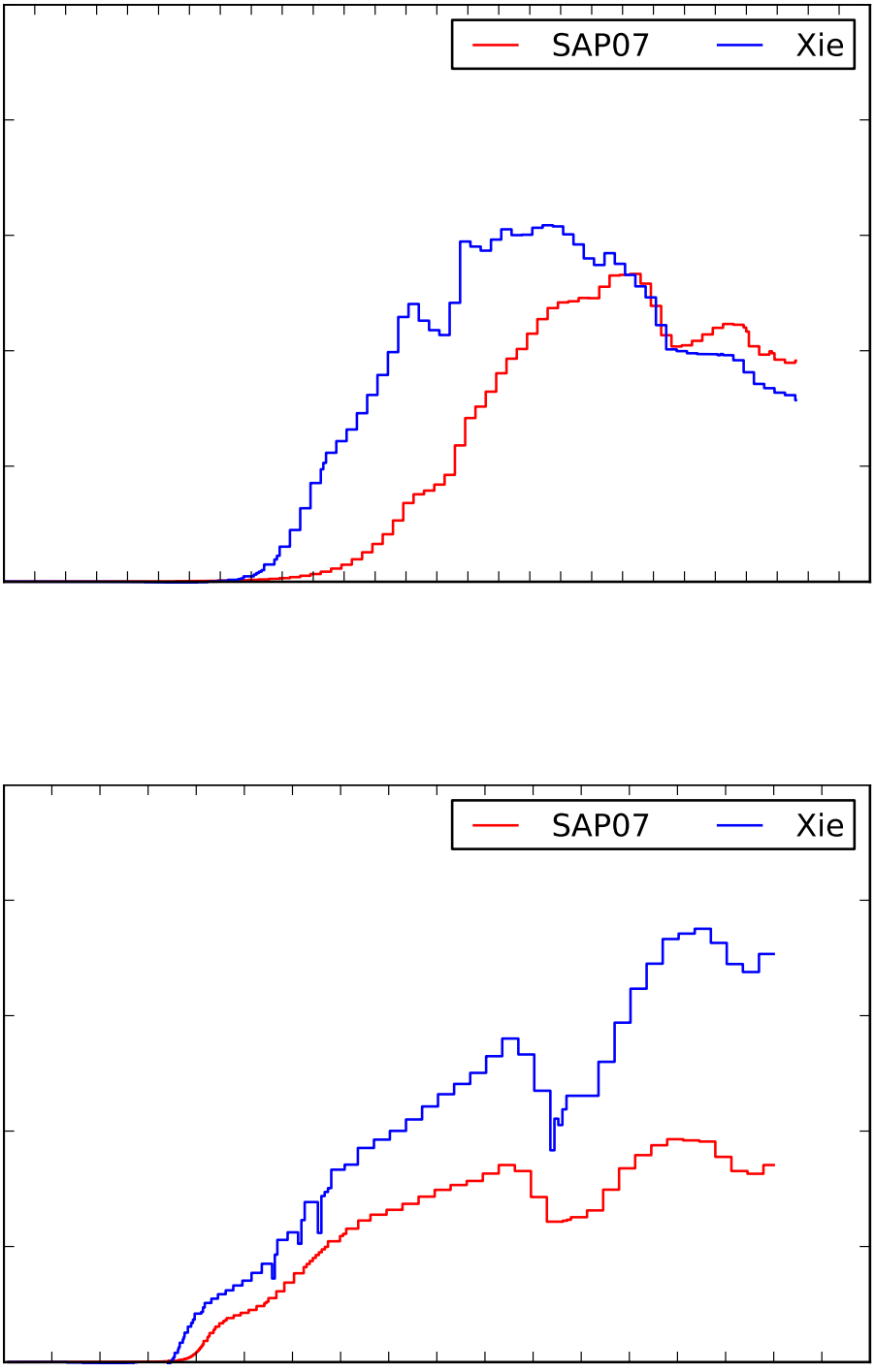

Figure 2.12. NO_X recycling rate time series from oxidized form NO_2: (a) JN2381BLUE (High NO_X) and (b) JN2697RED (Lower NO_X) experiments.

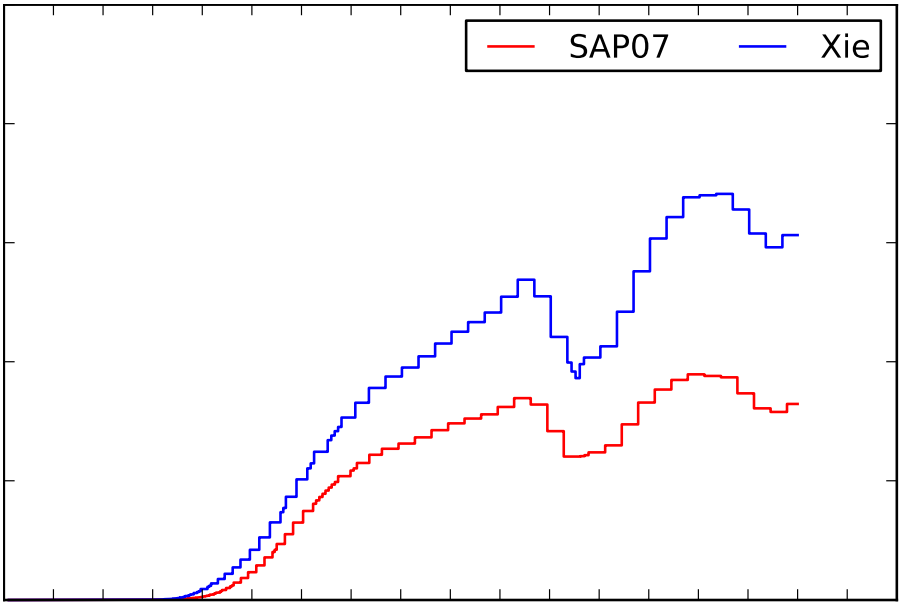

Figure 2.13. NO_2 recycling rate from PANs for JN2697RED (Lower NO_X) experiment.

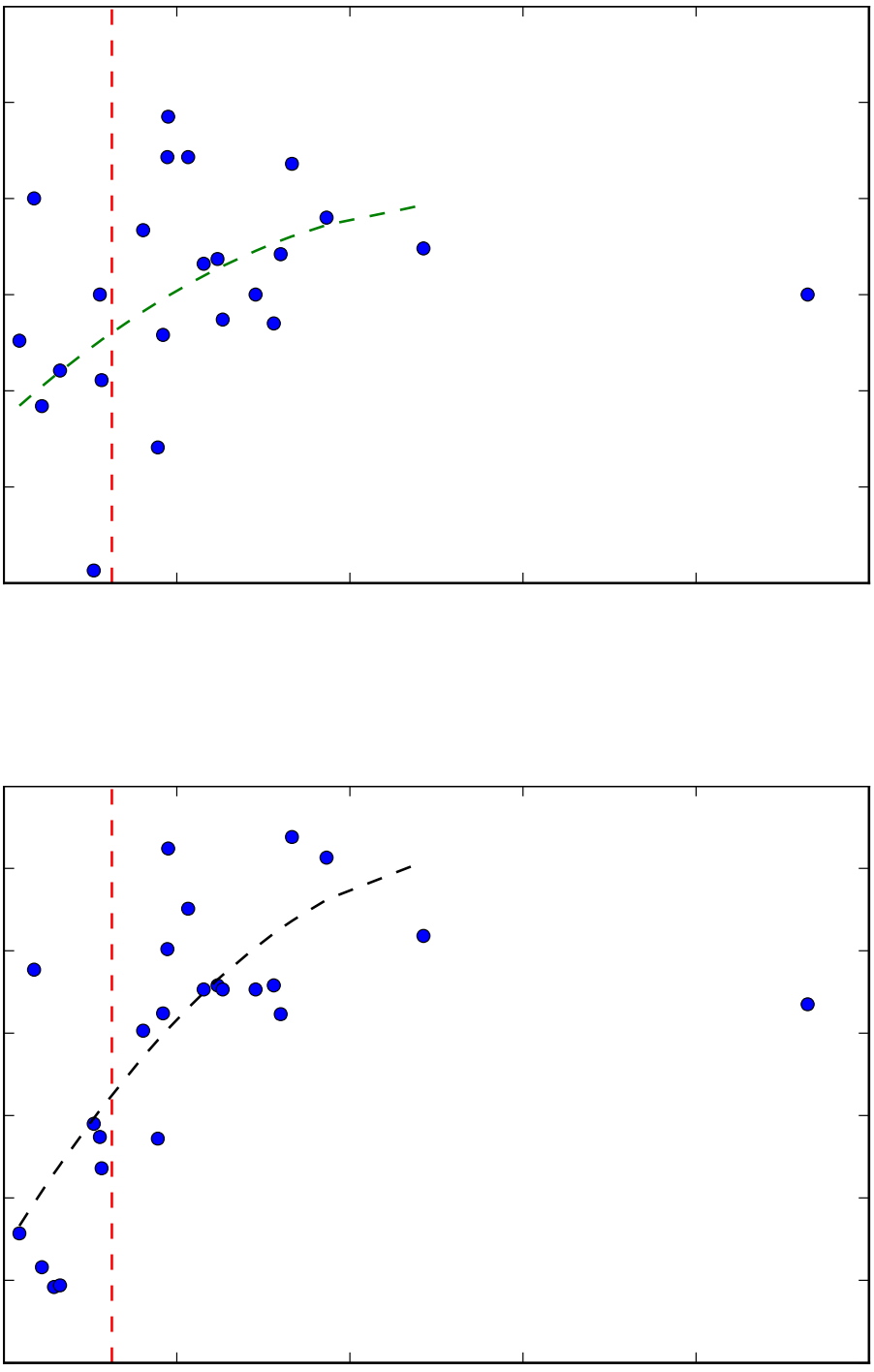

Figure 2.14. Radical cycle relative difference with regard to initial isoprene:NOX ratios: (a) OH cycle (b) NO cycle

Table 2.1. Characterization run experiments- initial concentration

Date/side	Compound injected	Injection (ppm)	Initial NOx (ppm)	Initial NO (ppm)	Initial NO2 (ppm)
OC0984BLUE	HCHO	0.96	0.5	0.35	0.15
ST3097RED	HCHO	2	0.32	0.27	0.05
ST2396RED	HCHO	0.5	0.33	0.28	0.05
ST2396BLUE	HCHO	1	0.33	0.28	0.05
JL1588RED	HCHO	0.79	0.31	0.22	0.09
JL1588BLUE	HCHO	0.43	0.3	0.21	0.09
AU2497RED	ETHENE	1.92	0.32	0.29	0.03
AU2497BLUE	ETHENE	1.84	0.32	0.29	0.03
AU2393BLUE	ETHENE	0.49	0.33	0.28	0.05
AU1688BLUE	ETHENE	0.97	0.41	0.34	0.07
AU1092RED	METHANE	500	0.35	0.28	0.07
AU1092BLUE	METHANE	250	0.35	0.28	0.07
AU0197RED	METHANE	500	0.35	0.3	0.05
AU0197BLUE	METHANE	250	0.34	0.29	0.05
ST3097BLUE	CO	250	0.33	0.28	0.05
AU3093BLUE	CO	100	0.32	0.28	0.04

Note: Date/side trailing code 'RED' and 'BLUE' denote the side of Dual chamber where the experiment was operated.

Table 2.2. Isoprene experiments - initial injected species and concentration

Isoprene runs – initial injected species and concentration.

Date/Side	ISOP/NOx (ppm/ppm)	Initial ISOP (ppm)	Initial NOx (ppm)	Initial NO (ppm)	Initial NO2 (ppm)
JN1793BLUE	0.18	0.1	0.54	0.47	0.07
JN1793RED	0.35	0.19	0.54	0.47	0.07
JL1780RED	0.44	0.2	0.46	0.36	0.1
JN2381BLUE	0.58	0.26	0.45	0.32	0.13
JL2381RED	0.65	0.28	0.43	0.35	0.08
JN2381RED	1.04	0.46	0.44	0.31	0.13
JL1780BLUE	1.11	0.52	0.47	0.36	0.11
JN2697BLUE	1.13	0.38	0.34	0.27	0.07
JN2592RED	1.61	0.58	0.36	0.31	0.05
OC1596BLUE	1.78	0.58	0.33	0.29	0.04
OC1596RED[a]	1.84	0.6	0.33	0.28	0.04
AU0897RED	1.89	1.28	0.68	0.59	0.09
AU1597BLUE	1.9	1.58	0.83	0.78	0.06
JN0298BLUE	2.13	1.5	0.7	0.58	0.12
ST0799BLUE	2.31	1.62	0.7	0.69	0.01
ST1199BLUE	2.47	1.5	0.61	0.6	0.01
JN2996RED	2.53	1.02	0.4	0.33	0.07
AU1196BLUE	2.91	0.98	0.34	0.29	0.04
JN2996BLUE	3.12	1.26	0.4	0.34	0.07
ST2496RED	3.2	2.06	0.64	0.57	0.07
JN2592BLUE	3.33	1.2	0.36	0.32	0.04
JN2697RED	3.73	1.29	0.35	0.28	0.07
OC0697RED	4.85	3.12	0.64	0.56	0.08
ST1199RED	9.29	1.56	0.17	0.16	0.01

[a] 200 ppm CO also injected in this experiment.

Table 2.3. Summary of O_3 peak model performance statistics

Experiment	Condition	Mechanism	NMB (%)	R^2	P value
N = 8	High NO_x	SAPRC07	−9.80	0.13	0.38
		Xie	−2.00	0.08	0.32
N = 16	Low NO_x	SAPRC07	3.42	0.85	3.09E-07
		Xie	9.44	0.79	4.00E-06

Table 2.4. Summary of crossover time statistics.

Experiment	Condition	Mechanism	NMB (%)	R^2	P value
N = 8	High NO_x	SAPRC07	−5.45	0.02	0.73
		Xie	−14.94	0.03	0.68
N = 16	Low NO_x	SAPRC07	−22.12	0.76	1.06E-05
		Xie	−29.73	0.67	9.62E-05

Table 2.5. Selected study cases initial condition and O3 peak concentration

Experiment	Initial ISOP:NOX (ppm/ppm)	Initial isoprene (ppm)	Initial NOX (ppm)	O3 peak (ppm)	O3 max (ppm)
JN2381BLUE	0.58	0.26	0.45	0.85	0.85
JN2697RED	3.73	1.29	0.35	0.57	0.75

Note: Here only the measured values of the first ozone peak are shown.

Table 2.6. The initial steps of isoprene oxidation by OH for the SAPRC07 and Xie mechanisms

The initial steps of isoprene oxidation by OH for the SAPRC07 and Xie mechanisms.

Mechanism	Reactions	Rate
SAPRC07	ISOP + OH → 0.986*RO2C + 0.093*RO2XC + 0.093*zRNO3 + 0.907*xHO2 + 0.624*xHCHO + 0.23*xMACR + 0.32*xMVK + 0.357*xIPRD + yR6OOH + 0.167*XC	k[BE06]
	xHO2 + NO → HO2 + NO	k[BR07]
	RO2C + NO → NO2	k[BR07]
Xie	**ISOP + OH → ISOPO2 + ISOPRXN**	k[BE06]
	ISOPO2 + NO → 0.40*MVK + 0.26*MACR + 0.883*NO2 + 0.07*ISOPND + 0.047*ISOPNB + 0.66*HCHO + 0.10*HC5 + 0.043*ARO2 + 0.08*DIBOO + 0.803*HO2	k[BR07]

Table 2.7. OH radical budget for: (Upper Row) JN2381BLUE (High NO_X) and (Lower Row) JN2697RED (Lower NO_X) experiments.

Experiment	Mechanism	New OH (ppb)			OH + VOC (ppb)	OH + NO2 (ppb)	OH cycle (unitless)
		Inorganic	Organic	Total			
JN2381BLUE	SAPRC07	22.6	56.2	78.8	532	141	8.9
	Xie	27.2	80.8	108	592	195	8.3
JN2697RED	SAPRC07	45.5	476	522	1382	13.9	2.5
	Xie	66.0	538	604	1749	29.9	3.3

Note: OH cycle number = amount of OH reacted/new OH.

Table 2.8. NO_2 production IRR (ppb) from NO conversion and recycling from NO_Z: (Upper Row) JN2381BLUE (High NO_X) and (Lower Row) JN2697RED (Lower NO_X) experiments.

Experiment	Mechanism	NO → NO_2 (ppb)				NO_z → NO_2 (ppb)	Total NO_2 (ppb)
		NO + XO2	NO + NO3	NO + O_3	Total		
JN2381BLUE	SAPRC07	1191	2884	27,575	30,208	12,061	42,269
	Xie	1357	3257	23,866	26,851	16,678	43,529
JN2697RED	SAPRC07	2138	93	4537	6721	9686	16,407
	Xie	2776	335	5972	8915	16,860	25,775

Note: NO to NO_2 conversion includes conversion by XO2 (=HO2 + RO2), NO3 and O_3.

Table 2.9. NO cycle calculation specifics: (Upper Row) JN2381BLUE (High NO_X) and (Lower Row) JN2697RED (Lower NO_X) experiments

Experiment	Mechanism	New NO (ppb)				NO → NO_2 (ppb)	NO cycle (unitless)
		Injection	HONO	WHNO3	Total		
JN2381BLUE	SAPRC07	445	8	4	457	30,215	66.2
	Xie	445	8	4	457	26,886	58.9
JN2697RED	SAPRC07	342	1	0	343	6723	19.8
	Xie	342	1	0	343	8955	26.1

Note: NO cycle number = amount of NO to NO_2 conversion/new NO.

E. References

[1] A. Guenther, T. Karl, P. Harley, C. Wiedinmyer, P. I. Palmer, C. Geron, Estimates of global terrestrial isoprene emissions using MEGAN (Model of Emissions of Gases and Aerosols from Nature) (2006). doi:10.5194/acpd-6-107-2006.

[2] W. L. Chameides, R. W. Lindsay, J. Richardson, C. S. Kiang, The role of biogenic hydrocarbons in urban photochemical smog: Atlanta as a case study., Science (New York, N.Y.) 241 (1988) 1473–1475. doi:10.1126/ science.3420404.

[3] G. Li, R. Zhang, J. Fan, X. Tie, Impacts of biogenic emissions on photochemical ozone production in Houston, Texas, Journal of Geophysical Research 112 (D10) (2007) D10309. doi:10.1029/2006JD007924. URL http://doi.wiley.com/10.1029/2006JD007924

[4] M. Claeys, B. Graham, G. Vas, W. Wang, R. Vermeylen, V. Pashynska, J. Cafmeyer, P. Guyon, M. O. Andreae, P. Artaxo, W. Maenhaut, Formation of secondary organic aerosols through photooxidation of isoprene, Science 303 (2004) 1173–1176. doi:10.1126/science.1092805.

[5] E. Edney, T. Kleindienst, M. Jaoui, M. Lewandowski, J. Offenberg, W. Wang, M. Claeys, Formation of 2-methyl tetrols and 2-methylglyceric acid in secondary organic aerosol from laboratory irradiated isoprene/NOX/SO2/air mixtures and their detection in ambient PM2.5 samples collected in the eastern United States, Atmospheric Environment 39 (29) (2005) 5281–5289. doi:10.1016/j.atmosenv.2005.05.031. URL http://linkinghub.elsevier.com/retrieve/pii/ 325 S1352231005004875

[6] M. Hallquist, J. C. Wenger, U. Baltensperger, Y. Rudich, D. Simpson, M. Claeys, J. Dommen, The formation, properties and impact of secondary organic aerosol: current and emerging issues, Atmos. Chem. Phys. 9 (2009) 5155–5236. doi:10.5194/acp-9-5155-2009.

[7] J. H. Kroll, N. L. Ng, S. M. Murphy, R. C. Flagan, J. H. Seinfeld, Secondary organic aerosol formation from isoprene photooxidation., Environmental science & technology 40 (2006) 1869–1877. doi:10.1021/es0524301.

[8] Y. Lin, H. Zhang, H. O. T. Pye, Z. Zhang, W. J. Marth, S. Park, M. Arashiro, Epoxide as a precursor to secondary organic aerosol formation from isoprene photooxidation in the presence of nitrogen oxides, Proceedings of the ... doi:10.1073/pnas.1221150110/-/DCSupplemental.www. pnas.org/cgi/doi/10.1073/pnas.1221150110. URL http://www.pnas.org/content/110/17/6718.short

[9] F. Paulot, J. D. Crounse, H. G. Kjaergaard, A. Kurten, J. M. St Clair, J. H. Seinfeld, P. O. Wennberg, Unexpected epoxide formation in the gas-phase photooxidation of isoprene., Science (New York, N.Y.) 325 (5941) (2009) 730–3. doi:10.1126/science.1172910. URL http://www.ncbi.nlm.nih.gov/pubmed/19661425

[10] J. D. Surratt, S. M. Murphy, J. H. Kroll, N. L. Ng, L. Hildebrandt, A. Sorooshian, R. Szmigielski, R. Vermeylen, W. Maenhaut, M. Claeys, R. C. Flagan, J. H. Seinfeld, Chemical composition of secondary organic aerosol formed from the photooxidation of isoprene., The journal of physical chemistry. A 110 (2006) 9665–9690. doi:10.1021/jp061734m.

[11] J. D. Surratt, M. Lewandowski, J. H. Offenberg, M. Jaoui, T. E. Kleindienst, E. O. Edney, J. H. Seinfeld, Effect of acidity on secondary organic aerosol formation from isoprene., Environmental science & technology 41 (2007) 5363–5369. doi:Doi10.1021/Es0704176.
[12] J. D. Surratt, A. W. H. Chan, N. C. Eddingsaas, M. Chan, C. L. Loza, A. J. Kwan, S. P. Hersey, R. C. Flagan, P. O. Wennberg, J. H. Seinfeld, Reactive intermediates revealed in secondary organic aerosol formation from isoprene., Proceedings of the National Academy of Sciences of the United States of America 107 (15) (2010) 6640–5. doi:10.1073/pnas.0911114107. URL http://www.pubmedcentral.nih.gov/articlerender.fcgi?artid=2872383&tool=pmcentrez&rendertype=abstract
[13] Y. Xie, F. Paulot, W. P. L. Carter, C. G. Nolte, D. J. Luecken, W. T. Hutzell, P. O. Wennberg, R. C. Cohen, R. W. Pinder, Understanding the impact of recent advances in isoprene photooxidation on simulations of regional air quality, Atmospheric Chemistry and Physics 13 (16) (2013) 8439–8455. doi:10.5194/acp-13-8439-2013. URL http://www.atmos-chem-phys.net/13/8439/2013/
[14] W. P. L. Carter, Development of the saprc-07 chemical mechanism and updated ozone reactivity scales, Report to the California Air Resources Board, Contract No. 03–18, 06-408, and 07-730, 27 January 2010b (available at: http://www.engr.ucr.edu/˜carter/SAPRC/).
[15] W. P. Carter, Development of a condensed saprc-07 chemical mechanism, Atmospheric Environment 44 (40) (2010) 5336 – 5345, atmospheric Chemical Mechanisms: Selected Papers from the 2008 Conference. doi:http://dx.doi.org/10.1016/j.atmosenv.2010.01.024. URL http://www.sciencedirect.com/science/article/pii/ S1352231010000622
[16] W. Hutzell, D. Luecken, K. Appel, W. Carter, Interpreting predictions from the SAPRC07 mechanism based on regional and continental simulations, Atmospheric Environment 46 (2012) 417–429. URL http://linkinghub.elsevier.com/retrieve/pii/S135223101100971Xhttp://www.sciencedirect.com/science/article/pii/S135223101100971X
[17] C. R. Hoyle, T. Berntsen, G. Myhre, I. S. A. Isaksen, Secondary organic aerosol in the global aerosol -chemical transport model Oslo CTM2, Atmospheric Chemistry and Physics 7 (2007) 5675–5694. doi:10.5194/ acp-7-5675-2007. URL <GotoISI>://000251239500014
[18] D. K. Henze, J. H. Seinfeld, Global secondary organic aerosol from isoprene oxidation, Geophysical Research Letters 33. doi:10.1029/2006GL025976.
[19] A. G. Carlton, C. Wiedinmyer, J. H. Kroll, A review of Secondary Organic Aerosol (SOA) formation from isoprene, Atmospheric Chemistry and Physics Discussions 9 (2) (2009) 8261–8305. doi:10.5194/ acpd-9-8261-2009. URL http://www.atmos-chem-phys-discuss.net/9/8261/2009/
[20] K. M. Foley, S. J. Roselle, K. W. Appel, P. V. Bhave, J. E. Pleim, T. L. Otte, R. Mathur, G. Sarwar, J. O. Young, R. C. Gilliam, C. G. Nolte, J. T. Kelly, A. B. Gilliland, J. O. Bash, Incremental testing of the Community Multiscale Air Quality (CMAQ) modeling system version 4.7, Geoscientific Model Development 3 (2010) 205–226. doi:10.5194/gmd-3-205-2010.

[21] M. Azzi, S. J. White, D. E. Angove, I. M. Jamie, A. Kaduewela, Evaluation of the SAPRC-07 mechanism against CSIRO smog chamber data, Atmospheric Environment 44 (14) (2010) 1707–1713. doi:10.1016/j.atmosenv.2010.02.013. URL http://linkinghub.elsevier.com/retrieve/pii/ S1352231010001196
[22] H. E. Jeffries, R. M. Kamens, K. Sexton, Early history and rationale for outdoor chamber work at the University of North Carolina, Environmental Chemistry 10 (4) (2013) 349. doi:10.1071/EN13901. URL http://www.publish.csiro.au/?paper=EN13901
[23] H. E. Jeffries, D. L. Fox, R. M. Kamens, outdoor smog chamber studies: light effects relative to indoor chambers, Environ. Sci. Technol. 10 (1006).
[24] H. M. Parikh, H. E. Jeffries, K. G. Sexton, D. J. Luecken, R. M. Kamens, W. Vizuete, Evaluation of aromatic oxidation reactions in seven chemical mechanisms with an outdoor chamber, Environmental Chemistry 10 (3) (2013) 245. doi:10.1071/EN13039. URL http://www.publish.csiro.au/?paper=EN13039 http://www.publish.csiro.au/view/journals/dsp_journal_fulltext.cfm?nid=188&f=EN13039
[25] H. E. Jeffries, I. Voicu, K. Sexton, Experimental tests of reactivity and reevaluation of the carbon bond four photochemical reaction mechanism: Final report for cooperative agreement r828906, Tech. rep. (2002 (USEPA)).
[26] H. E. Jeffries, Photochemical air pollution, in: H. B. Singh (Ed.), Composition, Chemistry, and Climate of the Atmosphere, John Wiley and Sons, Inc, 1995.
[27] B. H. Henderson, W. Vizuete, H. E. Jeffries, The python environment for reaction mechanism/mathematics (permm), in: Poster at the 8th Annual CMAS Conference, Chapel Hill, NC, 2009.
[28] R. Crouse, Integrated reaction rate analysis of ozone production in a photochemical oxidant model, Master's thesis, University of North Carolina at Chapel Hill (1990).
[29] J. Peeters, J.-F. Muller, HO(x) radical regeneration in isoprene oxidation via peroxy radical isomerisations. II: experimental evidence and global impact., Physical chemistry chemical physics : PCCP 12 (42) (2010) 14227–35. doi:10.1039/c0cp00811g. URL http://www.ncbi.nlm.nih.gov/pubmed/20882226
[30] H. Fuchs, A. Hofzumahaus, F. Rohrer, B. Bohn, T. Brauers, H.-P. Dorn, R. Haseler, F. Holland, M. Kaminski, X. Li, K. Lu, S. Nehr, R. Tillmann, R. Wegener, A. Wahner, Experimental evidence for efficient hydroxyl radical regeneration in isoprene oxidation, Nature Geoscience (2013) 10– 13doi:10.1038/ngeo1964. URL http://www.nature.com/doifinder/10.1038/ngeo1964
[31] J. D. Crounse, F. Paulot, H. G. Kjaergaard, P. O. Wennberg, Peroxy radical isomerization in the oxidation of isoprene, Physical chemistry chemical physics : PCCP 13 (2011) 13607–13613. doi:10.1039/c1cp21330j.
[32] G. da Silva, C. Graham, Z.-F. Wang, Unimolecular beta-hydroxyperoxy radical decomposition with OH recycling in the photochemical oxidation of isoprene., Environmental science & technology 44 (1) (2010) 250–6. doi: 10.1021/es900924d. URL http://www.ncbi.nlm.nih.gov/pubmed/19943615

3. Heterogeneous reactions of isoprene-derived epoxides: reaction probabilities and molar SOA yield estimates

A. INTRODUCTION

Isoprene (2-methyl-,1,3-butadiene, C_5H_8) is the most abundant nonmethane hydrocarbon present in the atmosphere and has large potential effects on air quality and radiative forcing.[11] The formation of secondary organic aerosol (SOA) from the photochemical oxidation of isoprene represents a significant source of fine aerosol mass ($PM_{2.5}$),[12, 13] especially in the southeastern United States during summer.[14-16] Epoxides formed from isoprene oxidation have been shown to be a critical precursor to isoprene-derived SOA.[17, 18] *Trans*-β-isoprene epoxydiols (IEPOX, $C_5H_{10}O_3$) and to a lesser extent methacrylic acid epoxide (MAE, $C_4H_6O_3$) have the capability to produce SOA through reactive uptake onto atmospheric $PM_{2.5}$.[16] In the southeast the condensed-phase reactions can form a variety of "tracer" species that contribute to the SOA burden (e.g., organosulfates, 2-methyltetrols, C_5-alkene triols, and 2-methylglyceric acid).[18-20] Isoprene-derived epoxides are thought to form in appreciable quantities in isoprene-rich regions and have been observed with mixing ratios in excess of 3 ppbv for IEPOX and 50 pptv for MAE.[17, 18]

The heterogeneous reactions of these epoxides required for subsequent SOA formation remain poorly constrained. Specifically, the rate of heterogeneous uptake – often reported as the gas-aerosol reaction probability (ɣ – also called the reactive uptake coefficient) – has only recently started to be explored through direct measurements.[5] ɣ is defined as the number of gas-phase molecules removed by the aerosol phase over the total number of molecules striking the aerosol surface. This parameter is particularly convenient for modeling these reactions as it can be efficiently incorporated into regional and global models.[21, 22] Most epoxide ɣ estimates to this point have relied on indirect parameterizations based on Henry's Law partitioning theory and reaction rates for a few aerosol-phase epoxide reactions.[21, 23]

Equally important to ɣ in terms of SOA production from IEPOX and MAE is the molar fraction of these species on the aerosol phase that produce SOA mass. We define this quantity as the molar SOA yield (α_{SOA}). In other words, α_{SOA} is the sum of the rates of all SOA tracer formation reactions relative to the heterogeneous rate of gas phase epoxide loss to particles, as we illustrate in equation 3.1.

$$\propto_{SOA} = \frac{\sum_{i=1}^{n} k_i[epoxide]_{(aq)}}{k_{het}[epoxide]_{(g)}} \qquad \text{(eqn. 3.1)}$$

where k_i is the rate constant for each value of *i*, and k_{het} refers to the heterogeneous rate of gas phase epoxide loss to particles.

Traditionally, epoxide SOA production studies have reported estimates of the SOA mass yield –an equilibrium parameter calculated as the mass of SOA produced relative to the amount of epoxide consumed or injected into the chamber.[19, 20] The mass yield can be related to α_{SOA} simply through conversion to molar units provided the mass fractions and identities of all SOA tracers are known.

We use the lack of epoxide heterogeneous constraints as motivation to investigate the heterogeneous kinetics of *trans*-β-IEPOX, which is the predominant isomer of IEPOX,[24] and MAE, as well as the extent to which the fraction lost to aerosols contribute to SOA.

B. METHODS

1. Epoxide Uptake Measurements.

We used entrained gas-aerosol flow reactors [5, 25, 26] to determine ɣ's for authentic *trans*-β-IEPOX and MAE. The reactor is a Pyrex glass flow reactor 1 m in length and with an 8 cm inner diameter coated with halocarbon wax (Halocarbon Products Corp., Series 1500) to inhibit wall-loss reactions. Synthetic procedures for generating authentic *trans*-β-IEPOX and MAE are described in the appendix [18, 27] Aerosols were generated using a custom built atomizer that outputs polydisperse aerosol in a nitrogen carrier flow at ~2 standard liters per minute (slpm). Atomizer solutions were chosen to match previous SOA chamber studies that showed significant SOA growth, which we describe below. Atomized aerosol were mixed with a nitrogen dilution flow of ~3 slpm and injected into the flow reactor through a side port at the top of the reactor perpendicular to the flow axis. Depending on the desired relative humidity (RH), the aerosol stream was sent through a diffusion dryer (TSI Inc., 3062) and the dilution flow passed through a water bubbler prior to addition into the flow reactor.

Trans-β-IEPOX and MAE were delivered to the reactor by flowing ~0.1 slpm of nitrogen over a 20 µg/mL solution of the epoxide in ethyl acetate. The epoxide was introduced to the aerosol stream through an injector rod inserted axially down the center of the flow reactor. This injector was moved along the length of the reactor to control the interaction time between the epoxide and the atomized aerosol. At the base of the reactor submicron (10 - 850 nm) aerosol number size distributions were measured through a perpendicular port with a scanning electrical mobility system with a differential mobility analyzer and mixing condensation particle counter (Brechtel Manufacturing Inc., SEMS v5.0 DMA MCPC). These number distributions where converted into total surface area concentrations which ranged between 18,000 and 65,000 $\mu m^2 cm^{-3}$ between different experiments. Epoxide levels were monitored through another perpendicular port using a time-of-flight chemical ionization mass spectrometer (Aerodyne Research Inc., ToF-CIMS) with both acetate and iodide reagent ion chemistries.[28, 29] ɣ estimates were consistent between the two reagent ions. The flow reactor RH was also measured at the base with a commercial RH/temperature sensor (Omega Engineering Inc., RH-USB).

The heterogeneous pseudo-first-order rate coefficient (k_{het}) for epoxide uptake on the aerosols was measured by moving the epoxide injector between six positions along the length of the flow reactor. A linear fit of the reaction time versus the natural log-averaged epoxide signal at each injector position yielded a slope equal to k_{total} which is the sum of k_{het} and the reaction rate coefficient of the epoxide on the reactor walls ($k_{total} = k_{het} + k_{wall}$). The slope of a linear fit of a second decay performed at the same RH in the absence of aerosols yields k_{wall} (typically <0.01 s^{-1}). Figure 3.1 shows the normalized time decays and the associated linear fit for both *trans*-β-IEPOX and MAE with and without aerosols present. Assuming plug flow conditions the difference between k_{total} and k_{wall} is k_{het}. In practice, however, we used an iterative correction to obtain a k_{het} that is corrected for non-plug flow conditions.[30] k_{het} was then converted to ɣ using equation 3.2 given the mean molecular speed of the epoxide molecule (ω) and the SEMS-reported total aerosol surface area concentration (S_a). A minimum of three ɣ measurements are used in all reported ɣ averages.

$$\gamma = \frac{4k_{het}}{S_a \omega} \qquad \text{(eqn. 3.2)}$$

2. Epoxide SOA Chamber Experiments.

Trans-β-IEPOX and MAE experiments were performed to assess the SOA growth under various RH and seed aerosol types. Briefly, IEPOX or MAE was injected into a dry (~5% RH) or humidified (~50% RH) 10-m^3 Teflon smog chamber that was pre-filled with ~35 µg/m^3 of inorganic seed aerosol as measured by the SEMS or a scanning mobility particle sizer with cylindrical differential mobility analyzer and condensation particle counter (TSI Inc., SMPS DMA 3081 CPC 3022). Seed aerosol were generated by atomizing one of three different solutions – 0.06 M $(NH_4)_2SO_4$, 0.06 M $(NH_4)_2SO_4$ + 0.06 M H_2SO_4, or 0.06 M $MgSO_4$ + 0.06 M H_2SO_4). ~15 mg of authentic *trans*-β-IEPOX or MAE standard was delivered to the seeded chamber by flowing ~5 slpm N_2 through a 60 °C heated glass manifold for 1 – 2 hours until the observed SOA mass concentration had stabilized (Figure 7.1).

C. RESULTS AND DISCUSSION

1. Flow Reactor Measurements of ɣ.

Table 3.1 summarizes the ɣ results for *trans*-β-IEPOX and MAE including the 1σ error for each measurement. Importantly, the aerosol and RH conditions chosen for the flow

reactor was representative of conditions that produced notable SOA growth in the chamber experiments. Table 3.1 also includes estimates of aerosol acidity obtained from the Extended AIM Aerosol Thermodynamics Model III (E-AIM – http://www.aim.env.uea.ac.uk/aim/aim.php) using the atomizer solution composition and RH as inputs.[31] As there is no input for magnesium ion concentrations in E-AIM, we instead used 2 sodium ions for the calculations involving $MgSO_4$. The largest reaction probability for *trans*-β-IEPOX ($\gamma = 0.021$) was observed on $(NH_4)_2SO_4 + H_2SO_4$ aerosol under dry conditions. The γ values are similar to previous measurements for *trans*-β-IEPOX showing a general increase in γ with higher aerosol acidity, consistent with particle phase acid-catalyzed epoxide ring opening reactions.[5, 6, 32] Moreover, for the same aerosol type at higher RH, decreases in γ are likely attributable to dilution from additional aerosol water. To our knowledge these are the first reaction probability measurements of MAE. γ's for MAE were significantly lower than those for *trans*-β-IEPOX and likely responsible for the generally smaller observed SOA production.[16] Only at acidities closer to neutral ($[H^+] \sim 8x10^{-5}$) are the IEPOX and MAE γ's of similar magnitude with values on the order of $5x10^{-4}$.

2. Chamber Box Modeling of α_{SOA}.

As with the atomizer solutions, the RH used in the flow reactor studies were chosen to match the aforementioned chamber studies. In this way the γ's measured in the flow reactor experiments capture the appropriate γ that one would expect during the chamber experiments thus providing a reliable constraint for epoxide uptake rates in the chamber. To properly assess the overall SOA production, however, the α_{SOA} is needed in addition to γ. To this end a 0-D time-dependent box model was used to simulate the chamber experiments and estimate α_{SOA}. The model was initialized with γ's from the flow reactor measurements, the amount of epoxide injected into the chamber, the chamber-measured aerosol surface area and mass concentrations, the estimated chamber wall-loss rate from epoxide injections in the absence of seed particles (Figure 7.2), and the user-chosen α_{SOA}. Chemical rate equations for gas and aerosol-phase epoxide concentrations were integrated over the duration of the chamber experiment to determine time-dependent concentrations.

The only losses of gas-phase epoxide were to particle surface area and to the chamber walls, and the only source of aqueous-phase epoxide was the reaction of gas-phase epoxide on the particle surface area. The aqueous-phase epoxide formation rate was scaled by α_{SOA} in order to match the chamber-observed aerosol mass loadings. Aerosol surface area was held constant over the course of a model run despite that the SOA formation does contribute to the surface area. This is less of an issue for MAE given the modest SOA growth compared to *trans*-β-IEPOX. For the *trans*-β-IEPOX experiments the additional SOA resulted in at most a 40% increase in surface area. It is not clear how this additional surface area would affect the modeled SOA growth. Based on previous studies, the presence of aerosol phase semi-oxidized organics in the form of polyethylene glycol tended to inhibit *trans*-β-IEPOX uptake, thereby slowing the SOA growth.[5] Indeed we observed that the modeled SOA growth rate tended to be faster than that

observed in the chamber experiments. However, this effect could also be in part a result of the instantaneous mixing assumed by the box model.

As shown in Figure 3.2, α_{SOA} was adjusted in the model to bracket the observed chamber SOA mass growth and obtain an upper and lower estimate of α_{SOA}. These ranges are reported in Table 3.1. The value of α_{SOA} for *trans*-β-IEPOX and MAE varied for the different aerosol compositions from 0.03 – 0.16 and 0.05 – 0.22. The results show a slightly larger α_{SOA} calculated for the ammonium sulfate seed types compared to magnesium sulfate. In general, we would expect aerosol conditions that influence ɣ – high aerosol acidity, the concentration of general acids like bisulfate, and the concentrations of nucleophiles – to influence α_{SOA} similarly. While ɣ was largest for the acidified aerosols, α_{SOA} seems to be largely independent of acidity with the largest α_{SOA} for *trans*-β-IEPOX (α_{SOA} = 0.16) observed on the pure ammonium sulfate aerosol. Therefore it appears that even in the absence of a substantial concentration of acid catalyst the same ultimate mass yield can be achieved provided the timescale is sufficiently long. Model outputs for IEPOX showed good agreement with the chamber observations especially considering that the characteristic leveling off of the SOA mass growth was well represented in the model output (see Figure 3.2a). This was not the case for the MAE experiments as seen in Figure 3.2b where the model outputs fail to capture any leveling off in aerosol mass. As a result α_{SOA} estimates for MAE may be less robust compared to *trans*-β-IEPOX. An underestimation of the MAE ɣ – and therefore an overestimation of the α_{SOA} – could result in such differences. That said, MAE ɣ measurements were reproducible and the modest SOA growth coupled with the low-time resolution of the mass concentration data make modeling the MAE experiments inherently more difficult.

It should be stated that the molecular weight of the SOA is assumed to be the same as *trans*-β-IEPOX or MAE, depending on which epoxide was investigated, while the majority of SOA tracers have a molecular weight larger than the parent epoxide.[18, 20] As a result, the α_{SOA} reported here are likely biased high. As an upper limit example, IEPOX-derived organosulfate (216 g/mole) has been shown to be a primary component of isoprene-derived SOA with a molecular weight almost twice that of IEPOX (118 g/mole). If we assume all of the SOA mass is made up of these organosulfates our reported α_{SOA} would be biased high by about 50%.

As we state above, it is not clear how ɣ and the α_{SOA} are affected when a significant fraction of the aerosol surface area is represented by epoxide-derived SOA. This warrants further investigation as it could be quite relevant in regions like the southeastern United States during summer where isoprene SOA can account for a substantial portion of the $PM_{2.5}$ mass and therefore surface area. The results presented here which constrain all reactions that contribute to IEPOX- and MAE-derived SOA could be beneficial in regional and/or global models to help constrain predictions in total IEPOX- and MAE-derived SOA, especially since current models only constrain the model with a few known aqueous phase reaction rates.

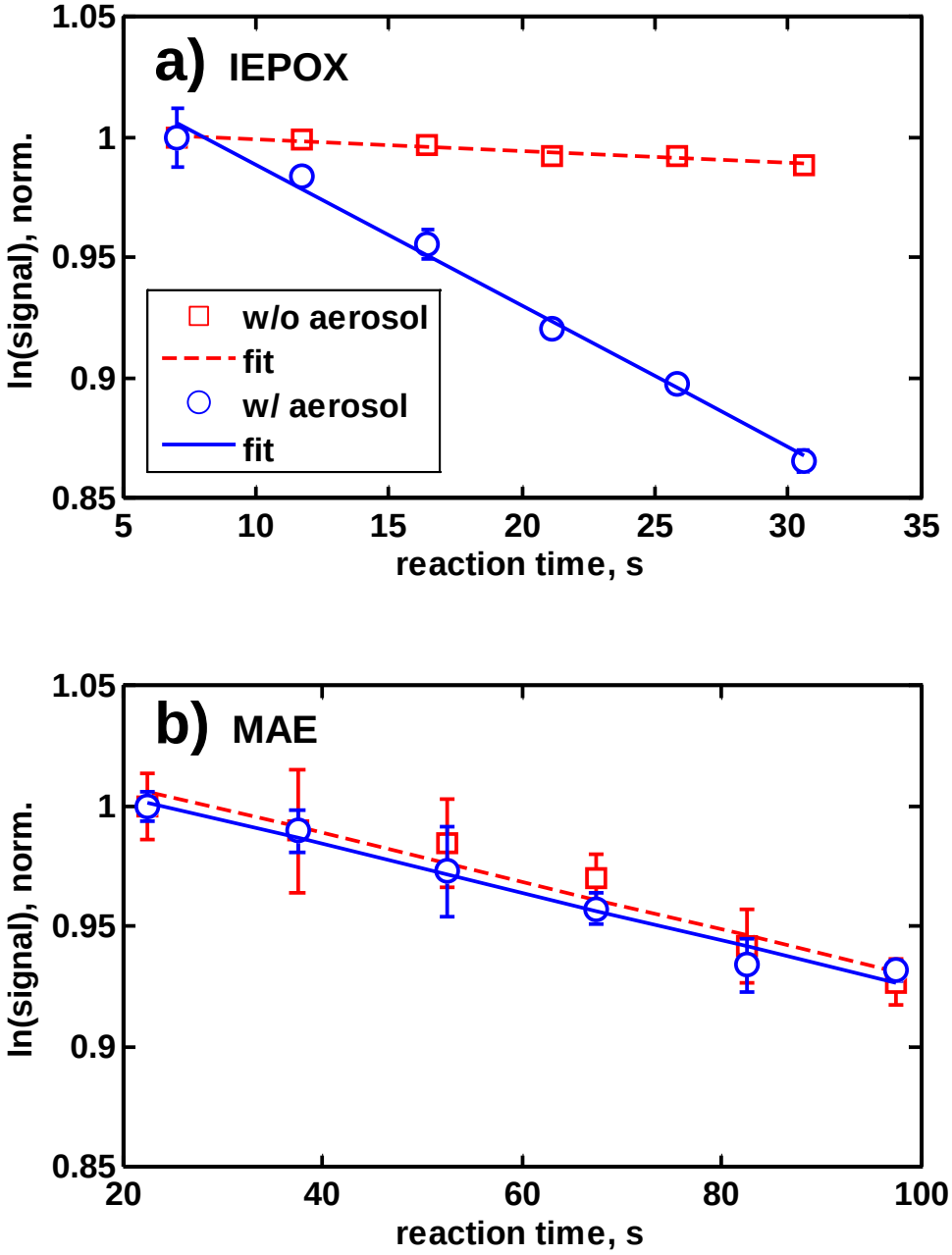

Figure 3.1. The average of the log of the epoxide signal versus reaction time and associated linear fit without aerosols (red squares, red dashed line is the fit) and with aerosols present in the flow reactor (blue circles, blue solid line is the fit) for (a) *trans*-β-IEPOX and (b) MAE on $(NH_4)_2SO_4$ + H_2SO_4 aerosol. Error bars represent the 2x the standard deviation of the averages. Values have been normalized to 1 for ease of comparison.

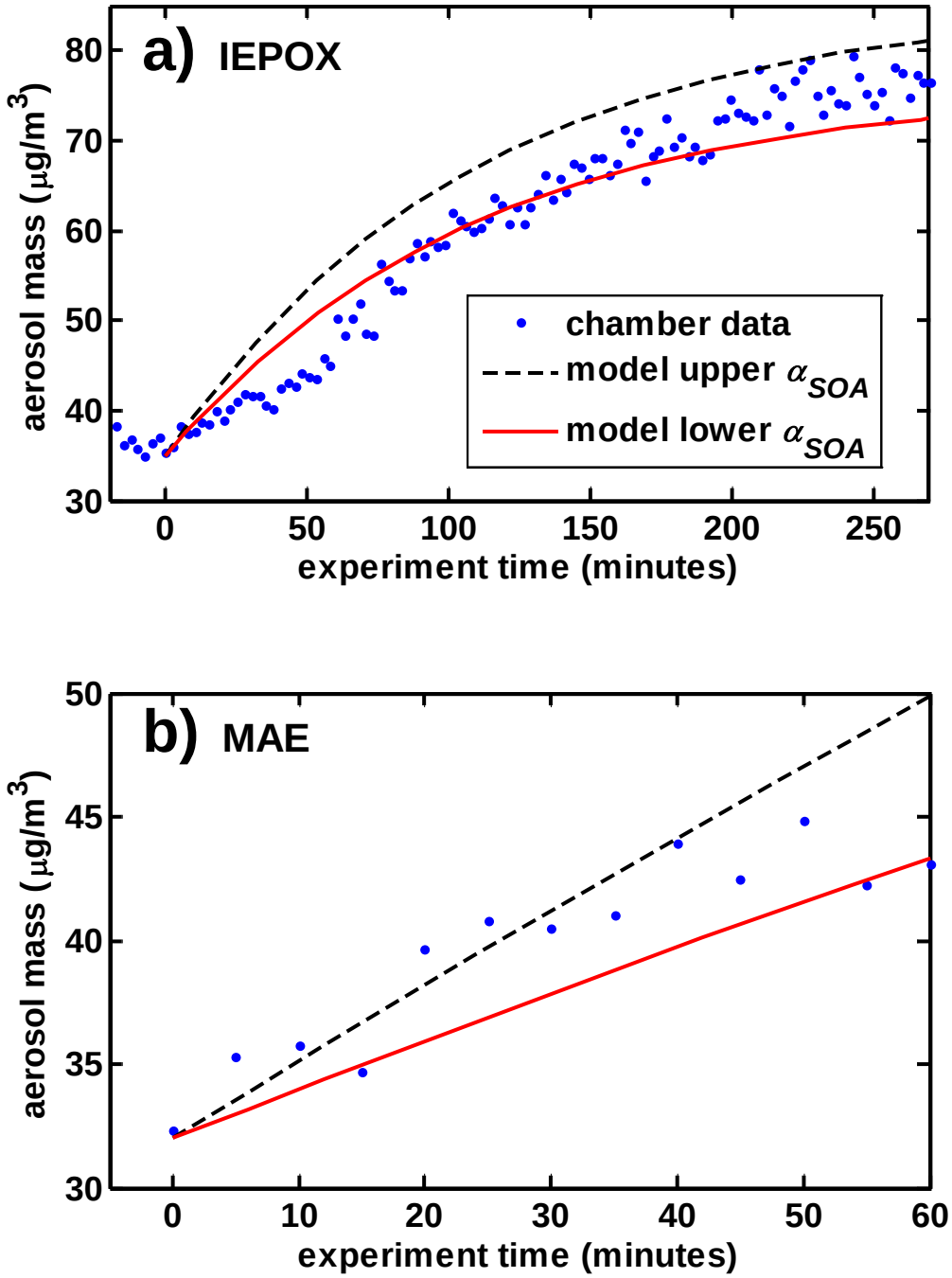

Figure 3.2. Chamber measured (blue dots) and modeled (black dashed line, red solid line) SOA mass loadings for (a) *trans*-β-IEPOX with $(NH_4)_2SO_4$ seed and (b) MAE with $(NH_4)_2SO_4$ + H_2SO_4 seed. The black dashed lines represent the predicted upper estimate of molar SOA yield (α_{SOA}), and the red solid lines represent the lower estimate (Table 3.1).

Table 3.1. Summary of Experiments and Results.

epoxide	aerosol	RH	aerosol $[H^+]$ (M)[a]	$\gamma \pm 1\sigma$	modeled α_{SOA} range
IEPOX	$(NH_4)_2SO_4$	0.50	7.74E-05	6.5e-4 ± 6.4e-4	0.13 - 0.16
IEPOX	$MgSO_4 + H_2SO_4$	0.08	0.04	0.011 ± 0.003	0.04 - 0.06
IEPOX	$MgSO_4 + H_2SO_4$	0.53	0.73	0.0094 ± 0.003	0.03 - 0.05
IEPOX	$(NH_4)_2SO_4 + H_2SO_4$	0.05	2.78	0.021 ± 0.001	0.09 - 0.11
IEPOX	$(NH_4)_2SO_4 + H_2SO_4$	0.59	2.01	0.019 ± 0.002	0.05 - 0.07
MAE	$MgSO_4 + H_2SO_4$	0.03	0.73	4.9e-4 ± 1e-4	0.05 - 0.11
MAE	$(NH_4)_2SO_4 + H_2SO_4$	0.03	2.78	5.2e-4 ± 1.1e-4	0.14 - 0.22

[a]Estimated from E-AIM model calculation of moles H^+ and total volume of aqueous phase. E-AIM RH input must be ≥0.1, so the same $[H^+]$ is estimated for like aerosol compositions despite differences in experimental RH.

D. REFERENCES

1. Guenther, A.; Karl, T.; Harley, P.; Wiedinmyer, C.; Palmer, P. I.; Geron, C., Estimates of global terrestrial isoprene emissions using MEGAN (Model of Emissions of Gases and Aerosols from Nature). *Atmos. Chem. Phys.* **2006,** *6* (11), 3181-3210.
2. Carlton, A. G.; Wiedinmyer, C.; Kroll, J. H., A review of Secondary Organic Aerosol (SOA) formation from isoprene. *Atmos. Chem. Phys.* **2009,** *9* (14), 4987-5005.
3. Hallquist, M.; Wenger, J. C.; Baltensperger, U.; Rudich, Y.; Simpson, D.; Claeys, M.; Dommen, J.; Donahue, N. M.; George, C.; Goldstein, A. H.; Hamilton, J. F.; Herrmann, H.; Hoffmann, T.; Iinuma, Y.; Jang, M.; Jenkin, M. E.; Jimenez, J. L.; Kiendler-Scharr, A.; Maenhaut, W.; McFiggans, G.; Mentel, T. F.; Monod, A.; Prévôt, A. S. H.; Seinfeld, J. H.; Surratt, J. D.; Szmigielski, R.; Wildt, J., The formation, properties and impact of secondary organic aerosol: current and emerging issues. *Atmos. Chem. Phys.* **2009,** *9* (14), 5155-5236.
4. Weber, R. J.; Sullivan, A. P.; Peltier, R. E.; Russell, A.; Yan, B.; Zheng, M.; de Gouw, J.; Warneke, C.; Brock, C.; Holloway, J. S.; Atlas, E. L.; Edgerton, E., A study of secondary organic aerosol formation in the anthropogenic-influenced southeastern United States. *Journal of Geophysical Research: Atmospheres* **2007,** *112* (D13), D13302.
5. Budisulistiorini, S. H.; Canagaratna, M. R.; Croteau, P. L.; Marth, W. J.; Baumann, K.; Edgerton, E. S.; Shaw, S. L.; Knipping, E. M.; Worsnop, D. R.; Jayne, J. T.; Gold, A.; Surratt, J. D., Real-Time Continuous Characterization of Secondary Organic Aerosol Derived from Isoprene Epoxydiols in Downtown Atlanta, Georgia, Using the Aerodyne Aerosol Chemical Speciation Monitor. *Environmental Science & Technology* **2013,** *47* (11), 5686-5694.
6. Lin, Y. H.; Knipping, E. M.; Edgerton, E. S.; Shaw, S. L.; Surratt, J. D., Investigating the influences of SO2 and NH3 levels on isoprene-derived secondary organic aerosol formation using conditional sampling approaches. *Atmos. Chem. Phys.* **2013,** *13* (16), 8457-8470.
7. Paulot, F.; Crounse, J. D.; Kjaergaard, H. G.; Kürten, A.; St. Clair, J. M.; Seinfeld, J. H.; Wennberg, P. O., Unexpected Epoxide Formation in the Gas-Phase Photooxidation of Isoprene. *Science* **2009,** *325* (5941), 730-733.
8. Lin, Y.-H.; Zhang, H.; Pye, H. O. T.; Zhang, Z.; Marth, W. J.; Park, S.; Arashiro, M.; Cui, T.; Budisulistiorini, S. H.; Sexton, K. G.; Vizuete, W.; Xie, Y.; Luecken, D. J.; Piletic, I. R.; Edney, E. O.; Bartolotti, L. J.; Gold, A.; Surratt, J. D., Epoxide as a precursor to secondary organic aerosol formation from isoprene photooxidation in the presence of nitrogen oxides. *Proceedings of the National Academy of Sciences* **2013,** *110* (17), 6718-6723.
9. Surratt, J. D.; Chan, A. W. H.; Eddingsaas, N. C.; Chan, M.; Loza, C. L.; Kwan, A. J.; Hersey, S. P.; Flagan, R. C.; Wennberg, P. O.; Seinfeld, J. H., Reactive intermediates revealed in secondary organic aerosol formation from isoprene. *Proceedings of the National Academy of Sciences* **2010,** *107* (15), 6640-6645.
10. Lin, Y.-H.; Zhang, Z.; Docherty, K. S.; Zhang, H.; Budisulistiorini, S. H.; Rubitschun, C. L.; Shaw, S. L.; Knipping, E. M.; Edgerton, E. S.; Kleindienst, T. E.; Gold, A.; Surratt, J. D., Isoprene Epoxydiols as Precursors to Secondary Organic Aerosol Formation: Acid-Catalyzed Reactive Uptake Studies with Authentic Compounds. *Environmental Science & Technology* **2011,** *46* (1), 250-258.

11. Gaston, C. J.; Riedel, T. P.; Zhang, Z.; Gold, A.; Surratt, J. D.; Thornton, J. A., Reactive Uptake of an Isoprene-Derived Epoxydiol to Submicron Aerosol Particles. *Environmental Science & Technology* **2014,** *48* (19), 11178-11186.
12. Pye, H. O. T.; Pinder, R. W.; Piletic, I. R.; Xie, Y.; Capps, S. L.; Lin, Y.-H.; Surratt, J. D.; Zhang, Z.; Gold, A.; Luecken, D. J.; Hutzell, W. T.; Jaoui, M.; Offenberg, J. H.; Kleindienst, T. E.; Lewandowski, M.; Edney, E. O., Epoxide Pathways Improve Model Predictions of Isoprene Markers and Reveal Key Role of Acidity in Aerosol Formation. *Environmental Science & Technology* **2013,** *47* (19), 11056-11064.
13. Alexander, B.; Hastings, M. G.; Allman, D. J.; Dachs, J.; Thornton, J. A.; Kunasek, S. A., Quantifying atmospheric nitrate formation pathways based on a global model of the oxygen isotopic composition (delta(17)O) of atmospheric nitrate. *Atmospheric Chemistry and Physics* **2009,** *9* (14), 5043-5056.
14. McNeill, V. F.; Woo, J. L.; Kim, D. D.; Schwier, A. N.; Wannell, N. J.; Sumner, A. J.; Barakat, J. M., Aqueous-Phase Secondary Organic Aerosol and Organosulfate Formation in Atmospheric Aerosols: A Modeling Study. *Environmental Science & Technology* **2012,** *46* (15), 8075-8081.
15. Bates, K. H.; Crounse, J. D.; St. Clair, J. M.; Bennett, N. B.; Nguyen, T. B.; Seinfeld, J. H.; Stoltz, B. M.; Wennberg, P. O., Gas Phase Production and Loss of Isoprene Epoxydiols. *The Journal of Physical Chemistry A* **2014,** *118* (7), 1237-1246.
16. Thornton, J. A.; Braban, C. F.; Abbatt, J. P. D., N_2O_5 hydrolysis on sub-micron organic aerosols: the effect of relative humidity, particle phase, and particle size. *Physical Chemistry Chemical Physics* **2003,** *5* (20), 4593-4603.
17. Thornton, J. A.; Abbatt, J. P. D., N_2O_5 reaction on submicron sea salt aerosol: Kinetics, products, and the effect of surface active organics. *Journal of Physical Chemistry A* **2005,** *109* (44), 10004-10012.
18. Zhang, Z.; Lin, Y. H.; Zhang, H.; Surratt, J. D.; Ball, L. M.; Gold, A., Technical Note: Synthesis of isoprene atmospheric oxidation products: isomeric epoxydiols and the rearrangement products cis- and trans-3-methyl-3,4-dihydroxytetrahydrofuran. *Atmos. Chem. Phys.* **2012,** *12* (18), 8529-8535.
19. Bertram, T. H.; Kimmel, J. R.; Crisp, T. A.; Ryder, O. S.; Yatavelli, R. L. N.; Thornton, J. A.; Cubison, M. J.; Gonin, M.; Worsnop, D. R., A field-deployable, chemical ionization time-of-flight mass spectrometer. *Atmospheric Measurement Techniques* **2011,** *4* (7), 1471-1479.
20. Kercher, J. P.; Riedel, T. P.; Thornton, J. A., Chlorine activation by N_2O_5: simultaneous, in situ detection of $ClNO_2$ and N_2O_5 by chemical ionization mass spectrometry. *Atmospheric Measurement Techniques* **2009,** *2* (1), 193-204.
21. Brown, R. L., Tubular Flow Reactors With First-Order Kinetics. *Journal of Research of the National Bureau of Standards* **1978,** *83* (1), 1-8.
22. Clegg, S. L.; Brimblecombe, P.; Wexler, A. S., Thermodynamic Model of the System H^+−NH_4^+−Na^+−SO_4^{2-}−NO_3^-−Cl^-−H_2O at 298.15 K. *The Journal of Physical Chemistry A* **1998,** *102* (12), 2155-2171.
23. Nguyen, T. B.; Coggon, M. M.; Bates, K. H.; Zhang, X.; Schwantes, R. H.; Schilling, K. A.; Loza, C. L.; Flagan, R. C.; Wennberg, P. O.; Seinfeld, J. H., Organic aerosol formation from the reactive uptake of isoprene epoxydiols (IEPOX) onto non-acidified inorganic seeds. *Atmos. Chem. Phys.* **2014,** *14* (7), 3497-3510.

24. Eddingsaas, N. C.; VanderVelde, D. G.; Wennberg, P. O., Kinetics and Products of the Acid-Catalyzed Ring-Opening of Atmospherically Relevant Butyl Epoxy Alcohols. *The Journal of Physical Chemistry A* **2010,** *114* (31), 8106-8113.

4. Constraining Condensed-Phase Formation Kinetics of Secondary Organic Aerosol Components from Isoprene Epoxydiols

A. Introduction

The gas-phase photooxidation of isoprene (2-methyl-1,3-butadiene), the largest biogenic volatile organic compound (VOC) emitted worldwide [33], forms isomeric isoprene epoxydiols (IEPOX) [17]. Subsequent acid-catalyzed multiphase chemistry of IEPOX is a significant source of secondary organic aerosol (SOA) mass [19, 34]. In recent field studies, upwards of 50% of the summertime aerosol mass loadings in the southeastern United States has been attributed to SOA resulting from IEPOX heterogeneous reactions [15, 16, 35]. Similar IEPOX-derived SOA influences are expected in areas with large isoprene emissions, such as tropical forests primarily composed of broad-leaf vegetation. As such a significant SOA precursor, IEPOX has implications regarding potential climate forcing due to the scattering of incoming radiation as well human health effects (REF Mandy's paper when published) [36, 37].

Once produced from isoprene photooxidation, gas-phase IEPOX can partition to atmospheric aerosol surface area where it can react with aerosol-phase constituents, such as water, nitrate, or other organics, to form a variety of low-volatility organic compounds that remain in the aerosol and contribute to the total aerosol mass. These low-volatility species are often referred to as SOA "tracers," as a number can be detected through offline chemical measurements that directly illustrate that IEPOX was the precursor. The efficiency of gas-phase IEPOX removal by aerosol surface area is largely thought to be a function of aerosol acidity and the concentration of nucleophiles present that can react with accommodated IEPOX [5, 32, 38-40]. Once accommodated to the aerosol, IEPOX undergoes an acid-catalyzed opening of the epoxide ring followed by nucleophilic addition to produce various tracer species [6]. Products of these reactions include the 2-methyltetrols (2-methylthreitol and 2-methylerythritol) for water addition reactions, and the IEPOX-derived organosulfate (IEPOX-OS) for sulfate addition as shown in Reactions (R1) – (R2) [41, 42].

(R1) $IEPOX_{(aq)} + H^+ + H_2O \rightarrow 2\text{-}methytetrols + H^+$

(R2) $IEPOX_{(aq)} + H^+ + SO_4^{2-} \rightarrow IEPOX\text{-OS} + H^+$

where *aq* is aqueous.

These products have been observed in field samples, and those resulting from nitrate addition, while observed less often, are also thought to be important in certain cases [34, 43]. Additional condensed-phase reactions form IEPOX-derived dimer species (2-methyltetrol dimers, OS dimers), rearrangement products (isomeric C_5-alkene triols and 3-methyltetrahydrofuran-3,4-diols (3-MeTHF-3,4-diols)), and higher order oligomers which have also been identified in field and chamber studies [16, 34, 44]. The formation

of certain IEPOX-derived oligomers has also been linked to brown carbon formation, and therefore, potentially having significant radiative forcing [44]. General acids, such as bisulfate, can also serve as ring-opening catalysts, though these reaction rates tend to be significantly slower for most aerosol conditions [6].

To date, only the formation of IEPOX-derived 2-methyltetrols and organosulfates have been characterized through bulk kinetic measurements [6]. While these two tracers are thought to be responsible for a sizeable fraction of IEPOX-derived SOA [16, 18], the remaining tracer formation reactions have yet to be examined. Accurate estimates would be beneficial especially for modeling purposes (e.g., see [23], [21], and [45]). Here we present an approach that combines chamber experiments, quantification of SOA tracers from filter samples using synthetic standards, and modeling to estimate the formation reaction rate constants of a number of IEPOX-derived SOA tracers that have been identified and quantified through offline measurements but whose formation rates have yet to be constrained by bulk solution measurements. This is done for a single seed aerosol system – acidified ammonium sulfate at low relative humidity (RH) –, but the obtained rate coefficients should, in theory, be independent of the seed aerosol used.

B. Methods

1. Chamber experiments

IEPOX-derived SOA growth experiments were conducted in an indoor 10-m^3 Teflon smog chamber under dark conditions that has been used in a number of recent studies at the University of North Carolina – Chapel Hill (UNC) [40, 44]. Acidic ammonium sulfate seed aerosol was injected into the dry (RH < 5%) chamber using a custom-built atomizer with an atomizing solution of 0.06 M $(NH_4)_2SO_4$ + H_2SO_4 until the desired total aerosol mass concentration was achieved. The custom-built pneumatic atomizer, which uses the energy from compressed air to break up a liquid stream, was designed and manufactured within the UNC Design Shop. Specifically, a mason jar is used that is attached to custom made Teflon and stainless steel fittings where high-purity compressed gas is passed through to generate aerosol. Concentration of salt solutions (e.g., ammonium sulfate or ammonium sulfate spiked with sulfuric acid) are adjusted to change the mode of the polydisperse aerosol size distribution generated; higher concentration of salt solution yields higher mode of aerosol generated from this atomizer. We generally target a mode of 50-80 nm at the beginning of each experiment. Further, the atomizer is cleaned between experiments by ultra sonication in Milli-Q water (18 mega Ohm).

After seed injection, the chamber was left static for at least 30 minutes to ensure that the seed aerosol concentration was stable and uniformly mixed throughout the chamber. IEPOX was then injected into the chamber for 2 hours by passing ~4 standard liters per minute (slpm) of $N_{2(g)}$ through a 60 °C heated glass manifold containing 50 – 300 μL of a 100 mg mL^{-1} mixture of the *trans-β*-IEPOX isomer, which is the predominant IEPOX isomer [24], in ethyl acetate. Synthesis methods for authentic *trans-β*-IEPOX are

described in the appendix [27]. The majority of the SOA mass growth took place within the first hour of the injection period, and by the end of the 2-hour period, significant SOA growth had largely stopped.

Chamber aerosol number distributions, which were subsequently converted to total aerosol surface area and volume concentrations, were measured by a scanning electrical mobility system (SEMS v5.0, Brechtel Manufacturing Inc. – BMI) containing a differential mobility analyzer (DMA, BMI) coupled to a mixing condensation particle counter (MCPC Model 1710, BMI). Total volume concentrations of seed aerosol were converted to total mass concentrations assuming a density of 1.6 g mL^{-1}, similar to that estimated by aerosol thermodynamic model outputs which we describe in more detail below, and SOA total volume concentrations were converted to total mass concentrations assuming a density of 1.25 g mL^{-1} [46]. The chamber RH and temperature were monitored with a commercial RH/temperature probe (OM-62, Omega Engineering Inc.). Gas-phase components, including *trans*-β-IEPOX, were measured with an iodide-adduct high-resolution time-of-flight chemical ionization mass spectrometer (HR-ToF-CIMS, Aerodyne Research, Inc.) described elsewhere [28, 47]. For this project we quality assured our data from the HR-ToF-CIMS instrument by comparing known standards quantified by independent instruments. For IEPOX, this was completed by injecting known amounts of the authentic *trans*-β-IEPOX standard into the HR-ToF-CIMS under a constant sampling flow of 2.1 slpm. Chamber levels of IEPOX are quantified by monitoring the mass-to-charge ratio (*m/z*) 244.9 that corresponds to the IEPOX-iodide ion cluster ($I^-\cdot C_5H_{10}O_3$) or any other gas-phase species isobaric with I^-·IEPOX. For the purposes of these experiments, we assume the entire *m/z* 244.9 signal is due to IEPOX. The HR-ToF-CIMS was always calibrated before each experimental run with the appropriate authentic standards for the target analytes. Blank experiments were also conducted to insure that no compounds were present in the chamber. No isoprene SOA constituents or IEPOX were found in the blank experimental runs.

2. SOA tracer quantification

At the conclusion of the IEPOX injection period, a filter sample was collected in order to analyze the composition of the chamber-generated SOA. Aerosols were collected onto 46.2 mm Teflon filters (Part No.: SF17471, Tisch Scientific) in a stainless steel filter holder for 2 hours at ~15 slpm with a carbon strip denuder (Sunset Labs) upstream of the filter holder. After collection, the filters were stored in 20 mL scintillation vials within a -20 °C freezer until extraction for subsequent analysis.

The IEPOX-derived SOA components were extracted from filters in high-purity methanol prior to chemical analyses by a gas chromatograph/mass spectrometer equipped with electron ionization (GC/EI-MS – 5890 Series II GC and 5971A MS, Hewlett-Packard) and an ultra performance liquid chromatograph/high-resolution quadrupole time-of-flight mass spectrometer equipped with electrospray ionization (UPLC/ESI-HR-QTOFMS – 6500 Series, Agilent) [19, 34]. 2-methyltetrols, C_5-alkene triols, 3-MeTHF-

3,4-diols, and the IEPOX-derived dimer, were quantified using GC/EI-MS with prior trimethylsilylation.

For this project we quality assured our data from the UPLC/ESI-HR-QTOFMS and GC/EI-MS instruments by comparing known standards quantified by independent instruments. The GC/EI-MS calibrations for these species were performed with authentic 2-methyltetrol and 3-MeTHF-3,4-diol standards [27]. The triols and dimer were assumed to have the same instrumental sensitivity as the 2-methyltetrol standard. A known fraction of the filter extracts were reconstituted in a 50:50 (v/v) methanol:water mixture from which the IEPOX-OS and IEPOX-derived dimer organosulfate (IEPOX-dimerOS) were quantified using UPLC/ESI-HR-QTOFMS operated in the negative ion mode. An authentic IEPOX-OS standard was used for calibration, and IEPOX-dimerOS was assumed to have the same calibration factor as the IEPOX-OS standard. Both instruments were always calibrated before each experimental run with the appropriate authentic standards for the target analytes. Blank experiments were also conducted to insure that no compounds were present in the chamber. No isoprene SOA constituents or IEPOX were found in the blank experimental runs. Surrogate spikes are performed to quantify the recovery without introducing target analytes into the process. Triplicate samples are run at standard intervals to measure precision and reproducibility of the results. Field and laboratory blanks provide assurance that positive results are not from sources other than the one being tested. Field blanks ensure that the sampling device has been effectively cleaned. Laboratory blanks monitor lab reagents for analyte contamination.

Filter sample security and accountability are assured during each stage of sample processing. Each sample is assigned a unique laboratory sample number (or date of collection) so that it can be identified and traced throughout the laboratory. Laboratory documentation assures analysis results traceable to valid calibrations, optimal instrument conditions, and appropriate reagents.

Acceptance criteria are established by statistical evaluation of data using the mean +/- 3 standard deviations to establish control limits. In the event of a quality control failure, the probable cause is determined, and samples may be repeated when it is determined that the cause of the failure no longer exists. More quality assurance measures are done after sample processing is completed. Blank, spike, and calibration data is summarized into tables and control charts for evaluation. The data is used to calculate control limits, and also to evaluate shifts and trends in the data.

3. Model setup and evaluation

We utilize a zero-dimensional (0-D) time-dependent chemical box model with explicit aqueous-phase tracer formation chemistry to investigate the reaction kinetics involved in the chamber SOA production. The model is initialized with the amount of *trans*-β-IEPOX added to the injection manifold as well as the measured seed aerosol total surface area and mass concentration. Estimates of the aqueous-phase molar concentrations of the inorganic seed aerosol species ($[H^+]$, $[H_2O]$, $[HSO_4^-]$, $[SO_4^{2-}]$) and the total volume of the

aqueous phase are obtained from the Extended AIM Aerosol Thermodynamics Model III (AIM, http://www.aim.env.uea.ac.uk/aim/aim.php) [7, 31]. The composition of the atomizer solution was used as the AIM inputs with a RH of 10% as AIM does not allow for RH inputs lower than 10%. As is typical with aerosol thermodynamic model calculations, the aerosol components were treated as a metastable solution thereby suppressing the formation of solid-phase species [48]. While we acknowledge that it is preferred to use some gas-phase measurements to constrain aerosol thermodynamic models, such measurements (e.g., gas-phase ammonia) were unavailable for these experiments and thus could not be used. Similarly, at low RH, models tend to have more difficulties representing the actual state of the aerosols. As a result, we recognize that our estimates presented herein are likely limited by the ability of so-called "reverse mode" thermodynamic aerosol model calculations to appropriately represent the aerosols in the chamber.

A constant IEPOX-aerosol reaction probability (γ) of 0.021 was assumed over the course of a modeled experiment, which is consistent with those measured on similar seed aerosol systems [5, 40]. The resulting pseudo-first order heterogeneous uptake rate coefficient (k_{het}) of IEPOX to the aerosol phase was then calculated by Eq. (4.1),

$$k_{het} = \frac{\gamma S_a \omega}{4} \quad \text{(Eq. 4.1)}$$

where S_a is the total seed aerosol surface area concentration and ω is the mean molecular speed of gas-phase IEPOX. Similar to [40], the aerosol surface area concentration is held constant over the course of a model run. In doing so, the additional surface area resulting from IEPOX-dervied SOA does not enhance k_{het}, but it also does not decrease k_{het} or, in other words, inhibit IEPOX uptake as the presence of certain organics have been shown to do [5]. Once IEPOX has partitioned to the particle phase – represented here as $IEPOX_{(aq)}$ – it is allowed to react with the inorganic aerosol constituents to form the SOA tracer species outlined above. In addition to Reactions (R1) and (R2) described above, the model incorporates acid-catalyzed reactions to form C_5-alkene triols, 3-MeTHF-3,4-diols, IEPOX-dimer, and IEPOX-dimerOS – Reactions (R3) – (R6) below. The model also tracks the formation of "other SOA" which we define as the difference between the chamber-measured SOA mass and the sum of the quantified tracer mass loadings. The species that make up the "other SOA" are representative of tracers that have yet to be quantified (e.g., higher order oligomers) and/or identified through offline measurement techniques. Similar to the other tracer formation reactions, the formation of the "other SOA" within the model is likely an acid-catalyzed process. We tentatively assume that the species making up the "other SOA" are made up of oligomeric type compounds and that the formation of these higher order oligomers results from the addition of existing organic nucleophiles like IEPOX-OS, Reaction (R7). Within the model, all of the "other SOA" is assumed to have an average molecular weight of 334 g mole^{-1}, the same as that of IEPOX-dimerOS.

$$IEPOX_{(aq)} + H^+ \rightarrow C_5\text{-alkene triols} + H^+ \quad \text{(R3)}$$

$$IEPOX_{(aq)} + H^+ \rightarrow \text{3-MeTHF-3,4-diols} + H^+$$
(R4)

$$IEPOX_{(aq)} + H^+ + \text{2-methyltetrols} \rightarrow \text{IEPOX-dimer} + H^+$$
(R5)

$$IEPOX_{(aq)} + H^+ + IEPOX\text{-OS} \rightarrow \text{IEPOX-dimerOS} + H^+$$
(R6)

$$IEPOX_{(aq)} + H^+ + IEPOX\text{-OS} \rightarrow \text{other SOA} + H^+$$
(R7)

where *aq* is aqueous.

The coupled differential equations corresponding to the production and/or loss of $IEPOX_{(g)}$, $IEPOX_{(aq)}$, 2-methyltetrols, IEPOX-OS, C_5-alkene triols, 3-MeTHF-3,4-diols, IEPOX-dimer, IEPOX-dimerOS, other SOA, HSO_4^-, and SO_4^{2-} are integrated over the entire IEPOX injection duration (2 hours) or until the observed chamber SOA mass concentration had reached a maximum. We assume that SO_4^{2-} and HSO_4^- remain in the initial equilibrium ratio such that when SO_4^{2-} is consumed to form IEPOX-OS, HSO_4^- is converted to SO_4^{2-} to maintain the same ratio. Additionally, we apply a general first-order loss to $IEPOX_{(aq)}$ – Reaction (R8) – that forms volatile products which do not contribute to the overall SOA mass.

$$IEPOX_{(aq)} \rightarrow \text{volatile products}$$
(R8)

This reaction serves to lower the molar SOA yield (ϕ_{SOA}) below unity to a point where the modeled SOA mass formation closely matches that of the experimental data. A first-order wall-loss is also applied to gas-phase IEPOX ($k = 9.4 \times 10^{-5}$ s^{-1}) and to all aerosol-phase species ($k = 1 \times 10^{-5}$ s^{-1}), similar to those estimated for this chamber in a previous study [40]. To appropriately capture the IEPOX injection into the chamber, the model represents the amount of IEPOX remaining in the injection manifold as an exponential decay. The decay constant, which varied between 1×10^{-3} s^{-1} – 2×10^{-3} s^{-1} for the different model simulations, was then used as a fitting parameter to better match the timescale of observed SOA growth. However, over the 2-hour duration of the experiment, this parameter had a negligible effect on the final model-predicted SOA growth.

We systemically vary the rate constants (k) for Reactions (R1) – (R8) within the model until the model output closely matches the offline tracer measurements. Once the model is given an initial estimation for each k, it is then run in a continuous loop varying k_{R1} – k_{R8} until the sum of the square differences between the filter-based tracer measurements and the model output is minimized. The only constraint used during minimization is that all $k > 0$. Implicitly, this approach assumes that the filter-based tracer measurements are robust and a correct representation of the actual IEPOX-derived SOA speciation and mass loading and that the filter collection and extraction efficiency is 100%.

C. Results and discussion

1. Model output and comparison to chamber data

Five total chamber experiments were performed for the $(NH_4)_2SO_4$ + H_2SO_4 seed aerosol system: two with 30 mg of IEPOX injected and ~120 μg m^{-3} seed aerosol, one with 15 mg of IEPOX injected and ~75 μg m^{-3} seed aerosol, and two with 5 mg IEPOX injection and ~60 μg m^{-3} seed aerosol. Initial chamber conditions for all experiments including seed aerosol surface area and mass loading as well as the amount of IEPOX placed in the injection manifold are provided in Table 4.1. Figure 4.1 shows aerosol mass data for one experiment (Exp. No. 1). The initial seed aerosol mass loading starts near 113 μg m^{-3}, and at experiment time (t) = 0 minutes the IEPOX injection is started. SOA mass growth is most rapid during the first 30 minutes after the start of IEPOX injection and begins to slow thereafter until reaching a maximum of ~275 μg m^{-3} total aerosol mass at t ≈ 90 minutes. The timescale of SOA growth for the other experiments was largely consistent with that of Figure 4.1. The corresponding model simulation for Exp. No. 1 is also shown in Figure 4.1. The model output was able to capture the SOA growth well – both the rate and the maximum mass loading – for all experimental cases. It should be emphasized though that model-measurement agreement for this particular study should not be interpreted as an indicator of model proficiency given that model parameters are adjusted to maximize this agreement – a point we revisit below.

As described above, the modeled SOA concentration is a sum of the 2-methyltetrols, IEPOX-OS, C_5-alkene triols, 3-MeTHF-3,4-diols, IEPOX-dimer, IEPOX-dimerOS, and other SOA. Figure 4.2 shows the modeled time evolution of SOA composition contributing to total SOA for Exp. No. 1 alongside the corresponding filter-based tracer measurements. These results as well as those from the other experiments are given in Table 4.2. The modeled SOA tracers agree well with the filter-based measurements with a percent difference <4% for all tracer species. Again this is unsurprising considering that $k_{R1} - k_{R8}$ are varied to ensure a small difference.

The model also predicts significant titration (~34%) of total aqueous inorganic sulfate species ($[SO_4^{2-}] + [HSO_4^-]$) over the course of an experiment. These titrations match well those shown in [41] for a low-NO_X isoprene oxidation experiment with acidified ammonium sulfate seed aerosol.

2. Model-predicted tracer formation kinetics

The resulting model-predicted tracer formation rate constants for Reactions (R1) – (R7) are given in Table 4.3. Equation for error is shown in Eq. 4-2. These are averaged over all experiments and the listed errors correspond to one standard deviation. As described

above these errors are in comparison with filter-based tracer measurements taken during the experiment. Implicitly, this approach assumes that the filter-based tracer measurements are correct. As opposed to comparing model-measurement agreement as an evaluation of model skill, a better choice for this study is the degree to which the extracted rate constants agree across the 5 model runs. Excluding the 3-MeTHF-3,4-diols rate constants, the error for all of the tracer formation rate constants were smaller than the mean with the largest errors representing ~90% of the mean values. Expectedly, the 3-MeTHF-3,4-diols formation rate constant shows the largest error, which is likely a result of the high volatility of the 3-MeTHF-3,4-diols compared to the other measured tracers. It is therefore a challenge to prevent losses during the drying portions of the filter extraction process.

Eq. 4-2 Error = $(k_{simulation} - k_{filter})$

Where $k_{simulation}$ is the model based reaction rate constant and k_{filter} is the filter based reaction rate.

While there are certainly nonidealities that exist for the aerosols that are not present in bulk solution kinetic measurements, a useful check is the degree to which the rate constants obtained in this study compare to those from existing bulk-solution kinetic measurements for 2-methyltetrols and IEPOX-OS formation [6]. For 2-methyltetrol formation, [6] determined the pseudo second-order formation constant for bulk solutions with water in excess, and [21] assumed a water concentration of 55 M in order to convert to a third-order rate constant with an explicit water dependence. The resulting rate constants from these studies are 9×10^{-4} M^{-2} s and 2×10^{-4} M^{-2} s for 2-methyltetrol (Reaction (R1)) and IEPOX-OS (Reaction (R2)) formation, respectively. These are of the same order as those predicted from the model output of $2.0 \pm 1.1 \times 10^{-4}$ M^{-2} s and $3.1 \pm 0.7 \times 10^{-4}$ M^{-2} s for 2-methyltetrols and IEPOX-OS, respectively, giving us confidence that the model does a suitable job in representing the kinetics of this multiphase process. Especially considering the low RH, non-ideal conditions present in the highly concentrated chamber aerosols may, in part, be responsible for these differences.

As mentioned earlier, we do not explicitly include epoxide ring-opening reactions by general acids (i.e., bisulfate). We expect such a contribution to be negligible as the branching ratio between bisulfate and H^+-catalyzed reaction channels likely heavily favors the H^+ channel. For example, in Exp. No. 1, ~98% of the epoxide ring-opening is predicted to proceed through the H^+-catalyzed channel compared to that of bisulfate. Given the estimates of the tracer formation rate constants, the calculated k_{het}, and the model output, the molar SOA yield (ϕ_{SOA}) can be estimated as the ratio of the sum of the tracer production rates over the $IEPOX_{(g)}$ heterogeneous loss rate [40]. Averaged over the 5 experiments $\phi_{SOA} = 0.078 \pm 0.024$ (1σ) with the largest ϕ_{SOA} shown for the 5 mg IEPOX injections and the smallest ϕ_{SOA} shown for the 30 mg injections. This ϕ_{SOA} is similar to that predicted from an independent modeling approach which estimated the ϕ_{SOA} for this aerosol system at 0.1 – 0.12 [40]. These results indicate that the molar yield of SOA from IEPOX heterogeneous reactions is likely to be significantly <1 for the majority of

atmospheric conditions where aerosols likely contain more water while being less acidic than the studies presented here.

3. Additional investigations

The $IEPOX_{(g)}$ time series obtained from the CIMS measurements for Exp. No. 1 is shown in Figure 4.3. During the beginning of the experiment, no appreciable IEPOX is observed, likely due to the rapid uptake and SOA growth. After t ≈ 20 minutes IEPOX levels start to accumulate and continue to build up until the end of the experiment. Similar behavior was shown in all of the chamber experiments. We tentatively attribute this behavior to IEPOX partitioning off of the chamber walls as the chamber-measured mixing ratio matches well with the amount of IEPOX expected to be lost to wall reactions by the model (see Figure 4.3). This indicates that IEPOX losses to the Teflon chamber walls can, to some extent, be at least partially reversible. The amount of IEPOX released from the chamber walls is expected to produce a negligible effect on the observed SOA in these experiments. For example, in Exp. No. 1, 25 ppbv of IEPOX should produce <10 μg m^{-3} of SOA mass growth, which would be within the scatter observed in the chamber aerosol mass measurements. However, it is worth noting that some of the IEPOX signal could be represented by other species isobaric with IEPOX. Indeed the 3-MeTHF-3,4-diols, which have the same molecular weight as IEPOX and are detectable by iodide-CIMS and presumably have a comparatively high vapor pressure, could be one such potential interference.

Further examination of the CIMS data shows a strong signal at *m/z* 262.9 that increased steadily over the course of an experiment (see Figure 4.4). High-resolution fitting of this peak within the mass spectra identifies this ion as $I^-\cdot C_5H_{12}O_4$ with low error (<15 ppm). $C_5H_{12}O_4$ is the same composition as the 2-methyltetrols that we quantify in the particle phase from the filter measurements, so initially it appeared as though a sizeable fraction of the 2-methyltetrol was also in the gas phase, depending on the sensitivity of the CIMS to 2-methyltetrols. However, CIMS calibration attempts with the authentic 2-methytetrols standard showed little to no signal at *m/z* 262.9. This could be due to a low vapor pressure or the inability to detect 2-methyltetrols under the current instrumental settings. Even upon exposure of the pure standard to the CIMS inlet, no significant signal was observed. As such, it appears that the measured gas-phase compound at *m/z* 262.9 is not the 2-methyltetrols and that 2-methyltetrols do not strongly partition to the gas-phase after formation in the aerosols. That said, this signal shares a similar time profile and correlates well (R^2 = 0.986) with the IEPOX signal at *m/z* 244.9 shown in Figure 4.3. Therefore, we cannot rule out that this could also be a product partitioning off of the chamber walls. Effects such as this and the partitioning of IEPOX to and from the chamber walls are unsurprising considering that the chamber walls represent a considerable surface area compared to the aerosols (~1000:1, $S_{a\text{-}walls}$:$S_{a\text{-}aerosol}$) and could certainly act as a reactive substrate [49].

Chamber experiments similar to those described above were also performed at elevated RH (~50%). However, despite sampling through the carbon strip denuder which should

remove the majority of residual gas-phase IEPOX from the sampling stream, large positive artifacts for the filter-based tracer measurements were observed such that we could not reconcile these filter-based mass loadings with the aerosol mass loadings observed in the chamber as measured by the SEMS-MCPC. The sum of the filter-based tracer mass loadings was significantly greater (1.2 – 2.3x) than those reported by the SEMS-MCPC, and therefore, these experiments were essentially unusable for the kinetic investigations presented here. Presumably, without the carbon strip denuder these positive artifacts would be even more enhanced. We presume that the filter membrane provides a surface for IEPOX and water uptake and tracer formation. In choosing to mention these results here, we hope to illustrate the potential for positive artifacts resulting from filter collection in both laboratory and field measurements at moderate to high RH.

D. Atmospheric implications and conclusions

By applying the estimated formation rate constants to an atmospherically relevant initial model condition, we can use the model to obtain approximate SOA mass loading and speciation of what might be partly representative of conditions in the atmosphere. For example, in order to represent a summer daytime mixture of an urban air mass containing acidified sulfate aerosols with a rural air mass containing appreciable amounts of IEPOX, we assume a gas-phase IEPOX mixing ratio of ~500 pptv with 250 μm^2 cm^{-3} of ammonium bisulfate aerosol surface area. Such surface area concentrations would correspond to an aerosol mass loading of roughly ~10 μg m^{-3}. Figure 4.5 shows the resulting model output for 3 hours of processing time. For these model conditions, 0.39 μg m^{-3} of total SOA is formed with the bulk (74%) being represented by 2-methyltetrols and minor amounts represented by IEPOX-OS (15%), C_5-alkene triols (9%), and 3-MeTHF-3,4-diols (2%). The remaining tracers – IEPOX-dimer, IEPOX-dimerOS, and other SOA – were predicted to form in small amounts (<2 ng m^{-3}), which are supported by the small loadings of these species in field samples from the southeastern United States [34, 35]. Notably, the model predictions for this example atmospheric situation yields an average loading that is similar to recent measurements at the Look Rock, TN, ground site during the Southern Oxidant and Aerosol Study (SOAS) [35]. Additionally, for this simulation, there was no discernable titration of total aqueous inorganic sulfate indicating that such titrations are unlikely to occur in atmospheric aerosols.

In summary, the approach outlined here to determine aqueous-phase IEPOX-SOA tracer formation rate constants is intended to be a good first approach at putting kinetic constraints on the formation of species that have been quantified though laboratory and/or field measurements but lack directly measured experimental rate constraints. While directly measured bulk-phase rate constant estimates are likely preferable to the modeling approaches outlined here, such measurements can often pose a challenge to measure in the condensed phase when authentic standards are unavailable or when surrogates may only be partially representative of the true compound. Furthermore, this method is such that it could be extended to other SOA production systems known to have atmospheric importance. Granted, special care must be taken to ensure that potential reactions and/or

partitioning resulting from reactor surfaces are well characterized or at least taken into account.

These investigations provide tracer branching ratios for SOA resulting from IEPOX uptake that is a necessary step to appropriately capture isoprene-derived SOA production in regional models that often guide policy decisions. It remains crucially important that SOA formation mechanisms are investigated in controlled experiments and then extended to models to ensure that the collective understanding of the mechanisms can accurately represent the observations before they are scaled up to large 2-D model domains.

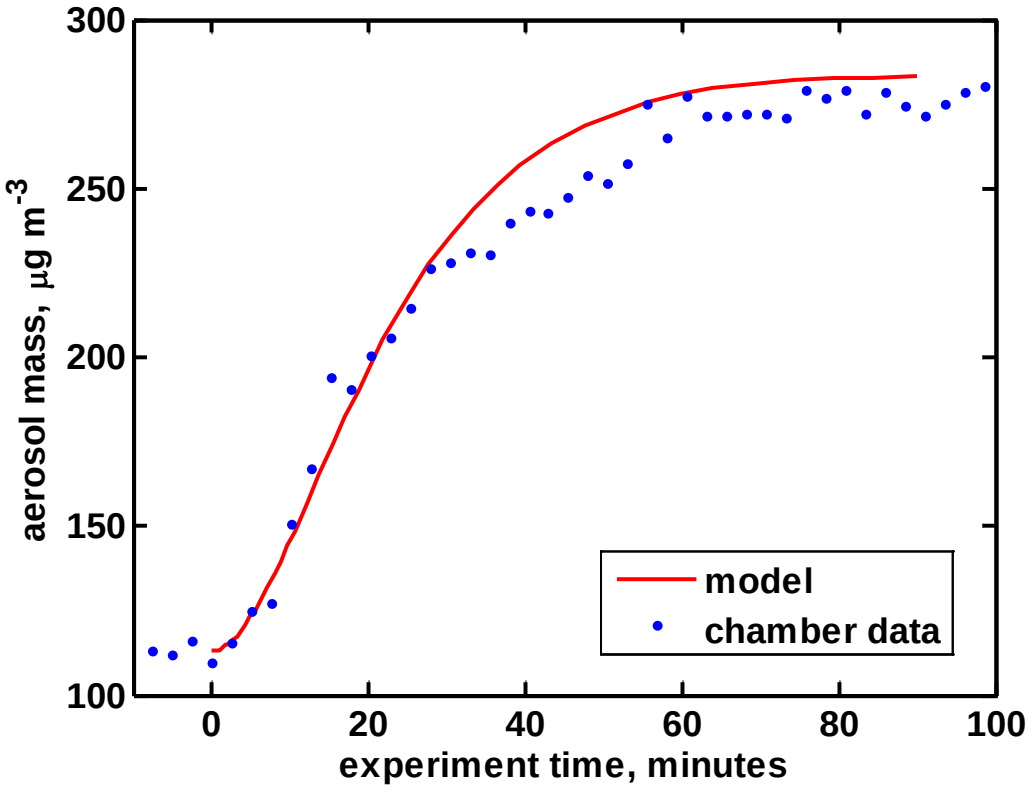

Figure 4.1. Aerosol mass loadings from IEPOX-SOA Exp. No. 1 and corresponding model output. IEPOX injection starts at experiment time = 0.

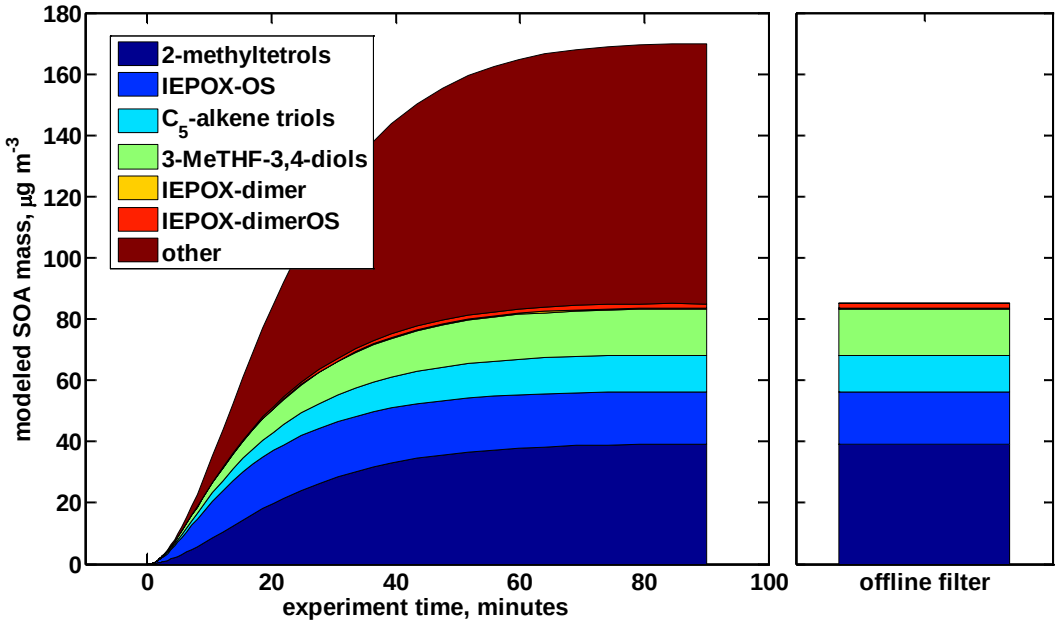

Figure 4.2. Model output of IEPOX-SOA tracers (left panel) and the associated filter-based tracer measurements (right panel) for Exp. No. 1. The "other SOA" is calculated as the difference between the chamber-measured aerosol mass loadings and the sum of the filter-based tracer loadings.

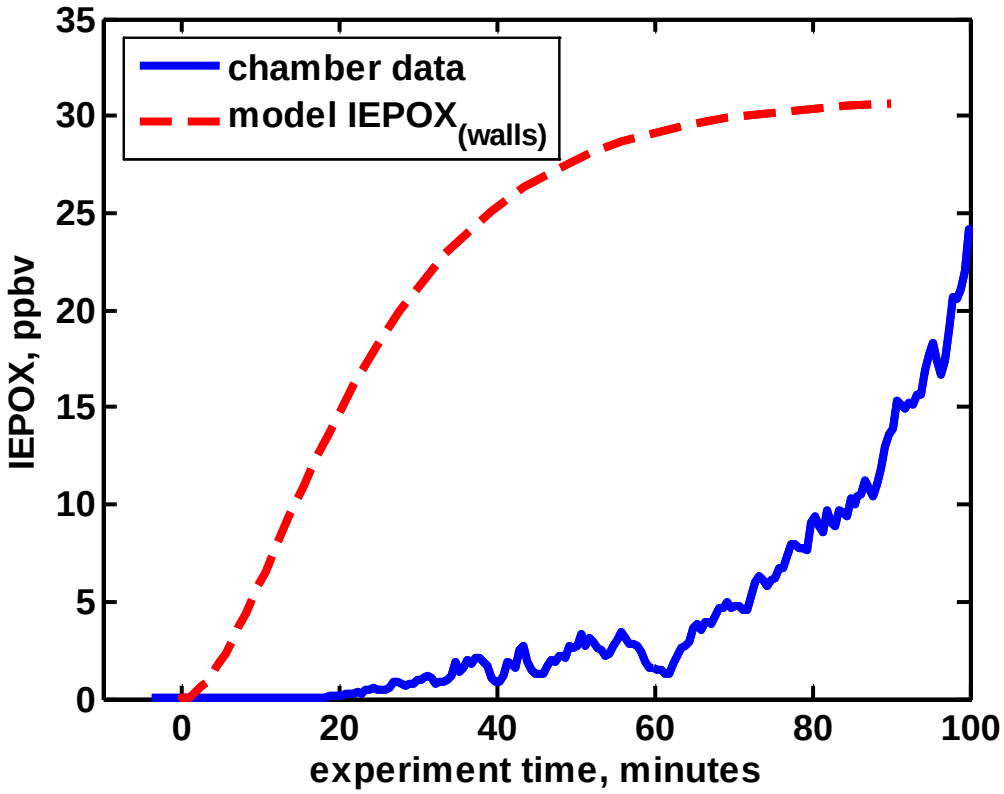

Figure 4.3. Gas-phase IEPOX mixing ratios measured during Exp. No. 1 (solid blue line) and model-calculated IEPOX lost to chamber wall reactions (dashed red line).

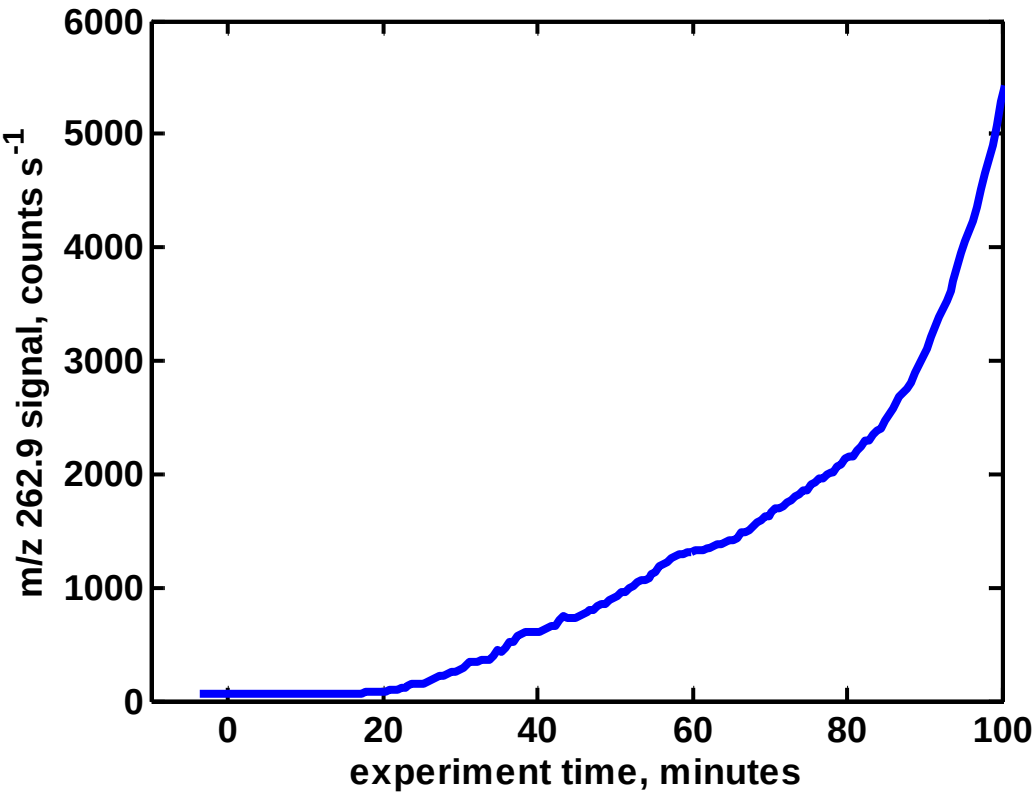

Figure 4.4. Time series of CIMS signal at *m/z* 262.9 Exp. No. 1. *m/z* 262.9 corresponds to the $I^{-}\cdot C_5H_{12}O_4$ ion.

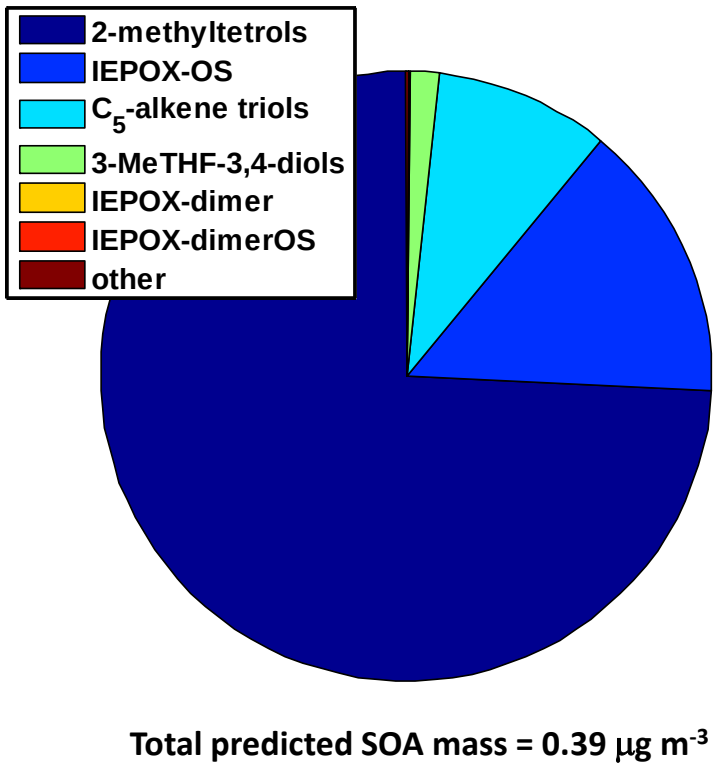

Figure 4.5. Model-predicted IEPOX-SOA tracer distribution and loadings for atmospherically relevant initial conditions.

Table 4.1. Summary of conditions for each chamber SOA experiment.

Exp.No.	IEPOX injected/mg	seed surface area/μm^2 cm^{-3}	seed mass/μg m^{-3}
1	30	1480	113
2	30	1660	125
3	15	1200	76
4	5	800	59
5	5	800	57

Table 4.2. Comparison of tracer mass loadings and model outputs for each chamber SOA experiment.

Exp. No.	Loading/μg m^{-3}							
	total SOA	2-methyltetrols	IEPOX-OS	C_5-alkene triols	3-MeTHF-3,4-diols	IEPOX-dimer	IEPOX-dimerOS	other SOA
1	170	39.1	17.0	12.0	15.1	0.4	1.5	85.0
model:	170	39.1	17.0	12.0	15.1	0.4	1.4	85.0
2	185	41.4	23.7	12.2	13.7	0.7	3.0	90.4
model:	185	41.3	23.7	12.2	13.7	0.7	3.0	90.4
3	131	34.0	13.3	35.3	3.7	3.6	4.0	37.2
model:	131	34.0	13.2	35.3	3.7	3.6	4.0	37.2
4	61	3.7	27.1	18.4	0.04	0.3	10.5	0.9
model:	61	3.7	27.1	18.4	0.04	0.3	10.5	0.9
5	63	4.0	27.4	19.4	0.1	0.3	9.1	2.8
model:	63	4.0	27.4	19.4	0.1	0.2	9.0	2.8

Table 4.3. Model-predicted formation reaction rate constants for IEPOX-SOA tracers.

SOA tracer formed	k	reaction
2-methyltetrols	$2.0 \pm 1.1 \times 10^{-4}$ M^{-2} s	(R1)
IEPOX-OS	$3.1 \pm 0.7 \times 10^{-4}$ M^{-2} s	(R2)
C_5-alkene triols	$7.4 \pm 4.9 \times 10^{-4}$ M^{-1} s	(R3)
3-MeTHF-3,4-diols	$1.2 \pm 1.2 \times 10^{-4}$ M^{-1} s	(R4)
IEPOX-dimer	$1.2 \pm 0.9 \times 10^{-5}$ M^{-2} s	(R5)
IEPOX-dimerOS	$5.8 \pm 5.2 \times 10^{-5}$ M^{-2} s	(R6)
other SOA	$2.9 \pm 2.6 \times 10^{-4}$ M^{-2} s	(R7)

E. References

1. Chen, Y.Z., et al., *Assessment of SAPRC07 with updated isoprene chemistry against outdoor chamber experiments.* Atmospheric Environment, 2015. **105**: p. 109-120.
2. Xie, Y., et al., *Understanding the impact of recent advances in isoprene photooxidation on simulations of regional air quality.* Atmospheric Chemistry and Physics, 2013. **13**(16): p. 8439-8455.
3. Hutzell, W.T., et al., *Interpreting predictions from the SAPRC07 mechanism based on regional and continental simulations.* Atmospheric Environment, 2012. **46**: p. 417-429.
4. Riedel, T.P., et al., *Heterogeneous Reactions of Isoprene-Derived Epoxides: Reaction Probabilities and Molar Secondary Organic Aerosol Yield Estimates.* Environmental Science & Technology Letters, 2015. **2**(2): p. 38-42.
5. Gaston, C.J., et al., *Reactive Uptake of an Isoprene-Derived Epoxydiol to Submicron Aerosol Particles.* Environmental Science & Technology, 2014. **48**(19): p. 11178-11186.
6. Eddingsaas, N.C., D.G. VanderVelde, and P.O. Wennberg, *Kinetics and Products of the Acid-Catalyzed Ring-Opening of Atmospherically Relevant Butyl Epoxy Alcohols.* The Journal of Physical Chemistry A, 2010. **114**(31): p. 8106-8113.
7. Wexler, A.S. and S.L. Clegg, *Atmospheric aerosol models for systems including the ions H^+, NH_4^+, Na^+, SO_4^{2-}, NO_3^-,Cl^-, Br^-, and H_2O.* Journal of Geophysical Research-Atmospheres, 2002. **107**(D14).
8. Pye, H.O., et al., *Epoxide pathways improve model predictions of isoprene markers and reveal key role of acidity in aerosol formation.* Environ Sci Technol, 2013. **47**(19): p. 11056-64.
9. Eddingsaas, N.C., D.G. VanderVelde, and P.O. Wennberg, *Kinetics and Products of the Acid-Catalyzed Ring-Opening of Atmospherically Relevant Butyl Epoxy Alcohols.* Journal of Physical Chemistry A, 2010. **114**(31): p. 8106-8113.
10. Riedel, T.P., et al., *Constraining Condensed-Phase Formation Kinetics of Secondary Organic Aerosol Components from Isoprene Epoxydiols.* Atmospheric Chemistry and Physics, 2015.
11. Guenther, A., et al., *Estimates of global terrestrial isoprene emissions using MEGAN (Model of Emissions of Gases and Aerosols from Nature).* Atmos. Chem. Phys., 2006. **6**(11): p. 3181-3210.
12. Carlton, A.G., C. Wiedinmyer, and J.H. Kroll, *A review of Secondary Organic Aerosol (SOA) formation from isoprene.* Atmos. Chem. Phys., 2009. **9**(14): p. 4987-5005.
13. Hallquist, M., et al., *The formation, properties and impact of secondary organic aerosol: current and emerging issues.* Atmos. Chem. Phys., 2009. **9**(14): p. 5155-5236.

14. Weber, R.J., et al., *A study of secondary organic aerosol formation in the anthropogenic-influenced southeastern United States.* Journal of Geophysical Research: Atmospheres, 2007. **112**(D13): p. D13302.
15. Budisulistiorini, S.H., et al., *Real-Time Continuous Characterization of Secondary Organic Aerosol Derived from Isoprene Epoxydiols in Downtown Atlanta, Georgia, Using the Aerodyne Aerosol Chemical Speciation Monitor.* Environmental Science & Technology, 2013. **47**(11): p. 5686-5694.
16. Lin, Y.H., et al., *Investigating the influences of SO2 and NH3 levels on isoprene-derived secondary organic aerosol formation using conditional sampling approaches.* Atmos. Chem. Phys., 2013. **13**(16): p. 8457-8470.
17. Paulot, F., et al., *Unexpected Epoxide Formation in the Gas-Phase Photooxidation of Isoprene.* Science, 2009. **325**(5941): p. 730-733.
18. Lin, Y.-H., et al., *Epoxide as a precursor to secondary organic aerosol formation from isoprene photooxidation in the presence of nitrogen oxides.* Proceedings of the National Academy of Sciences, 2013. **110**(17): p. 6718-6723.
19. Surratt, J.D., et al., *Reactive intermediates revealed in secondary organic aerosol formation from isoprene.* Proceedings of the National Academy of Sciences, 2010. **107**(15): p. 6640-6645.
20. Lin, Y.-H., et al., *Isoprene Epoxydiols as Precursors to Secondary Organic Aerosol Formation: Acid-Catalyzed Reactive Uptake Studies with Authentic Compounds.* Environmental Science & Technology, 2011. **46**(1): p. 250-258.
21. Pye, H.O.T., et al., *Epoxide Pathways Improve Model Predictions of Isoprene Markers and Reveal Key Role of Acidity in Aerosol Formation.* Environmental Science & Technology, 2013. **47**(19): p. 11056-11064.
22. Alexander, B., et al., *Quantifying atmospheric nitrate formation pathways based on a global model of the oxygen isotopic composition (delta(17)O) of atmospheric nitrate.* Atmospheric Chemistry and Physics, 2009. **9**(14): p. 5043-5056.
23. McNeill, V.F., et al., *Aqueous-Phase Secondary Organic Aerosol and Organosulfate Formation in Atmospheric Aerosols: A Modeling Study.* Environmental Science & Technology, 2012. **46**(15): p. 8075-8081.
24. Bates, K.H., et al., *Gas Phase Production and Loss of Isoprene Epoxydiols.* The Journal of Physical Chemistry A, 2014. **118**(7): p. 1237-1246.
25. Thornton, J.A., C.F. Braban, and J.P.D. Abbatt, *N_2O_5 hydrolysis on sub-micron organic aerosols: the effect of relative humidity, particle phase, and particle size.* Physical Chemistry Chemical Physics, 2003. **5**(20): p. 4593-4603.
26. Thornton, J.A. and J.P.D. Abbatt, *N_2O_5 reaction on submicron sea salt aerosol: Kinetics, products, and the effect of surface active organics.* Journal of Physical Chemistry A, 2005. **109**(44): p. 10004-10012.
27. Zhang, Z., et al., *Technical Note: Synthesis of isoprene atmospheric oxidation products: isomeric epoxydiols and the rearrangement products cis- and trans-3-methyl-3,4-dihydroxytetrahydrofuran.* Atmos. Chem. Phys., 2012. **12**(18): p. 8529-8535.
28. Bertram, T.H., et al., *A field-deployable, chemical ionization time-of-flight mass spectrometer.* Atmospheric Measurement Techniques, 2011. **4**(7): p. 1471-1479.

29. Kercher, J.P., T.P. Riedel, and J.A. Thornton, *Chlorine activation by N_2O_5: simultaneous, in situ detection of $ClNO_2$ and N_2O_5 by chemical ionization mass spectrometry.* Atmospheric Measurement Techniques, 2009. **2**(1): p. 193-204.
30. Brown, R.L., *Tubular Flow Reactors With First-Order Kinetics.* Journal of Research of the National Bureau of Standards, 1978. **83**(1): p. 1-8.
31. Clegg, S.L., P. Brimblecombe, and A.S. Wexler, *Thermodynamic Model of the System $H^+-NH_4^+-Na^+-SO_4^{2-}-NO_3^--Cl^--H_2O$ at 298.15 K.* The Journal of Physical Chemistry A, 1998. **102**(12): p. 2155-2171.
32. Nguyen, T.B., et al., *Organic aerosol formation from the reactive uptake of isoprene epoxydiols (IEPOX) onto non-acidified inorganic seeds.* Atmos. Chem. Phys., 2014. **14**(7): p. 3497-3510.
33. Guenther, A.B., et al., *The Model of Emissions of Gases and Aerosols from Nature version 2.1 (MEGAN2.1): an extended and updated framework for modeling biogenic emissions.* Geosci. Model Dev., 2012. **5**(6): p. 1471-1492.
34. Lin, Y.-H., et al., *Isoprene Epoxydiols as Precursors to Secondary Organic Aerosol Formation: Acid-Catalyzed Reactive Uptake Studies with Authentic Compounds.* Environmental Science & Technology, 2012. **46**(1): p. 250-258.
35. Budisulistiorini, H., et al., *Seasonal characterization of submicron aerosol chemical composition and organic aerosol sources in the southeastern United States: Atlanta, Georgia and Look Rock, Tennessee.* Atmospheric Chemistry and Physics Discussions, 2015. **15**(16).
36. Dockery, D.W., et al., *An Association between Air Pollution and Mortality in Six U.S. Cities.* New England Journal of Medicine, 1993. **329**(24): p. 1753-1759.
37. Chung, S.H. and J.H. Seinfeld, *Global distribution and climate forcing of carbonaceous aerosols.* Journal of Geophysical Research: Atmospheres, 2002. **107**(D19): p. AAC 14-1-AAC 14-33.
38. Surratt, J.D., et al., *Effect of Acidity on Secondary Organic Aerosol Formation from Isoprene.* Environmental Science & Technology, 2007. **41**(15): p. 5363-5369.
39. Piletic, I.R., E.O. Edney, and L.J. Bartolotti, *A computational study of acid catalyzed aerosol reactions of atmospherically relevant epoxides.* Physical Chemistry Chemical Physics, 2013. **15**(41): p. 18065-18076.
40. Riedel, T.P., et al., *Heterogeneous Reactions of Isoprene-Derived Epoxides: Reaction Probabilities and Molar Secondary Organic Aerosol Yield Estimates.* Environmental Science & Technology Letters, 2015. **2**(2): p. 38-42.
41. Surratt, J.D., et al., *Evidence for Organosulfates in Secondary Organic Aerosol.* Environmental Science & Technology, 2007. **41**(2): p. 517-527.
42. Claeys, M., et al., *Formation of Secondary Organic Aerosols Through Photooxidation of Isoprene.* Science, 2004. **303**(5661): p. 1173-1176.
43. Darer, A.I., et al., *Formation and Stability of Atmospherically Relevant Isoprene-Derived Organosulfates and Organonitrates.* Environmental Science & Technology, 2011. **45**(5): p. 1895-1902.
44. Lin, Y.-H., et al., *Light-Absorbing Oligomer Formation in Secondary Organic Aerosol from Reactive Uptake of Isoprene Epoxydiols.* Environmental Science & Technology, 2014. **48**(20): p. 12012-12021.

45. Karambelas, A., et al., *Contribution of Isoprene Epoxydiol to Urban Organic Aerosol: Evidence from Modeling and Measurements.* Environmental Science & Technology Letters, 2014. **1**(6): p. 278-283.
46. Kroll, J.H., et al., *Secondary Organic Aerosol Formation from Isoprene Photooxidation.* Environmental Science & Technology, 2006. **40**(6): p. 1869-1877.
47. Lee, B.H., et al., *An Iodide-Adduct High-Resolution Time-of-Flight Chemical-Ionization Mass Spectrometer: Application to Atmospheric Inorganic and Organic Compounds.* Environmental Science & Technology, 2014. **48**(11): p. 6309-6317.
48. Hennigan, C.J., et al., *A critical evaluation of proxy methods used to estimate the acidity of atmospheric particles.* Atmos. Chem. Phys., 2015. **15**(5): p. 2775-2790.
49. Zhang, X., et al., *Influence of vapor wall loss in laboratory chambers on yields of secondary organic aerosol.* Proceedings of the National Academy of Sciences, 2014. **111**(16): p. 5802-5807.

5. Audits of Data Quality

Our formal quality assurance program complied with a category III quality assurance project plan. To ensure data quality our team ran solvent blanks, blank chamber experiments, and calibrations each time we conducted our experiments. Also, filters were spiked with authentic standards to determine exact extraction efficiencies from filters collected from the chamber. Filters were used to quantify the isoprene SOA constituents used for the modeling work. Instruments were always calibrated before each experimental run with the appropriate authentic standards for the target analytes. Blank experiments were conducted to insure that no compounds were present in the chamber. No isoprene SOA constituents or IEPOX were found in the blank experimental runs. Similar experiments were also conducted for the flow reactor and no SOA or IEPOX was observed in these as well.

For model runs, we ensured the quality of the data by comparing directly to the quantified isoprene SOA tracers. We also ensured the installation of our software by comparing our generated output with concentrations predicted by a separate modeling tool. One graduate student, Dr. Surratt, and Dr. Vizuete independently spot-checked the implemented code. Only the graduate student ran simulations while the other researchers quality assured the code. All model building was completed in increments starting with simplified cases. Should the model replicate observed phenomena in the simplified experiments only then can additional complexity be added to the model. At each stage of this development a minimum of 10% of the produced data would undergo a spot check. In this case a spot check is defined as an independent verification of the generated output by another software system. This was accomplished either by excel spreadsheet for simpler calculations to comparisons with existing runs using different modeling systems. Independent researchers not involved with the collection audited 10% of all measurement data and all calculations were redone in separate software.

6. Conclusions

The atmospheric oxidation of isoprene in the presence of anthropogenic emissions is a potential important contributor to PM. This important PM pathway is especially relevant, given the close proximity to large emissions of biogenic isoprene, to Houston. For Houston to properly assess potential PM control mitigation strategies requires the ability of a model to predict isoprene derived PM accurately. Currently, the air quality models used to make these predictions lack the chemical kinetics needed for the production primarily due to lack of fundamental experimental data from the particle to the gas phase. It is in the gas phase where began our investigation on the chemical mechanisms that were modified to accommodate the isoprene pre-cursors. We found that these modifications increased uncertainty in ozone predictions. This data suggests a continued focus on the productions of radical and PM precursor species to improve the ability of the mechanism to accurately simulate ozone chemistry while maintaining explicit gas phase precursors for isoprene PM.

We have also generated new experimental data that quantitatively measures the reactive uptake of two predominant isoprene-derived gas phase intermediates to PM. These new fundamental measurements provide for the first time the data needed to directly evaluate the aerosol-phase processes in an air quality model. These experiments include *trans*-β-IEPOX and MAE chamber runs where PM growth was measured with various relative humidity (RH) levels and seed aerosol types. These data were used to generate critical parameters needed for the accurate predictions of PM from isoprene. This included providing tracer branching ratios for PM resulting from IEPOX uptake that is a necessary step to appropriately capture isoprene-derived PM production in regional models that often guide policy decisions. It remains crucially important that SOA formation mechanisms are investigated in controlled experiments and then extended to models to ensure that the collective understanding of the mechanisms can accurately represent the observations before they are scaled up to larger model domains.

7. Appendix

A. Thermodynamic Aerosol Model Estimates

As E-AIM input does not include any divalent cation, Na2SO4 was used as a proxy for MgSO4. The ISORROPIA-II aerosol thermodynamic model (http://isorropia.eas.gatech.edu) does include an Mg2+ input for the estimation of various aerosol parameters (Fountoukis and Nenes, 2007). However, we tended to favor the E-AIM model output of aerosol total aqueous-phase volume compared to the ISORROPIA-II output. As a check that the substitution of Na2SO4 for MgSO4 in the estimation of [H+] was reasonable, ISORROPIA-II was run for a Na2SO4+H2SO4 solution and a MgSO4+H2SO4 solution at 10% RH and 50% RH to ensure that pH values were close. For 10% RH ISORROPIA-II predicts a pH of 0.6292 for the Na2SO4+H2SO4 aerosol and a pH of 0.3387 for the MgSO4+H2SO4 aerosol, a difference of ~0.3 pH units. For 50% RH ISORROPIA-II predicts a pH of -0.07972 for the Na2SO4+H2SO4 aerosol and a pH of 0.3796 for the MgSO4+H2SO4 aerosol, a difference of ~0.46 pH units.

B. Assessing MAE wall-loss influences on modeled ϕ_{SOA}.

As mentioned in the main text, an underestimation of the MAE wall-loss could result in a low bias of the estimated MAE ϕ_{SOA}. The chamber wall-loss estimates for MAE (and trans-β- IEPOX) under low RH and aerosol-free conditions used in the box model are shown in Figure 7.2. If instead the MAE wall-loss is allowed to vary from the measured wall-loss estimate, the leveling-off observed in the chamber-measured aerosol mass concentrations for the MAE experiments can be better captured. As an example, in Figure 7.3 the MAE wall-loss is increased from $1.118e^{-005}$ s^{-1} to $4e^{-004}$ s^{-1}, which causes the

modeled MAE SOA to level-off in accordance with the chamber observations. In this case the model-predicted ϕ_{SOA} range is increased from 0.16-0.25 to 0.28-0.37.

Table 7.1. Summary and results of flow reactor experiments.

epoxide	aerosol	RH	aerosol SA ($\mu m^2/cm^3$)[a]	γ
IEPOX	$(NH_4)_2SO_4$	0.55	32,405	1.40E-03
IEPOX	$(NH_4)_2SO_4$	0.56	32,952	9.64E-04
IEPOX	$(NH_4)_2SO_4$	0.54	43,148	5.37E-05
IEPOX	$(NH_4)_2SO_4$	0.57	43,357	1.95E-04
IEPOX	$MgSO_4 + H_2SO_4$	0.17	63,680	1.26E-02
IEPOX	$MgSO_4 + H_2SO_4$	0.2	64,308	9.20E-03
IEPOX	$MgSO_4 + H_2SO_4$	0.2	63,900	8.70E-03
IEPOX	$MgSO_4 + H_2SO_4$	0.46	17,773	1.20E-02
IEPOX	$MgSO_4 + H_2SO_4$	0.55	64,802	8.10E-03
IEPOX	$MgSO_4 + H_2SO_4$	0.56	66,722	8.00E-03
IEPOX	$(NH_4)_2SO_4 + H_2SO_4$	0.17	58,767	2.17E-02
IEPOX	$(NH_4)_2SO_4 + H_2SO_4$	0.21	53,762	2.11E-02
IEPOX	$(NH_4)_2SO_4 + H_2SO_4$	0.21	53,120	2.03E-02
IEPOX	$(NH_4)_2SO_4 + H_2SO_4$	0.54	34,390	1.70E-02
IEPOX	$(NH_4)_2SO_4 + H_2SO_4$	0.55	34,648	1.93E-02
IEPOX	$(NH_4)_2SO_4 + H_2SO_4$	0.53	57,825	2.11E-02
IEPOX	$(NH_4)_2SO_4 + H_2SO_4$	0.52	59,508	1.99E-02
MAE	$MgSO_4 + H_2SO_4$	0.19	25,531	4.80E-04
MAE	$MgSO_4 + H_2SO_4$	0.21	52,056	4.44E-04
MAE	$MgSO_4 + H_2SO_4$	0.23	50,113	5.57E-04
MAE	$(NH_4)_2SO_4 + H_2SO_4$	0.16	26,601	5.72E-04
MAE	$(NH_4)_2SO_4 + H_2SO_4$	0.16	26,656	3.92E-04
MAE	$(NH_4)_2SO_4 + H_2SO_4$	0.22	40,591	5.84E-04

[a]Average total surface area concentration during the decay measurement.

Table 7.2. Summary and results of chamber experiments.

epoxide	aerosol	RH	seed SA ($\mu m^2/cm^3$)	seed mass ($\mu g/m^3$)	mass epoxide injected (mg)	exp. time (hours)	max. mass ($\mu g/m^3$)	chamber SOA mass yield
IEPOX	$(NH_4)_2SO_4$	0.50	1150	35	15	4.5	80	0.04
IEPOX	$MgSO_4 + H_2SO_4$	0.08	900	38	15	1	127	0.08
IEPOX	$MgSO_4 + H_2SO_4$	0.53	1325	47	15	1	91	0.04
IEPOX	$(NH_4)_2SO_4 + H_2SO_4$	0.05	1200	47	15	2	160	0.10
IEPOX	$(NH_4)_2SO_4 + H_2SO_4$	0.59	1060	36	15	4	102	0.06
MAE	$MgSO_4 + H_2SO_4$	0.03	635	33	15	1.5	43	0.01
MAE	$(NH_4)_2SO_4 + H_2SO_4$	0.03	710	32	15	1	45	0.01

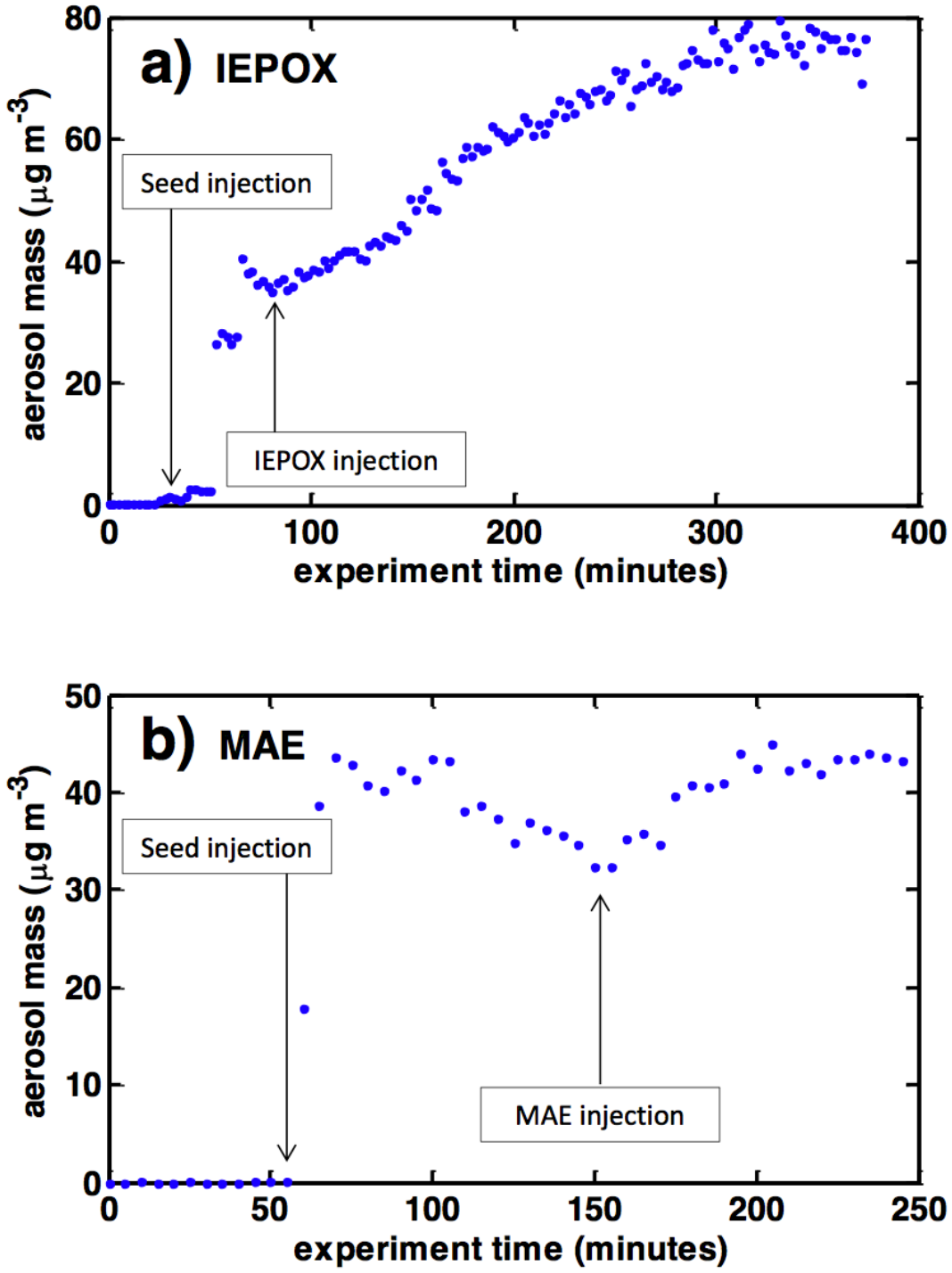

Figure 7.1. Aerosol mass loading time series during chamber SOA experiment for (a) trans-β- IEPOX with (NH4)2SO4 seed (b) MAE with (NH4)2SO4+H2SO4 seed.

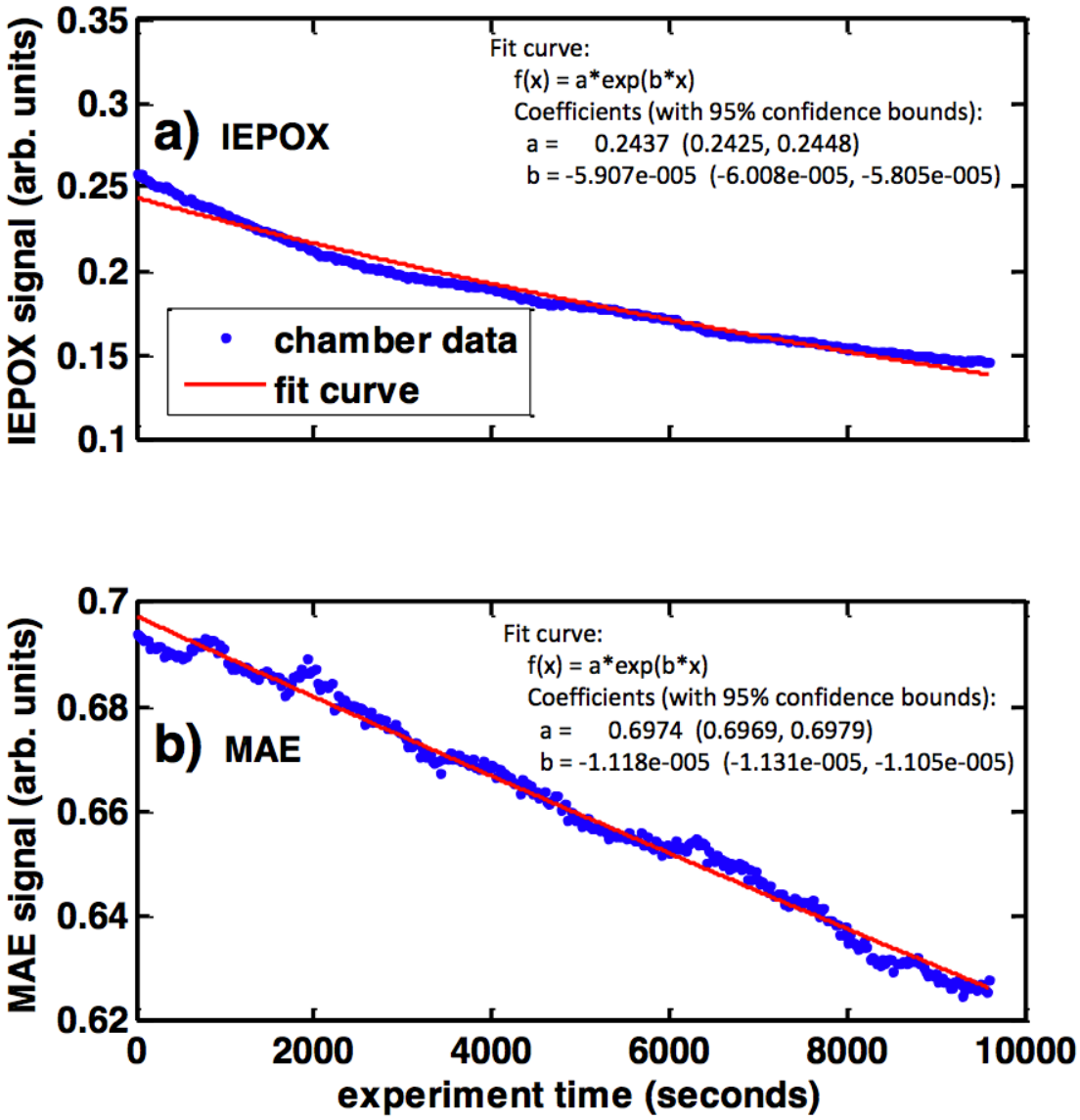

Figure 7.2. Example chamber wall-loss estimates for (a) trans-β-IEPOX (b) MAE. Epoxide signals are shown as blue dots, and the fit is shown as red solid line. The fit coefficient b is used as the wall-loss rate constant for chamber modeling.

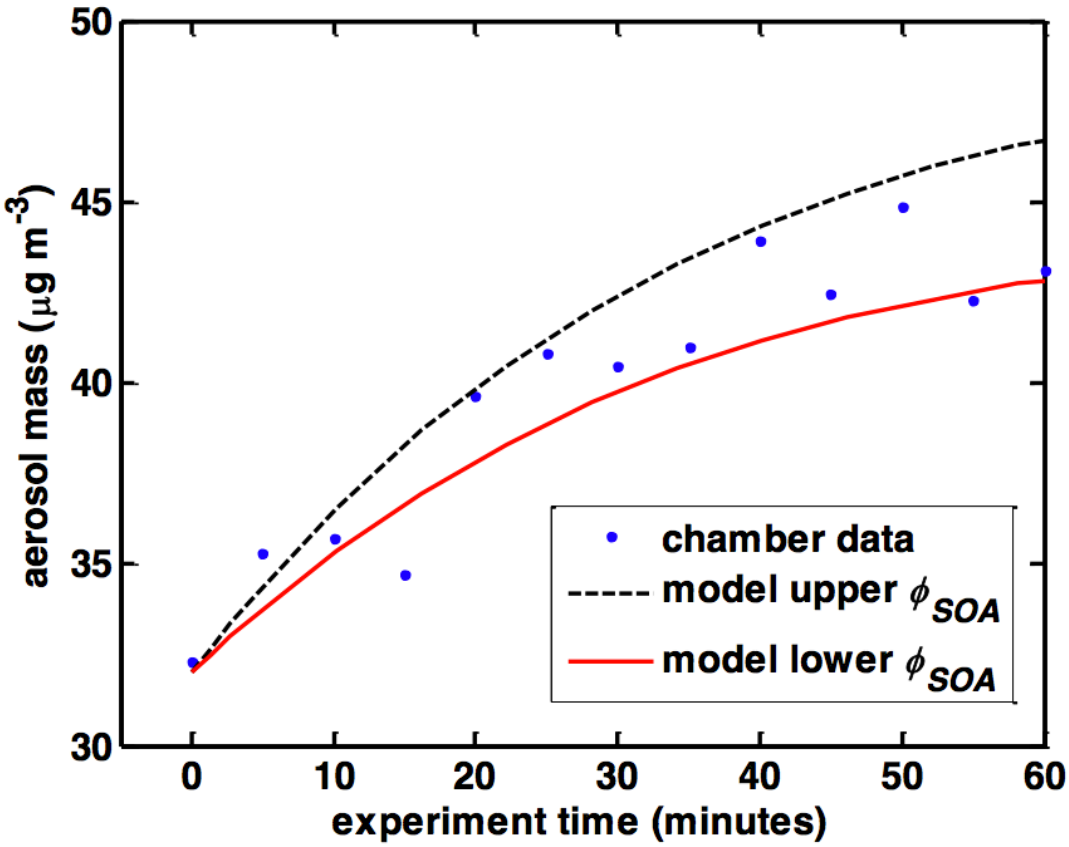

Figure 7.3. Chamber measured (blue dots) and modeled (black dashed line, red solid line) SOA mass loadings for MAE with (NH4)2SO4+H2SO4 seed. The black dashed lines represent an upper estimate of molar SOA yield (ϕ_{SOA}), and the red solid lines represent a lower estimate. Here the MAE wall-loss rate constant is increased by ~35x from the measured wall-loss rate constant in order to capture the leveling-off in aerosol mass loadings.

C. UNC Indoor Environmental Chamber Facility:

This chamber facility is located on UNC's campus within the Department of Environmental Sciences and Engineering. The chamber is contained within 1500 ft^2 laboratory space found in Michael Hooker Research Center Room 0016. In addition to the indoor 10-m^3 flexible Teflon chamber, there are 4 chemical hoods and three large lab benches that are used for placing major analytical instrumentation described below as well as for conducting filter sample extractions needed for chemical characterization of SOA constituents derived from reactive uptake of IEPOX and MAE. The lab has special offices for the Post Doctoral Scholar and Laboratory Technician in charge of organic synthesis. The lab also contains desk space for 5 students.

The chamber will be flushed with high-purity air from a clean air generator before the start of all planned experiments. IEPOX and MAE will be injected into the chamber facility by using a glass-mixing manifold that will be wrapped with calibrated heating tapes heated to 60 °C, and flushed with high-purity N_2 (preheated) at 5 L min^{-1} for at least 1 h using available mass flow controllers. Environmental parameters, gas-phase epoxides, and aerosol physical and chemical properties will be quantitatively measured using the equipment described below.

1. Major instrumentation and analytical equipment at the indoor chamber facility:

1. Hewlett-Packard (HP) 5890 Series II Gas Chromatograph coupled to a HP 5971A Mass Selective Detector. An Econo-Cap-EC-5 Capillary Column (30 m x 0.25 mm i.d.; 0.25 μm film thickness) will be used to separate the resultant trimethylsilyl (TMS) derivatives of 2-methyltetrols, 2-methylglyceric acid, *cis*- and *trans*-3-MeTHF-3,4-diols, and dimers before MS detection.

Protocol for GC calibration

Diluting standards:

Before making the calibration curve, you need to prepare for standards of different concentration. Usually keep 1.5 ppm, 15 ppm and 150 ppm standards for calibration from 0.25 ppm to 100 ppm. These standards can last for months.

Procedures:

a. Pre-clean 9 scintillation vials with methanol and let them dry.
b. Add standards in the vials. Use only one syringe to avoid error in using different syringes.
c. For each compound, start from the lowest concentration. Rinse the syringe well with ethyl acetate before and after each compound. From a lower concentration to a higher concentration, there is no need to rinse the syringe with ethyl acetate. But rinse with the solution you are about to take.
d. Cap the vials (and label the caps) to avoid contamination.
e. Teflon tape the vials of standards and put them back to the freezer.
f. Dry the solutions with gentle N_2 flow.
g. Start heating the heating plate to 70℃ (this might take up to 20 min).

Derivatization:

a. Add 50 uL pyridine and 100 uL BSTFA into each scintillation vial. Caution: pyridine and BSTFA are very volatile. Cap the vials while not used to minimize evaporation.
b. Cap the vials, vortex well and Teflon tape them. Heat them for 1 h.
c. After 1 h, let vials cool to room temperature and use disposable glass pipets to transfer the liquids to HPLC vials.
d. Measure with GC-MS.

Since all of our experiments have been performed with *trans*-*β*-IEPOX, only the *cis*-3-MeTHF-3,4-diols will be formed, and it is unnecessary to calibrate to the other isomers. The following can be used as a guide to ensure that calibrations are close to those

expected. Given calibration coefficients represent the mean and standard deviation of those obtained over the past year. Your calibration coefficients should generally agree with these values:

2-Methyltetrols: $(7.2\pm5.6)\times10^5$ area/ppm
cis-3-MeTHF-3,4-diols: $(1.1\pm0.1)\times10^5$ area/ppm

2. Tofwerk High-Resolution Time-of-Flight Chemical Ionization Mass Spectrometer (HR-ToF-CIMS) equipped with acetate reagent ion chemistry to measure gas-phase IEPOX and MAE signals.

Periodically, it is necessary to check/set the baseline and threshold and measure the Single Ion Area for the CIMS. The following should be performed once every ~2 weeks:

Setting ADC Baseline.
We will iteratively measure the baseline and adjust the offset until the baseline is aligned with our predefined baseline bin value:

a. This diagnostic can be run with/without voltages on.
   If TPS is on, we recommend noting the values of all pulser (U+low, etc) voltages, and setting each of these to 0V.
b. Open the DAQ settings tab and uncheck Ch1 Threshold recording. Set baseline bin to 5.
c. Open Mass Calibration / integration. Set Automatic recalibration to "none." Press Close and return to the acquisition window.
d. On the right side of the Mass Spectrum display, check Ch1 (blue) and uncheck all other display options.
e. Press green start arrow to begin acquisition. The spectrum number in the upper right corner of the mass spectrum should begin to update (e.g., "Spectrum # 1/1000" and growing).
f. Autoscale Y axis by pressing "Y" button to left of display. Show full X axis by pressing "<<X>>" button above display.
g. The recorded spectrum will have shape similar to the figure below. Pickup of the TOF extraction pulses drives the signal low at the beginning. It eventually recovers, reaching a stable value.
h. Hold and drag mouse button to zoom in on noise region of spectrum (region without mass peaks) after time where stable signal value is reached.
i. Note the average Y value in this region.
j. We want the average baseline to equal 5 bins. We will now adjust our offset and repeat this measurement until the average is 5.
k. The average value in the figure above is 4.6 bin. FS = 500 mV; offset is 10.0 mV.
l. To move the baseline 0.40 bins, we shift the offset by approximately 0.4 bin * 1.95 mV / bin = 0.78 mV. To increase bin value, we make the offset more negative. 10.0 – 0.78 = new setting of 10.78 mV.
m. After a couple iterations of offset adjustment and measurement. We settle at offset = 11.1 mV and the baseline is very near 5 bins (shown below).

Setting ADC Threshold.

To determine the best threshold, we look at electronic noise in a singlewaveform spectrum.

a. Set MCP voltage below 1200 V.
b. Open DAQ settings tab and uncheck Ch1 threshold.
c. Open Basic TOF Timing, note current number of waveforms, then set to waveforms = 1. (These instructions assume segments = block = 1).
d. Open Advanced timing tab. Uncheck "Use Max block frequency".
e. Open Mass Calibration / integration. Set Automatic recalibration to "none."
f. Press Close and return to the acquisition window.
g. On the right side of the Mass Spectrum display, check Ch1 (blue) and uncheck all other display options.
h. Press green start arrow to begin acquisition.
i. Adjust displays as for Baseline diagnostic, making sure you see the entire range of the X axis.
j. You are looking at the electronic noise in one waveform (extraction) Determine the maximum bin value recorded for a significant number of samples. In the screenshot above, this is 7.
k. Open the DAQ settings and set the threshold to be 1 bin greater than the value from the last step (8, in this case).
l. Recheck thresholding, Recheck "Use Max block Frequency" and turn Automatic calibration on again.

Measuring Single Ion (SI) Area.

Running the diagnostic:

a. Open ToFDAQ Configuration Window
b. Disable Ch1 thresholding
c. In Mass Calibration / integration tab > Peak Integration Box, press "Measure." A new window will open.
d. Set the Trigger level to 5 mV.
e. Check "Accumulate Histogram" and press Start.
f. When the area values begin to stabilize (usually thousands of events), press Stop.
g. The raw (red) value should be at least 1.1 mV*ns. If it is less than this, increase the MCP setting by 20 V, Clear Histogram, and restart measurement. Repeat until value is greater than 1.1 mV*ns.
h. Press "Save to Ini," to store the raw SI area to your setting file. This number is used for all displayed ion rates during acquisition.
i. Close SI Window. Re-enable Ch1 Thresholding. Exit the menu window.

3. Aerodyne Aerosol Chemical Speciation Monitor (ACSM) will be used to measure submicron mass concentrations of particulate organics, sulfate, nitrate, ammonium, and chloride from the chamber facility. The detection limit is $<0.2\ \mu g/m^3$ for 15 min of signal averaging. The ACSM is built upon the same technology as the widely used Aerodyne Aerosol Mass Spectrometer (AMS), in which an aerodynamic particle focusing lens is combined with high vacuum thermal particle vaporization, electron impact ionization,

and quadrupole mass spectrometry. Mass spectral organic data from the ACSM can be deconvoluted using positive matrix factorization (PMF).
We did not have ACSM at at the indoor chamber facility

4. Brechtel Manufacturing, Inc. (BMI) Scanning Electrical Mobility System (SEMS v5.0) equipped with a cylindrical differential mobility analyzer (DMA, BMI) and a mixing condensation particle counter (MCPC, Model 1710, BMI). This is used to measure the real-time aerosol size distributions contained within the smog chamber. Full aerosol size distributions (10-900 nm) are taken every 4.5 minutes, which includes the up and down scans.

This instrument requires little maintenance. However, the sheath flow RH should be monitored to ensure that it remains <15% RH to prevent potential arching within the DMA column. If the RH>15%, it is necessary to change the desiccant on the pump assembly. Additionally, to ensure that the instrument is calibrated optimally it is necessary to occasionally (approximately every 6 months) atomize monodispersed polystyrene latex (PSL) spheres into the instrument. The PSL diameter measured by the instrument should agree within 1-5 nm of that listed on the PSL container. NOTE: PSLs older than 1 year often deviate from the manufacturer's reported diameter. Also, in general, if you are performing experiments with very high aerosol loadings (>500 $\mu g/m^3$), it is good practice to clean the impactor with DI water and methanol, rinse the anti-static inlet tubing with DI water and methanol, and sample atomized pure DI water for ~30 minutes after the experiments have finished.

5. Dionex 4500i Ion Chromatograph (IC) for cation and anion analysis of aerosol samples collected from flow reactor and environmental chamber experiments.

6. OM-62 Temperature Relative Humidity Data Logger (OMEGA Engineering, INC.). This provides real-time measure of both temperature and RH during all indoor chamber experiments.

This instrument requires very little maintenance apart from the occasional change of batteries. The RH, Dew point, and Temperature measurements are all factory-calibrated.

7. N_2 evaporator (Thermo Electron) for drying filter sample extracts for subsequent GC/MS and UPLC/DAD-ESI-HR-QTOFMS analyses.

a. Make sure that the N2 evaporator is getting adequate flow from the N_2 gas cylinder. PLEASE NOTE THAT YOU DON'T WANT TO OVER PRESSURIZE the N_2 evaporator. Ideally, you don't want to provide anything higher than 2 psi into the system; however, you may need to use a bit more than 2 psi (due to leaks) but not higher than 6 psi!
b. To test that the N_2 evaporator is getting adequate flow, take a 50 mL beaker that contains some methanol in it and put it under one of the needles attached the evaporator system. Ideally, you should see bubbles being generated in the methanol

in this beaker. If you do, then this is telling you are getting good flow of N_2 from the gas cylinder.

c. Before putting the filter extract vials on to the evaporator system, make sure all of the needles on the evaporator system have been pre-cleaned with ChromaSolv-Grade methanol. To do this, take a pre-cleaned 50 mL glass beaker and just submerge the tips of the needles with the N_2 gas flowing through the system. This will provide another check to ensure that N_2 is still flowing adequately through the evaporator.
d. Now, uncap all of the vials and place carefully onto the N_2 evaporator. Please note that you will want to raise the needles up on this evaporator system before placing the vials on it so that you can place these vials on it without spilling them. Once the vials are in place on the evaporator, CAREFULLY lower the needles down into the vials. You want the needles (which are blowing out ultra-pure N_2 gas) to be just above the surface of the methanol inside without the needles EVER touching the methanol.
e. When drying the methanol off the samples, you want the methanol to have just been fully evaporated. Some samples will dry quicker than others.

D. UNC Dual Outdoor Environmental Chamber Facility:

The UNC dual outdoor environmental chamber facility is located in Pittsboro, NC, which is approximately 18 miles south of the main UNC Chapel Hill campus. This 274-m^3 dual chamber consists of two individual chambers with identical volumes (136 m^3) divided by a Teflon film curtain. At the smog chamber facility we have 150 ft^3 of lab space to house equipment directly under the chamber. Prior to the experiments needed for the proposed project, the chamber walls will be cleaned with Milli-Q water (18.2 MΩ) using a special microfiber soft cloth. Chamber walls will then be dried by purging with particle filtered background air, and pacified with 0.2–0.5 ppm of O_3 for 3 to 5 hours. A clean air generator will then be used to introduce zero air into the chambers. Pure water humidifiers will be used to adjust the relative humidity between 30 and 70%.

Data will be recorded every minute from automatic instruments that measure O_3, NO, and NOy and other sensors that record total solar radiation (285-800nm), total UV radiation (285-440 nm), temperature and dew point. C_1-C_{10} volatile hydrocarbons are measured by automated gas chromatographs, every 10 minutes, which translates into every 20 minutes on each chamber side. A detailed chromatogram of C_2 –C_{10} hydrocarbons, including chamber background, is made every hour. Aerosol size distribution measurements are taken every 3 minutes and optical particles (0.3 to 30 mm) counted every 2 minutes with a Grimm model 109 optical particle counter.

Over the past few years we have begun to implement remote operation of many of the chamber operations. This includes: operation and data collection from the chambers 5 chromatographic instruments, remote data collection O_3, NO_X, temperature, humidity, solar radiation and particle size instruments. Routine operations such as purging the chamber with background air and replacing the air in the chamber with purified air, injections of NO_X and isoprene are also “on-line”. The full suite of instrumentation available is described below.

1. Major instrumentation and analytical equipment at the outdoor chamber facility include:

1. Carlo Erba Gas Chromatograph (GC) 4140 equipped with a flame ionization detector (FID). This instrument uses a Supelco 8100 Haysep-Q 2m x 3mm i.d. column, with auto sample loop to measure C_1-C_3 hydrocarbons.

2. Shimadzu 4A isothermal GC/FID with 20 m DB-1 0.32mm ID column and with LN2 cryo sample concentration and auto sample loop to provide C_5-C_7, or C_6-C_8 or C_7-C_{10} depending on oven temperature using capillary GC analysis. Sensitivity is 1 ppbC.

3. Varian 3800 programmable oven GC/FID to provide detailed C3-C10 volatile HC analysis on a fused silica CP-SIL 5CB 25, 60m x1.25 mm i.d. column with auto LN2 sample concentration, every 50 minutes.

4. Valco GC oven with a Valco Ni63 electron capture detector (ECD) and 20 cm x 5mm i.d. molecular sieves column to measure SF_6 as a chamber dilution tracer; another Valco ECD system with a 50 cm x 3 mm glass column to measure peroxy acetyl nitrate (PAN).

5. TSI differential mobility analyzer (DMA) 3080 + condensation particle counter (CPC) 3025A to measure 6 to 900 nm diameter particles depending on flow to DMA and CPC and Refurbished 3017 TSI DMA with a TSI 3022a CPC (sizes 15-780 nm particles)

6. Grimm Model 109 optical aerosol counter (OPC) to measure particles in the 0.3 to 5 um range.

7. Thermo Environmental 49P UV photometric monitor to measure O3 and Thermo Environmental Model 49P UV O_3 calibrator.

8. Thermo Electron SO_2 analyzer

9. Monitor Labs 9841 chemiluminescent NO_X analyzer

10. Io-tech data acquisition data system (64 channels)

11. Epply total UV and TSR sensors

12. Tofwerk High-Resolution Time-of-Flight Chemical Ionization Mass Spectrometer (HRToF-CIMS) equipped with acetate reagent ion chemistry in order to measure oxidation products as well as measuring IEPOX and MAE.

13. Aerodyne Aerosol Chemical Speciation Monitor (ACSM) will be used to measure submicron mass concentrations of particulate organics, sulfate, nitrate, ammonium, and chloride from the chamber facility. The detection limit is <0.2 $\mu g/m^3$ for 15 min of signal averaging. The ACSM is built upon the same technology as the widely used Aerodyne Aerosol Mass Spectrometer (AMS), in which an aerodynamic particle focusing lens is

combined with high vacuum thermal particle vaporization, electron impact ionization, and quadrupole mass spectrometry. Mass spectral organic data from the ACSM can be deconvoluted using positive matrix factorization (PMF).

Table 7.3 Quality Assurance for Sample Preparation and Advanced Analytical Methods in Chamber Experiments

Sample Preparation and Analytical Methods	**Quality Assurance**
Reverse-Phase Ultra Performance Liquid Chromatography/Electrospray Ionization-Quadrupole-Time-of-Flight Mass Spectrometry (RP-UPLC/ESI-Q-TOFMS)	* Only high-purity methanol, acetonitrile and Milli-Q water are solvents used. * Before each analysis period, the mass spectrometer in the negative and positive ion modes using the W reflectron (which provides the highest mass resolution of ~12,000 FWM) will be calibrated using a 1:1 (v/v) solvent mixture of acetonitrile and 0.1% phosphoric acid aqueous solution (Surratt et al., 2008, 2009). 10 known phosphoric acid cluster ions from this solution are used to calibrate the mass range analyzed (50 to 1000 *m/z*). The calibration wizard of this instrument will be used to help ensure high-quality mass calibrations. In addition, a standard compound (i.e., leucine enkphalin MW = 555) will be checked for its accurate mass to ensure a quality mass calibration. If the mass calibration is of high quality then the samples will be immediately analyzed. * Before analyzing samples, the cleanliness of the reverse-phase LC column, ionization source, and mass spectrometer are checked by running the LC gradient scheme (as described in Surratt et al., 2008) without sample injection. * Solvents used to dissolve samples are then injected and analyzed, which also checks the cleanliness of the injector. * A calibration curve is then generated using known authentic standards that are applicable to the analysis of SOA chemical components. The calibration curve checks to make sure the response of instrument is within acceptable limits. If response is unreasonable, then auto tune feature of this instrument is used to ensure that the mass spectrometer is well calibrated and mass resolution is acceptable. * Once the above checks are made, samples are analyzed. Before and after each sample injection, solvent blanks are injected and analyzed. This ensures that the LC column, ionization source, and mass spectrometer remain clean during the analysis period. * During each chromatographic run, 2 ng mL^{-1} of leucine enkphalin (MW = 555) will be used for the lock-mass spray for lock-mass correction to obtain accurate masses for each SOA

	component eluting from the column. This ensures high-quality accurate mass data (i.e., determination of elemental compositions or molecular formulas) for each SOA component detected by this technique (Surratt et al., 2008, 2009). * Control filters outlined above will be run with the samples to establish chemical backgrounds of the filter media. These backgrounds will be subtracted from the "real" filter samples.
Hydrophilic Interaction Liquid Chromatography/Electrospray Ionization-Quadrupole-Time-of-Flight-Mass Spectrometry (HILIC/ESI-Q-TOFMS)	* Only high purity methanol and Milli-Q water are solvents used. * Before each analysis period, the mass spectrometer in the negative and positive ion modes using the W reflectron (which provides the highest mass resolution of ~12,000 FWM) will be calibrated using a 1:1 (v/v) solvent mixture of acetonitrile and 0.1% phosphoric acid aqueous solution (Surratt et al., 2008, 2009). 10 known phosphoric acid cluster ions from this solution are used to calibrate the mass range analyzed (50 to 1000 *m/z*). The calibration wizard of this instrument will be used to help ensure high-quality mass calibrations. In addition, a standard compound (i.e., leucine enkphalin MW = 555) will be checked for its accurate mass to ensure a quality mass calibration. If the mass calibration is of high quality then the samples will be immediately analyzed. * Before analyzing samples, the cleanliness of the HILIC column, ionization source, and mass spectrometer will be checked by running the appropriate LC gradient scheme without sample injection. * Solvents used to dissolve samples are then injected and analyzed, which also checks the cleanliness of the injector. * A calibration curve is then generated using known authentic standards that are applicable to the analysis of organic aerosol chemical components. The calibration curve checks to make sure the response of instrument is within acceptable limits. If response is unreasonable, then auto tune feature of this instrument is used to ensure that the mass spectrometer is well calibrated and mass resolution is acceptable. * Once above checks are made, samples are analyzed. Before and after each sample injection, solvent blanks are injected and analyzed. This ensures that the LC column, ionization source, and mass spectrometer remain clean during the analysis period. * During each chromatographic run, 2 ng mL^{-1} of leucine enkphalin (MW = 555) will be used for the lock-mass spray for lock-mass correction to obtain accurate masses for each SOA component eluting from the column. This ensures high-quality accurate mass data (i.e., determination of elemental compositions or molecular formulas) for each organic aerosol component detected by this technique.

	* Control filters outlined above will be run with the samples to establish chemical backgrounds of the filter media. These backgrounds will be subtracted from the "real" filter samples.
High Performance Liquid Chromatography/Electrospray Ionization-Ion Trap Mass Spectrometry (ESI-ITMS)	* Only high purity methanol and Milli-Q water are solvents used. * Before analyzing samples, the cleanliness of the LC column, ionization source, and mass spectrometer will be checked by running the appropriate LC gradient scheme without sample injection. * Solvents used to dissolve samples are then injected and analyzed, which also checks the cleanliness of the injector. * The $[M - H]^-$ and $[M + H]^+$ ion signals will be optimized by introducing a 1 mg mL^{-1} malic acid and leucine enkphalin standard solutions, respectively. These standards will help to optimize the following parameters of the ion trap mass analyzer: sheath gas flow, auxiliary gas flow, source voltage, capillary voltage, tube lens offset, capillary temperature, and maximum ion injection time. * Two scan events will be used during each chromatographic run; scan event 1 will be the full scan mode in which data are collected from *m/z* 50 to 1000 in both the negative and positive ionization modes and scan event 2 will be the MS^n mode in which product ions were generated from significant base peak ions observed in scan event 1. * For MS^n experiments (i.e., detailed structural characterization of organic aerosol constituents from analysis of daughter ions produced from CID of parent ions detected in MS mode), an isolation width of 2.5 *m/z* units and a normalized collision energy level of 35% will be applied.
Matrix-Assisted Laser Desorption Ionization Time-of-Flight Mass Spectrometry (MALDI-TOFMS)	* Only high-purity solvents are employed. * Before each analysis period, the steel target plate, which eventually contains the samples and blanks, is sonicated in methanol and milli-q water for 15 minutes for each solvent. This ensures that the plate is cleaned for the analysis period. * A 10 mL Hamiltonian syringe is then cleaned with 10 washes of each of the following (in this order): methanol, acetonitrile, dichloromethane, isopropanol, milli-Q water, and then methanol. * Using the syringe, 4 to 8 mL of each solvent blank, filter blank, and sample extract are then transferred and applied onto the steel target plate and allowed to air-dry. * Between each application of every sample filter extract, blank filter, and control filter, the syringe is washed 10 times using the solvent in which these samples are dissolved. * Graphite is the matrix applied for this technique. The brush that is used to apply the graphite matrix to the samples dried on

	the steel target plate is always sonicated in high-purity methanol for 5 minutes before every use.
Gas Chromatography/Mass Spectrometry (GC/MS) with prior Derivatization	* Only high-purity solvents are employed. * Before analyzing samples, the cleanliness of the GC column, ionization source, and mass spectrometer are checked by running the GC temperature program with a clean solvent injection. * Derivatization agents (e.g., PFBHA, BSTFA, and TMCS) are always purchased in the highest available purity. * Additionally, solvent blanks and control filters are always analyzed before each analysis period. * Also, between the analyses of each filter sample, a solvent blank injection is always conducted to ensure cleanliness. * The syringe used to inject samples is also washed several times using a number of solvents by using the automated syringe-washing feature of this instrument.
Ion Chromatography	* Only Milli-Q water and high-purity solvents are employed. * Before analyzing samples, the cleanliness of the IC columns, injector, and detector are checked by injecting filter blanks and solvent blanks. * Calibration curves for each inorganic ion and water-soluble organic ions of interest are then generated. If these curves are acceptable, then samples are immediately analyzed. * Between each sample injection, a solvent blank is always injected and analyzed to ensure that the instrument remains clean during the sample analysis period.
Total Aerosol Peroxide Quantification by a Diode Array Spectrophotometer	* High-purity solvents (i.e., methanol, ethyl acetate, chloroform, and acetic acid) are only employed. * Before each analysis period, a peroxide calibration curve will be obtained from a series of benzoyl peroxide solutions. * From this calibration curve, the known molar absorptivity of benzoyl peroxide will be checked to ensure proper instrument conditions. Solvent blanks and filter blanks (controls) will also be analyzed with the filter sample extracts. * Between the analyses of each sample, a solvent blank will be analyzed to establish the baseline for the next sample measurement.
Particle-into-Liquid Sampler (PILS)	* To sustain a constant sampling flowrate of 12.5 L min^{-3}, the appropriate sized critical orifice is used. * To sample 30 nm – 1 μm particles (PM_1), a single-stage pre-impactor (D_{50} = 1 μm) removes super-micrometer sized particles. * An automated three-way valve (Swagelok) either directs airflow through (filter mode) or bypasses (sample mode) a high efficiency particulate air (HEPA) filter to allow for chemical background level testing during chamber experiments or field campaigns.

	* A series of three denuders remove gases that can bias aerosol mass concentration measurements of measureable chemical constituents; inorganic vapors are removed by two denuders with annular glass surfaces (URG-2000-30 x 242-3CSS), and a third denuder (Sunset Laboratory Inc.), composed of 15 thin carbon filter paper sheets (3.15cm x 20.32 cm x 0.04 cm thick) with 0.2 cm gaps between them, removes organic gases. The glass denuders are placed upstream of the carbon denuder so that detailed extraction tests can be carried out following operation. * Ambient air that is sampled is mixed with steam that is introduced through a tube (0.04 cm ID, the tip of which has a thermocouple attached to provide accurate steam injection tip temperature readings. An algorithm is used to account for pressure fluctuations and air flow over the tip, to provide real-time control of the steam injection tip temperature at 100 ± 2°C. * Rapid adiabatic mixing of steam and the cooler ambient air (containing aerosol) produces a high supersaturation of water vapor that allows droplets to grow large enough (D_p > 1μm) to be collected by inertial impaction. * Dilution occurs when the impacted droplets are washed from the impactor plate. In addition to the wash-flow, dilution takes place as a result of water vapor condensation on the impactor wall. Thus, a dilution factor will be determined by spiking the wash-flow of Milli-Q water with a non-interfering ion (i.e., LiF or LiBr) with subsequent IC or ESI-MS analyses.
Aerosol Chemical Speciation Monitor (ACSM)	* Chamber or ambient air (containing gas and aerosol) is introduced consistently into the ACSM by a high vacuum system through a particle aerodynamic lens. This lens focuses submicron aerosol (~ 40 – 1000 nm aerodynamic diameter) into a narrow beam that is directed to a resistively heated particle vaporizer. Non-refractory aerosol components flash vaporize on impaction at 600°C. * Resultant vapors are ionized by electron impaction (EI). Positive ions are then extracted into the quadrupole mass spectrometer for determination of mass-to-charge ratio (*m/z*). * Ionization efficiency calibration of the ACSM, needed to determine mass concentration of species from raw MS ion signals, will be performed weekly for chamber experiments and for field campaigns by sampling DMA size-selected dry ammonium nitrate particles. This calibration is used for relevant calculations as described in detail previously. * Chemical background will be removed from “real” ACSM signals by rotating automatically with a valve between filtered and non-filtered air. * The mass axis of the mass spectrometer will be continually calibrated with a naphthalene internal standard that will be

	contained in a liquid reservoir that is continually leaked into the mass spectrometer at low mixing ratios (reference = direct discussions with Aerodyne Inc., 2009).
Proton Transfer Reaction High-Resolution Time-of-Flight Mass Spectrometer (PTR-TOFMS)	* Ambient mixing ratios for most VOCs and their volatile/semivolatile oxidation products will be determined converting the raw PTR-TOFMS signal in Hz into mixing ratio in ppbv or pptv using experimentally determined calibration factors. * Calibrations for the PTR-TOFMS system will be conducted using high-pressure cylinders containing synthetic blends of selected non-methane hydrocarbons, oxygenated VOCs, and acetonitrile (common tracer for anthropogenic pollution). * Similar to Apel et al. (1998), standards will be diluted to atmospheric mixing ratios (ppbv to pptv levels) with catalytic converter prepared zero air adjusted to maintain humidity of the sampled air. * For field campaigns, calibrations will be conducted upon arrival and set-up at the field site. Additionally, calibrations will be done again mid-way through the campaign to ensure accurate response factors of VOCs and oxygenated VOCs (e.g., ketones, aldehydes, nitrates, alcohols) * For chamber experiments, calibrations will be checked monthly to ensure accurate response factors. * Background signals will be obtained every 2.5 h during field campaigns and chamber experiments. The system will be zeroed for 4 cycles by diverting the flow of ambient air through a heated catalytic converter (0.5% Pd on alumina at 450°C) to oxidize VOCs and determine the system background signals. * Using a linear interpolation, the background will be subtracted from ambient signals.

E. UNC Biomarker Mass Spectrometry Facility:

The ultra performance liquid chromatography/diode array detection electrospray ionization high-resolution quadrupole time-of-flight mass spectrometer (UPLC/DAD-ESI-HR-QTOFMS) will be utilized to identify and quantify IEPOX-and MAE-derived organosulfates as well as light-absorbing SOA constituents. The UPLC/ESI-HR-Q-TOFMS instrument is located in the UNC Biomarker Mass Spectrometry Facility. This facility is a shared-use facility located in the Department of Environmental Sciences and Engineering in the School of Public Health. It is one of six sub-core facilities within the Center for Environmental Health and Susceptibility (CEHS) Systems Biology Facility Core (SBFC). The center provides expertise for qualitative analysis and quantitative measurement of both low-molecular-weight compounds and larger biomolecules. The Agilent Accurate-Mass Quadrupole Time-of-Flight mass spectrometer in the facility is

currently configured with an electrospray ionization (ESI) source and is coupled to an Agilent 1200 Rapid Resolution LC. Chromatographic separations are performed with columns packed with sub two-micron particles generating backpressures up to 600 bar. The mass spectrometer can acquire spectra over the range of 30 to 3200 *m/z* and routinely achieves less than 1 ppm accuracy across the entire mass range (and sub-2ppm in MS/MS mode). The high resolution and accurate mass capabilities in both MS and MS/MS modes make it a powerful tool for compound identification, and structural elucidation of unknowns.

In addition to state-of-the-art mass spectrometer systems available, the core facility employs experienced research staff ready to assist us at any stage of the process from method development through sample analysis and data interpretation. The current fee for using this facility is $15 per injection onto the UPLC/DAD-ESI-HR-Q-TOFMS.

F. UNC Synthesis Laboratory:

The Synthesis Laboratory facilities include a containment laboratory located in McGavran-Greenberg Hall, with sealed floors and a separate air-handling system. This 520 ft^2 laboratory is dedicated to organic synthesis, with two 5 ft chemical fume hoods and two controlled atmosphere glove boxes. This laboratory will house the Synthesis Laboratory's spectroscopy and chromatography instrumentation. Within the laboratory is located a standard inventory of equipment required for organic synthesis, including Rotary evaporators, a gas chromatograph, high performance liquid chromatograph (HPLC) with scanning UV-Vis detector suitable for preparative-scale separations, an HPLC with scanning fluorescence detector, water-baths, -80 and -20 ^oC freezers, refrigerators, a double-beam UV-Vis spectrophotometer (Cary 3), a scanning fluorometer, a gas-tight glove-box for highly hazardous or atmosphere-controlled procedures, and two analytical micro-balances.

The Synthesis Laboratory has access to variable temperature, multinuclear NMR spectrometers (Varian Inova 500, 600 and 700 MHz spectrometers) through the Department of Biochemistry on a service (cost/time used) basis and to additional variable temperature, multinuclear Varian Inova 400 and 500 MHz spectrometers, also on a service basis, through the School of Pharmacy. Dr. Zhenfa Zhang is a trained operator and thus the synthesis laboratory does not pay operator costs. IR spectroscopy is available through the UNC Department of Chemistry. The Biomarker MS Facility, described above, is available for mass spectrometric needs associated with characterizing target products and intermediates.